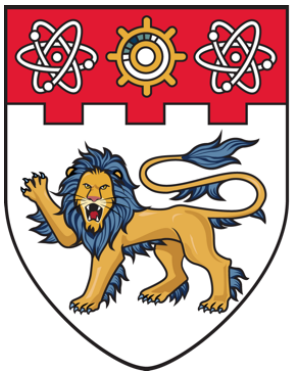

NANYANG TECHNOLOGICAL UNIVERSITY
SINGAPORE

MATERIALS AND MECHANISMS OF SODIUM AND ZINC-BASED ENERGY STORAGE

JIA GUICHONG

SCHOOL OF PHYSICAL AND MATHEMATICAL SCIENCES

2019

MATERIALS AND MECHANISMS OF SODIUM AND ZINC-BASED ENERGY STORAGE

JIA GUICHONG

SCHOOL OF PHYSICAL AND MATHEMATICAL SCIENCES

A thesis submitted to the Nanyang Technological University in partial fulfilment of the requirement for the degree of Doctor of Philosophy

2019

Statement of Originality

I hereby certify that the work embodied in this thesis is the result of original research done by me except where otherwise stated in this thesis. The thesis work has not been submitted for a degree or professional qualification to any other university or institution. I declare that this thesis is written by myself and is free of plagiarism and of sufficient grammatical clarity to be examined. I confirm that the investigations were conducted in accord with the ethics policies and integrity standards of Nanyang Technological University and that the research data are presented honestly and without prejudice.

[Input Date Here]
July-29-2019
Date

[Input Signature Here]
[Input Name Here]
JIA GUICHONG

Supervisor Declaration Statement

I have reviewed the content and presentation style of this thesis and declare it of sufficient grammatical clarity to be examined. To the best of my knowledge, the thesis is free of plagiarism and the research and writing are those of the candidate's except as acknowledged in the Author Attribution Statement. I confirm that the investigations were conducted in accord with the ethics policies and integrity standards of Nanyang Technological University and that the research data are presented honestly and without prejudice.

[Input Date Here]

July-29-2019

Date

[Input Supervisor Signature Here]

Fan Hong Jin

[Input Supervisor Name Here]

Authorship Attribution Statement

Please select one of the following; *delete as appropriate:

This thesis contains material from [2] paper(s) published in the following peer-reviewed journal(s) / from papers accepted at conferences in which I am listed as an author.

Chapter 3 is published as:
Guichong Jia, Huanwen Wang, Dongliang Chao, Haiyong He, Nguyen Huy Tiep, Yongqi Zhang, Zheng Zhang, Hong Jin Fan*, Ultrathin $MoSe_2$ @N-doped Carbon Composite Nanospheres for Stable Na-Ion Storage, Nanotechnology 28, 42LT01 (2017). DOI: 10.1088/1361-6528/aa8c55.

The contributions of the co-authors are as follows:

- Prof. Hong Jin Fan provided the initial project direction and edited the manuscript drafts.
- I designed the experiment with Huanwen Wang.
- I performed all the laboratory work and analyzed the data at School of Physical and Mathematical Sciences with an assistance from Huanwen Wang.
- I prepared the manuscript drafts. The manuscript was revised by Dongliang Chao, Yongqi Zhang and Prof. Hong Jin Fan.
- The TEM and EDS data were collected by Dongliang Chao.
- The TGA data were collected by Haiyong He.
- The XRD data were collected by Nguyen Huy Tiep.
- The XPS data were collected and analyzed by Zheng Zhang in Agency for Science, Technology and Research (A*STAR).

Chapter 4 is published as:
Guichong Jia, Dongliang Chao*, Nguyen Huy Tiep, Zheng Zhang, and Hong Jin Fan*, Intercalation Na-Ion Storage in Two-Dimensional $MoS_{2-x}Se_x$ and Capacity

Enhancement by Selenium Substitution, Energy Storage Mater. 14,136-142 (2018). DOI: 10.1016/j.ensm.2018.02.019.

The contributions of the co-authors are as follows:

- Prof. Hong Jin Fan provided the initial project direction and edited the manuscript drafts.
- I designed the experiment with Dongliang Chao.
- I performed all the laboratory work and analyzed the data at School of Physical and Mathematical Sciences.
- I prepared the manuscript drafts. The manuscript was revised by Dongliang Chao and Prof. Hong Jin Fan.
- The TEM and EDS data were collected by Dongliang Chao.
- The XRD data were collected by Nguyen Huy Tiep.
- The XPS data were collected and analyzed by Zheng Zhang in Agency for Science, Technology and Research (A*STAR).

Note: If published materials are not inserted as thesis chapters, students must acknowledge co-worker contributions in the acknowledgement section of their thesis.

[Input Date Here]	[Input Signature Here]
July-29-2019	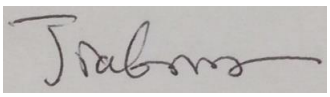
. . . . .	. . . . .
Date	[Input Name Here] JIA GUICHONG

Abstract

The tremendous development of mobile electronics and renewable energy technology facilitate the research on energy storage devices. Electrochemical energy storage system is an effective technique to store and release electricity reversibly. The rechargeable lithium ion battery as the conventional electrochemical energy storage system has a great development in recent two decades. However, it has hampered by the increasing cost of lithium resource and severe safety issues. Thus, the exploration of alternative rechargeable batteries is significant and emergent. Sodium and zinc-based batteries show the promising prospect because of the low cost and high safety, especially for the grid-scale energy storage system. In this thesis, the materials and mechanisms of sodium and zinc-ion batteries have been investigated.

Two-dimensional layered transition-metal dichalcogenides (TMDs) are widely studied as anode materials in sodium-ion batteries (SIBs) in recent years. However, their storage mechanisms of sodium ions are vague. There are two problems, the first one is the reversibility of conversion reaction during cycles, and the second one is the specified potential ranges for conversion reaction and intercalation process.

In chapter 3, the reversibility of the layered TMDs in SIB has been investigated. The thin nanosheets $MoSe_2$ uniformly embedded within an N-doped carbon matrix was synthesized. Its electrochemical properties were measured in detail, which exhibited better rate and cycle performance than those of pure $MoSe_2$ in SIB. And the storage mechanism of sodium ions was studied with ex-situ X-ray diffraction characterization, which revealed the irreversible conversion reaction of $MoSe_2$ during the first cycle within the potential range from 0.01 to 3.0 V vs. Na^+/Na.

Meanwhile, layered TMDs, as the anode materials in SIBs, always suffer from the poor capacitance retention due to the damage of the layered structure, but the research on its protecting conditions is few. Moreover, some ex-situ measurements could be influenced by the ambient environment, so the direct and continuous observation with in-situ characterization techniques in working condition is highly significant. Herein, in chapter 4, the specified potential ranges of conversion reaction and intercalation process have been studied in detail. The $MoS_{2-x}Se_x$/graphene foam was synthesized via a Se substitution reaction of S in MoS_2/graphene foam. The controlled potential ranges were applied on $MoS_{2-x}Se_x$/graphene foam in SIBs to investigate the triggering condition of

damaging the layered structure. The composition changes and crystal structure evolution are characterized by the combined in-situ Raman spectroscopy and ex-situ XRD measurements, which also revealed the specified potential ranges for conversion reaction and intercalation process. MoS_2/graphene foam with only intercalation process shows better capacitance retention than that with intercalation process and conversion reaction simultaneously. And $MoS_{2-x}Se_x$/graphene foam exhibited better rate performance than that of MoS_2/graphene foam within the chosen potential range of intercalation process, which indicated the Se substitution of S in MoS_2 is an effective method to enhance the electrochemical performance, owing to the expanded interlayer spacing. This work provides direct observation on mechanism study and effective strategy to improve the electrochemical performance.

For the alternative battery of zinc-ion battery (ZIB), it has the advantages of low cost and high safety because of the cheap cost and aqueous electrolyte. Vanadium-based materials are one main type of cathode materials for ZIBs. However, the main studies are focused on the vanadium-based materials with high valence states of vanadium, such as the V^{4+} and V^{5+}. The vanadium-based materials with low valence states have not been reported yet. Herein, the synchrotron-based in-situ X-ray diffraction and density functional theory (DFT) calculation have been applied to explore the materials. In chapter 5, the VOOH with a low valence state (V^{3+}) has been synthesized and investigated, as cathode material, in aqueous ZIB, which exhibited a high specific capacity and good rate performance. And the electrochemical reaction kinetics was studied with galvanostatic intermittent titration technique (GITT) and redox current contribution analysis. Its composition changes and crystal structure evolution were also characterized by synchrotron-based in-situ X-ray diffraction. Combined with density functional theory (DFT) calculation, a new storage mechanism of zinc ions in vanadium-based materials have been proposed. This work can provide an insight to explore new electrode materials for electrochemical energy storage.

All in all, the elaborate control and design of experiments and advanced characterization techniques are effective strategies for material exploration and mechanism study.

Acknowledgements

It is a wonderful journey of my Ph.D. program in the days of my youth at Nanyang Technological University, Singapore. For all my experience here, it is an invaluable treasure for my life, I would like to thank the people I meet here.

I would like to give my deepest gratitude to my supervisor Prof. Fan Hong Jin. With his guidance, I have learnt a lot of knowledge not only about scientific researches, but also how to understand the world. He not only encourages me to explore the natural world, but also inspires me to know myself. And thanks for his support in my research work and life. These help and inspiration are my treasure for my whole life.

My sincere thanks also give to Prof. Yu Ting and Prof. Xu Zhichuan for their support and supervision in my research progress. I also would like to express my sincere appreciate to my group mates and all collaborators, Dr. Wang Huanwen, Dr. Chao Dongliang, Dr. Zhang Yongqi, Dr. Xu Kun, Dr. Ouyang Bo, Dr. Zhang Zheng, Dr. Zhu Changrong, Dr. Nguyen Huy Tiep, Dr. He Haiyong, Dr. Xu Jing, Dr. Tan Hua, Dr. Zhou Yao, Dr. Wang Zhe, Mr. Hu Yuzhong, Mr. Hu Ping, for their fruitful discussions and support during my Ph.D. study.

Last but most essentially, I need to thank my family for their support and understanding. With their love and encouragement, I could control my life by myself and discover the world and myself.

Table of Contents

List of Abbreviation

LIB: Li-ion battery

SIB: Sodium-ion battery

AZIB: aqueous zinc ion battery

KIB: potassium ion batteries

2D: two-dimensional

TMDs: transition metal dichalcogenides

GO: graphene oxide

rGO: reduced graphene oxide

EC: ethylene carbonate

DMC: dimethyl carbonate

EMC: ethyl methyl carbonate

PVDF: polyvinylidene fluoride

NMP: N-methyl-2-pyrrolidinone

SEI: solid electrolyte interphase

CV: cyclic voltammetry

GCD: galvanostatic charge and discharge

EIS: electrochemical impedance spectroscopy

GITT: galvanostatic intermittent titration technique

CE: coulombic efficiency

CVD: chemical vapor deposition

FESEM: field-emission scanning electron microscopy

HRTEM: high-resolution transmission electron microscopy

STEM: scanning transmission electron microscopy

HAADF: high-angle annular-dark-field

ABF: annular-bright-field

AFM: atomic force microscopy

XPS: X-ray photoelectron spectroscopy

XRD: X-ray diffraction

XAS: X-ray absorption spectroscopy

XANES: X-ray absorption near-edge structure

EXAFS: extended X-ray absorption fine structure

HXAS: hard X-ray absorption spectroscopy

SXAS: soft X-ray absorption spectroscopy

NMR: Nuclear magnetic resonance

FTIR: Fourier transform infrared spectroscopy

EDS: energy dispersive X-ray spectroscopy

BET: Brunauer-Emmett-Teller

TGA: thermogravimetric analysis

SEAD: selective area electron diffraction

DFT: density functional theory

Chapter 1 Introduction

1.1 Background

Energy is the fundamental power for the development of our world. In recent hundreds of years, people mainly utilize the fossil fuels, such as coal and oil, to develop our society, but the overconsumption of the fossil fuels results in the environmental pollution incidentally, so it is very significant to develop the renewable energy technologies. Some of them, such as solar cell and wind power generators, are intermittent and localized power suppliers, which need energy storage systems to store and release energy reversibly. Simultaneously, the increasing development of portable energy sources, such as portable electronics and electric vehicles, also facilitate the research on energy storage devices.[1]

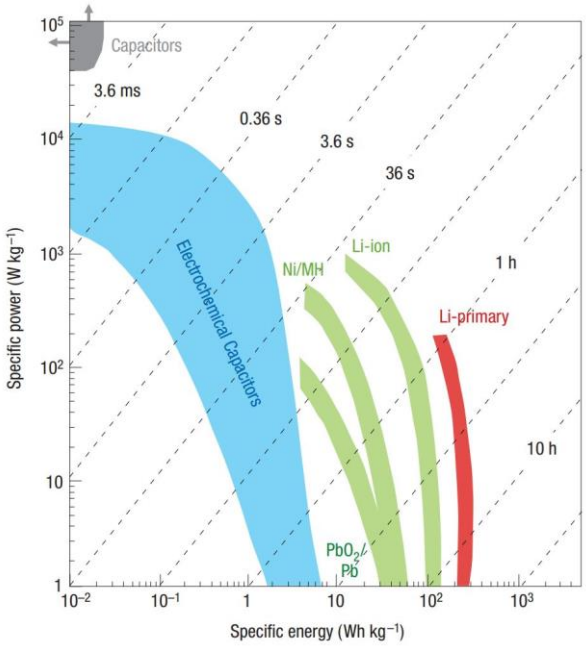

Fig. 1.1 Ragone plot of specific power against specific energy for various electrochemical energy storage devices. Times shown are the time constants of the devices.[2]

Compared with other energy storage devices, such as flywheel and compressed air energy storage systems, electrochemical energy storage system can store and release electricity reversibly and directly with high efficiency and versatility through the electrochemical reactions during charge and discharge processes. For electrochemical energy storage systems, they have many types, for instance, rechargeable battery, supercapacitor, flow battery, fuel cell and so on. These electrochemical energy storage

systems have their characteristic features, which can be used in different environment, distinguishing by their different power and energy densities (Figure 1.1[2]). Rechargeable batteries have tremendous development in recent years because of the rapid development of portable electronics and electric vehicles, especially the Li-ion battery.

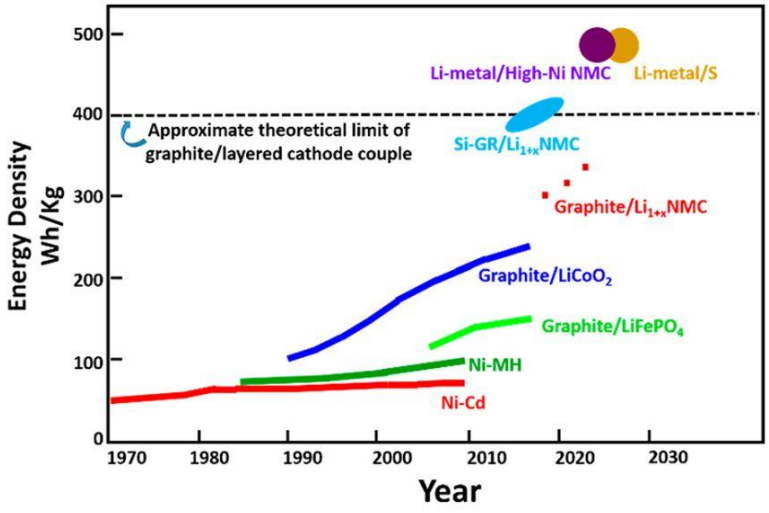

Fig. 1.2 The development of gravimetric energy densities for diverse electrochemical batteries.[3]

For the rechargeable batteries, they have developed from the non-rechargeable batteries. Before the commercialization of LIBs in 1991 from Sony Corporation, there are several main kinds of rechargeable batteries, for instance, lead-acid battery, Ni-Cd battery and Ni-MH battery (Figure 1.2).[3] But most of their markets are replaced by LIBs in recent years, because LIBs have some advantages, for instance, high open circuit voltage, high specific volumetric and gravimetric energy densities, low self-discharge effect, long cycling life, good environment compatibility and no memory effect. Thus, LIBs can be used in most environment, and their researches are so impressive. Researchers still promote and optimize their power and energy densities, which are limited by their electrochemical reaction principles and electrode materials. The conventional commercialized rechargeable LIB consists of the positive electrode and negative electrode, separating by an organic separator with porous and ion-selective features impregnated within organic electrolyte. The positive and negative electrodes are prepared by casting slurries, consisting of active materials (such as lithium metal oxide for positive material and graphite for negative material) with some specified additives, on aluminum and copper foils, respectively. However, the rapid development of LIBs results in the large demand for lithium resource, which brings about its increasingly high cost. Because the finite resource and uneven distribution of lithium element around the

world and the severe safety concerns of LIBs with organic electrolyte, many researchers have transferred their research fields into other metal ion batteries, for example, sodium ion battery, zinc ion battery, potassium ion battery and so on.[4]

1.2 Introduction to sodium-ion battery

1.2.1 Configuration and working mechanism

LIBs suffer from the increasing cost and uneven distribution of lithium resource on the earth and severe safety issues, which have the potential crisis of satisfying the industrial demand and large-scale energy storage application, for instance, the electric vehicles and grid storage devices. Sodium ion battery (SIB), as one kind of rechargeable metal ion batteries, has the potential to be an alternative of LIB, because the sodium element is one kind of abundant resource and can be extracted from seawater, and its distribution is more even than that of lithium element in the world. It is known that sodium element has the similar physicochemical properties with the lithium element. Moreover, the SIB also has similar mechanism and configuration with LIB, although the sodium element endows a bigger diameter, higher redox potential ($E^0_{(Na^+/Na)} = -2.71\ V$ versus standard hydrogen electrode, 0.3 V above that of lithium element) and lower capacity density than that of lithium, which are the challenges of SIB to commercialization, especially the poor fast-charging capability for portable energy storage. The techniques of fabricating LIB and commercialized experience can be transplanted into SIB easily, such as the synthesis routes, fabrication facilities and inner structures. Thus, the SIB is the most promising alternative of LIB in the next decades.

In terms of the electrochemical mechanism of the SIB, it is similar with LIB. The working principle and inner configuration of SIB are schematically presented in Figure 1.3[5]:

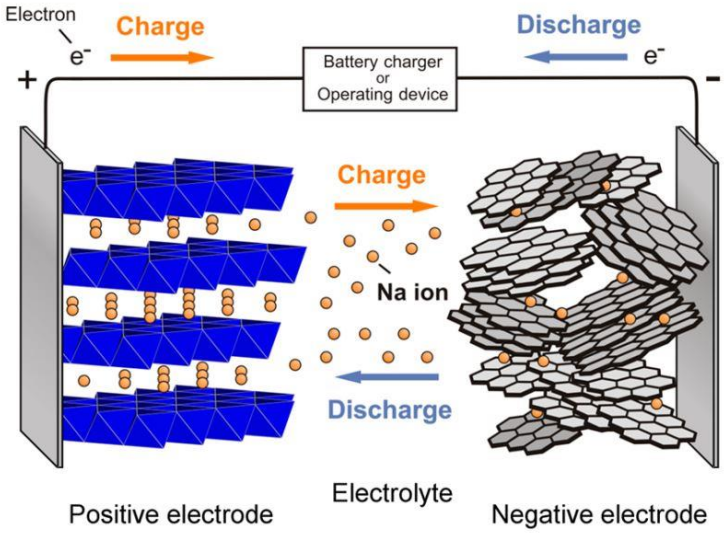

Fig. 1.3 Schematic illustration of Na-ion batteries.[5]

The inner components consist of the positive electrode (also named cathode), negative electrode (also named anode), separator, electrolyte and current collectors. The cathode materials and anode materials are coated on current collectors, and the separator is porous and insulated. The electrolyte is one kind of materials with the features of ionic conduction and electric insulation. The principle of electrochemical energy storage is reversible electrochemical reactions, which lead to the reversible transition between chemical energy and electricity. During the charge process, the cell will be applied an external power, and electrons will be introduced into the anode through the current collector from the outside circuit. Simultaneously, sodium ions will be extracted from the cathode side and inserted into the anode side crossing the separator and electrolyte. The electricity has been transferred into electrochemical energy and the potential of the cell will increase. As for the discharge process, the electrochemical energy will be changed into electricity and the potential of the cell will decrease. The sodium ions will be deintercalated from the anode and intercalated back into cathode, and the electrons will be released into external circuit. The reversible extraction and insertions of metal ions during charge and discharge processes are basic principles of rechargeable metal ion batteries.

1.2.2 Materials in sodium-ion battery

In this part, the materials in SIBs will be introduced in detail, which mainly contain the cathode materials, anode materials and electrolytes.[6]

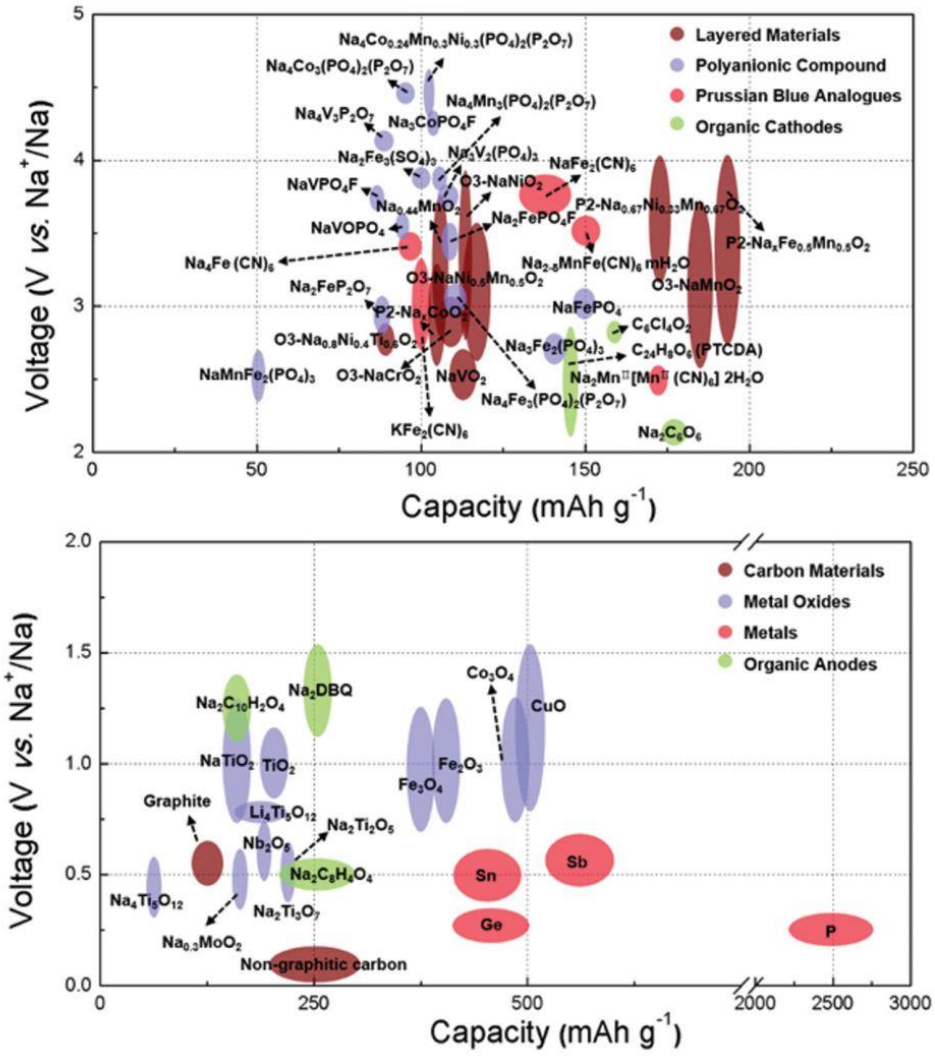

Fig. 1.4 Voltage–capacity plots of various cathode and anode materials for NIBs.[6]

Cathode materials

In terms of the cathode materials of SIB, they should be a series of materials that can accommodate sodium cations, and sodium ions can be reversibly deintercalated from and intercalated in them. Considering the enough potential of the battery, cathode materials should have the reasonably potential beyond 2 V to that of sodium element. Because the sodium cation has a larger diameter than that of lithium cation (0.98 Å for sodium cation and 0.69 Å for lithium cation), the application of cathode materials in SIB has several challenges, including the low ion mobility, severer volume change and structural degradation during the long-term cycle. Herein, this part will summarize the most-recent development of cathode materials.[6-8]

One kind of cathode materials is metal oxide, which mainly contains the layered oxide and tunnel oxide. As for the layered oxides, they have three kinds of types,

including O3, P3 and P2-phase layered oxides (in Figure 1.5).[9] O3 and P2-phase layered oxides are common cathode materials. The crystal structure of O3-phase is in the formation of closely packed ABCABC, and sodium layers and metal layers are surrounded by the oxygen ion framework. Sodium ions reside at the edge-shared octahedral sites with MO_6 octahedra. In contrast, the sodium cations are stabilized at the trigonal prismatic sites in P2-phase layered oxides, which forms the ABBAABBA crystal structure. P3-phase layered oxides have the manner of ABBCCA formation, which can also be obtained by transferring from O3-phase layered oxides during intercalation and deintercalation of sodium ions. Compared with P2-type compounds, O3-type layered oxides can deliver higher reversible capacities, but they are still hindered by the poor air stability. P2-phase layered oxides have better cycling stability, because they have larger trigonal prismatic sites occupied by sodium cations, which can facilitate the transportation of sodium ions in their frameworks. Many types of sodium-based layered oxides can be named as Na_xMO_2 (M is Ni, Co, Mn, Fe, Cr, V, etc.). These layered oxides can be synthesized with solid-state reactions, hydrothermal reactions and co-precipitation techniques in air. For instance, $NaMnO_2$ has a high theoretical capacity of 242 mAh g^{-1} due to a highly active reaction couple of M^{4+}/M^{3+}.[9]

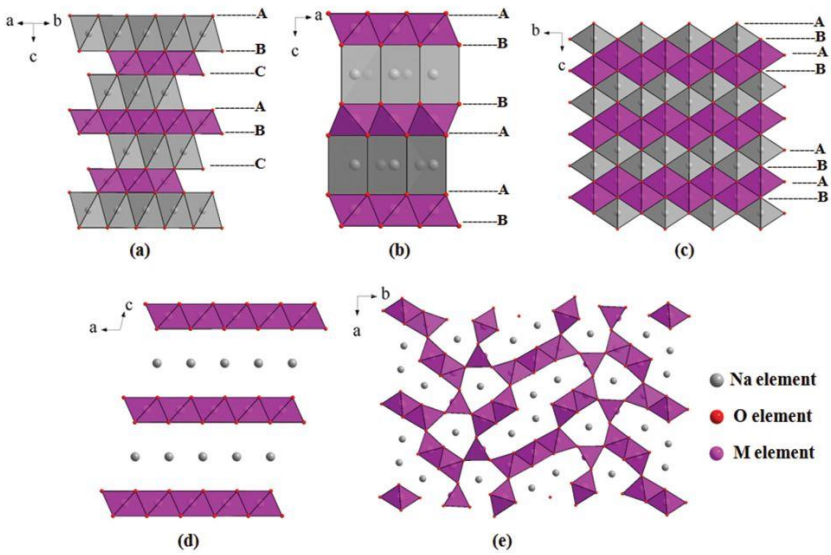

Fig. 1.5 Patterns of crystal structures: a) O3-type layered oxides, b) P2-type layered oxides, c) O2-type layered oxides, d) birnessite-type layered oxides, and e) tunnel oxides. The capital letters (A, B, C) are used to describe the packing patterns of the oxygen-ion frameworks.[9]

Another kind of oxides is tunnel-type oxide. In the framework, all M^{4+} ions and half of the M^{3+} ions locate at the octahedral sites (MO_6), simultaneously, and other M^{3+} ions occupy the square-pyramidal sites (MO_5), which form an orthorhombic structure. Two double and one triple octahedral chains link to the edge shared MO_5 by the vertices,

which forms two types of tunnels, the large S-shaped tunnels (half-filling) and small tunnels (filling), which are also illustrated in Figure 1.5.[9] Thus, sodium cations can be allowed to extract from and inserted into the forming tunnel structures along the c direction. The tunnel-type oxide of $Na_{0.44}MnO_2$ served as the cathode material has been studied completely in recent years, and it exhibits a theoretical specific capacity of 121 mAh g^{-1}.[9]

The second main kind of cathode materials is the polyanionic compounds. They have the advantages of good structural diversity and stability, high operating voltage and good cycle performance, as one kind of common intercalation cathode materials, which motivate tremendous researches. In general, the compounds mainly contain phosphates, pyrophosphates, fluorophosphates, sulfates and mixed polyanions.[10-11] Their typical crystal structures are presented in Figure 1.6.[9]

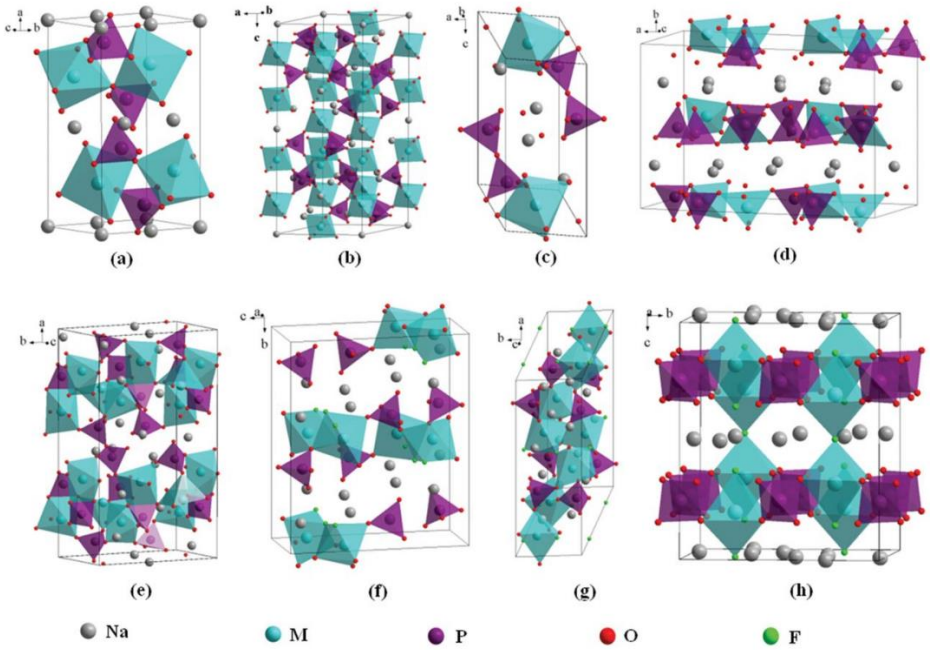

Fig. 1.6 Crystal structures of: a) olivine $NaMPO_4$, b) NASICON $Na_3V_2(PO_4)_3$, c) triclinic $Na_2MP_2O_7$, d) orthorhombic $Na_2MP_2O_7$, e) orthorhombic $Na_4M_3(PO_4)_2P_2O_7$, f) orthorhombic Na_2MPO_4F, g) monoclinic Na_2MPO_4F, and h) tetragonal $Na_3M_2(PO_4)_2F_3$ (M represents transition metals).[9]

The third kind of cathode materials is the Prussian blue, which have many analogues with the formation of $A_xMM'(CN)_6$ (A = Na, K; M and M′ = Fe, Co, Mn, Ni). In typical, Prussian blue analogs always have the cubic morphologies. Metal ions situate at the corners of cube and cyanide groups are linked along cube edges. The metal ions link to the cyanide groups with the carbon or nitrogen groups on the cyanides.[12-13] A typically inner structure is illustrated in Figure 1.7.[12] Because each unit contains eight subunit cells inside, one Prussian blue cubic structure has large interstitial space between metal ions

and cyanide groups, which can accommodate metal ions reversibly, for instance, Li^+, Na^+, K^+, NH_4^+, even alkaline earth divalent ions and zeolitic water insides. Most of Prussian blue analogs can be classified into two main kinds, $KM[Fe(CN)_6]$ and $Na_xM[M'(CN)_6]$. They show relatively high working potentials in SIBs. However, the organic groups in Prussian blue compositions have a low electrical conductivity. And their electrochemical performance is limited by the low specific capacities. These advantages and disadvantages arouse wide interests in investigating and promoting their electrochemical properties in SIBs. The first cathode made from Prussian blue was reported by Goodenough's group in 2012 year[13]. They fabricated several kinds of open framework $KMFe(CN)_6$ compounds (where M is Mn, Fe, Co, Ni and Zn) doped with different metal ions and then investigated their electrochemical properties in SIBs within an organic electrolyte. The highest reversible specific capacity of around 100 mAh g^{-1} was exhibited by $KFe(II)Fe(III)(CN)_6$ in liquid-carbonate organic electrolyte. Just two years later, the specific capacity of Prussian blue as cathode material in SIB was improved two times. Cui's group developed a new kind of Prussian blue analogue with eight large interstitial sites, manganese hexacyanomanganate, which showed a high specific capacity of 209 mAh g^{-1}.[12]

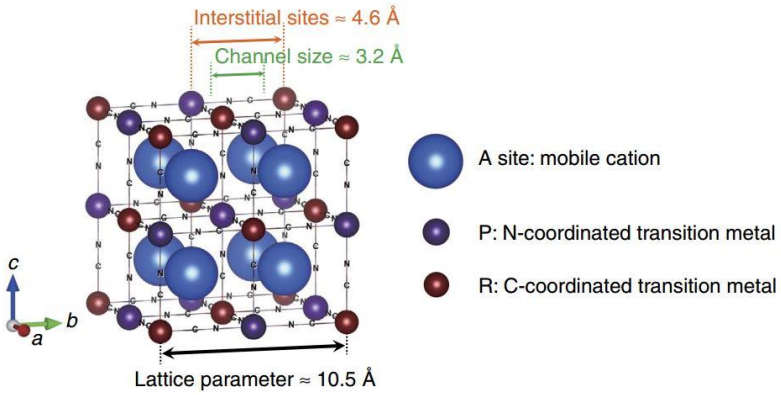

Fig. 1.7 The typical crystal structure of PBAs contains a face-centered cubic phase. Owing to the lengthy CN bonds, subunit cells contain large interstitial sites.[12]

The last main type of cathode materials is organic compounds. Organic compounds as the electrode materials in green rechargeable batteries provoke extensive interests because of their advantages of cheapness, flexibility, designability and recyclability.[14] In terms of the organic cathode materials in SIBs, many kinds of organics have been investigated. The main types are organosulfur compounds, aromatic carbonyl derivatives, radical compounds, pethidine derivatives and functional polymers. In general, they

exhibit relatively low conductivities and specific capacities. Few of them have demonstrated promising electrochemical performance with relatively high working potential and high specific capacities simultaneously. As for the energy storage mechanisms of organic cathode materials, cation-intercalation and anion-intercalation have been proposed. The former is the intercalation and deintercalation of sodium cations coupled with electrochemical reactions in functional groups, the latter is the incorporation and extraction of anions from electrolyte in the organic compounds, regardless of metal cations. Recently, the rapid development of flexible and wearable electronics stimulates the exploration of organic cathode materials, even all organic rechargeable batteries.[6, 15]

Anode materials

In terms of anode materials, they should have the reasonable potentials below 2 V vs Na^+/Na, comparing with cathode materials. The potential of full cell is calculated by the potential difference between cathode and anode. As for the requirements of anode materials, they should have high conductivity, low working potentials, high specific capacities, eco-friendly, cheap and stability in various working conditions. In terms of the storage mechanism of sodium ions, they can be classified into three main types: intercalation, alloying and conversion anode materials.[14]

For the intercalation type of anode materials, sodium cations can intercalate into and deintercalate from their matrixes reversibly. Graphite is the most conventional anode material in LIBs, but it cannot be used in SIBs directly, because its interlayer spacing and thermodynamics are not favorable owing to the large diameter of sodium ion. The cheap cost and abundant resource still provoke the development on it. The graphite can be used by modifying with all kinds of functional groups and interlayer-expanding techniques. In terms of other kinds of carbon materials in SIBs, non-graphite carbon compounds are investigated tremendously, for instance, hard carbon, cokes and carbon blacks. Hard carbon is a good one, which can exhibit a theoretical capacity of 240 mAh g^{-1} with good cycle stability in some organic electrolytes. And some polymer-derived carbon is also studied as intercalation-type anode materials in SIBs, although they usually do not have much high specific capacities. Some oxides and sulfides are also explored as potential anode materials, such as Sb_2O_4 and all phases of iron oxides.[16-17] Some kinds of layered $NaMO_2$-type oxides can also be used as anode materials. For instance, $Na_2Ti_3O_7$ can show an initial specific capacity of beyond 200 mAh g^{-1} due to the relatively low redox

potentials of $Ti^{3+/4+}$.[18-19] However, their electrochemical working potentials are relatively high compared with sodium metal.

The second main type is alloying anode materials. They always have been expected to be the next-generation anode materials, especially to meet the requirements of high energy density in electric vehicles, owing to the advantages of high specific capacities and relatively low redox potentials. However, they have the shortages of huge volume expansion during alloying and deallying processes, which is the bottleneck of their commercialization.[6] The silicon can be applied as anode material in LIBs with a high theoretical specific capacity, but it cannot be used in SIBs because of the unsuitable electrochemical activity. Other kinds of alloying-based anode materials have been discovered recently, such as Sn, Ge, P, Sb and their derivatives. Researchers fabricate compositions with these alloying materials and porous conductive materials, expecting trade off the volume change and high specific capacity and enhance the electrical conductivity.[20]

Table 1.1 Summary of typical alloying-type anode materials for SIBs.[6]

	Reduction product	Theoretical capacity (mAh g^{-1})	Volumn expansion (Na_xX/X) (%)	Average voltage (vs Na^+/Na) (V)
Sn	$Na_{3.75}Sn$	847	520	~0.2
Sb	Na_3Sb	660	393	~0.6
P	Na_3P	2596	408 (red); 500 (black)	~0.4
Ge	NaGe	369	305	~0.3

The last main type of anode materials is conversion-type materials. They can provide reasonable energy and power densities simultaneously, comparing with the intercalation and alloying materials, and their electrical conductivities are higher and volume changes are lighter.[21] However, as for conversion materials, they always have the transition of crystal structures and composition evolution during cycles, so they have poor electrochemical kinetics and capacity retentions, marked by large voltage hysteresis between charge and discharge processes. This phenomenon can be observed in some sulphides, phosphides, fluorides and their hybrids. Their reaction equation can be described as: a $Na^+ + a\ e^- + M_bX_c \leftrightarrow b\ M + a\ NaX_d$.[22] In general, most conversion reactions are reversible, especially in some specific conditions. And some of them cannot

return to the original composition after cycle in some extreme conditions, such as complete reduction at low potential. As for the potentials of conversion materials, they do not have obvious voltage plateaus, because the changes of crystal structures and the multi-ions reactions involved during cycle.

Electrolyte

The electrolyte is an important and critical component in all kinds of batteries. It has the features of ion-conductivity and electrical insulation. Ions need to be transported between anode and cathode materials crossing the electrolyte during charge and discharge processes, so it needs the high ion conductivity, which is a significant factor of high rate performance. Meanwhile, it should separate the cathode and anode from short circuit, so enough electrical insulation is also significant. Because the outside potential will be introduced on the batteries through the two electrodes, the electrolyte should bear the high potential from decomposition, which can result in the severe exploration. Thus, the capability of bearing high potential is the critical parameter to high-voltage batteries. Simultaneously, the chemical stability and viscosity of the electrolyte under potential are also important, the changes of ion mobility and electrical insulation have much influence on the electrochemical performance of rechargeable batteries. And electrolyte should not react with cathode and anode materials. Recently, the electrolyte has a new and significant requirement of large working temperature range (low melting and high boiling points are desirable) as the commercialization of electric vehicle around the world. In terms of the electrolytes, they have three main kinds, including liquid electrolytes, polymer electrolytes and solid-state electrolyte.[23]

In SIBs, the conventional electrolytes are sodium salts of $NaClO_4$, $NaPF_6$ or Na bis(trifluoromethane) sulfonamide (NaTFSI), which are dissolved in a series of carbonate ester solvents, such as propylene carbonate (PC), fluoroethylene carbonate (FEC), ethylene carbonate (EC), dimethyl carbonate (DMC) and diethyl carbonate (DEC) with different ratios. Recently, considering the safety of batteries, resulting from the organic electrolytes, solid state electrolyte has a tremendous development, which mainly contains the ceramic, glassy and solid-state ion materials.[24]

1.3 Introduction to zinc-ion battery

Rechargeable metal ion batteries have severe operating safety problems and environmental benignity, especially with organic electrolytes. And the large grid-scale energy storage systems have the requirement of low cost. The aqueous rechargeable batteries, as the promising alternative, have attracted extensive attention in recent years because of the abundant resource, working safety and environmental friendliness. Moreover, these batteries usually work in aqueous electrolytes, which have higher ionic conductivity and lower viscidity than those of the organic electrolytes and solid-state electrolytes. Furthermore, the common mild neutral electrolyte does not need much maintenance and special protection during operation. As for all kinds of the aqueous rechargeable batteries, researchers transfer their interests in aqueous zinc ion batteries, because the cost of zinc is so low and their specific capacities are much higher than most of the aqueous batteries.[25] However, its working potential (< 2V generally) is lower than LIB and SIB, so it is not suitable for portable energy storage. The limited cathode material is also a big problem, which needs much effort to discover new kinds of electrode materials. As for large-scale energy storage system, it needs the stable cycles for thousands of times, which is a challenge to ZIB at present. Thus, much effort needs to be devoted to optimizing the electrochemical performance and discovering new types of electrode materials further.

In terms of the history of aqueous ZIBs, they are evolved from the previous alkaline zinc-MnO_2 batteries, which do not have the rechargeable capability. The development of rechargeable metal ion batteries, especially the lithium ion batteries, provokes the re-discovery of zinc-MnO_2 batteries. In 1986, the Zn-MnO_2 batteries with neutral electrolytes had been proposed and fabricated. Until 2011, Kang's group uncovered the Zn^{2+} ions intercalation and deintercalation properties in the aqueous ZIBs with MnO_2 cathode material, although it had a low specific capacity and poor cycle performance. Inspired by this proposed and realized mechanism in aqueous ZIBs, extensive efforts have been devoted to discovering new kinds of electrode materials, promoting the frameworks of batteries and developing novel types of electrolytes (in Figure 1.8).[26]

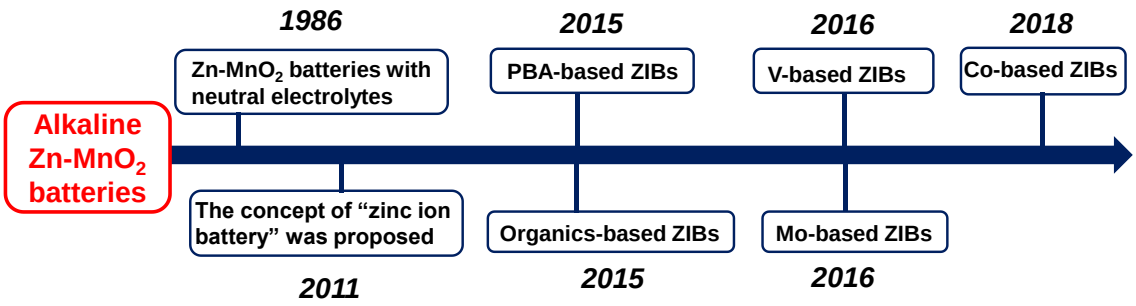

Fig. 1.8 A brief development history for ZIBs.[26]

1.3.1 Configuration and working mechanism

Metallic zinc has a higher redox potential (-0.76 V vs. standard hydrogen electrode) than that of lithium element (-3.0 V), which will reduce the working potential according to the electrochemical mechanism. And the thermodynamics of aqueous electrolyte also limit its working potential. However, the metallic zinc has a relatively high specific capacity of 820 mAh g^{-1}, which is much higher than those of intercalation-type electrode materials. And zinc is abundant and nontoxic, which is an intriguing advantage for ZIBs. As for the configuration of ZIB, they have a similar inner structure to rechargeable metal ion batteries, containing the anode, cathode, separator and electrolyte. Its configuration is exhibited in Figure 1.9.[27]

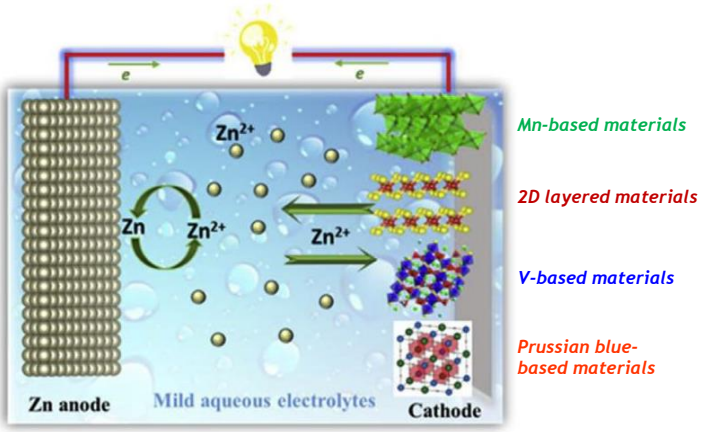

Fig. 1.9 Schematic illustration of the electrochemical principle of aqueous zinc ion batteries.[27]

In terms of the storage mechanism in ZIBs, there are still some confusions. In general, they can be classified into three types according to the recent researches: Zn^{2+} insertion/ extraction; Zn^{2+}/H^{+} insertion/extraction and chemical conversion reaction. They will be introduced in detail.[28]

Zn^{2+} insertion/extraction: This mechanism is the first one and accepted dominantly for most cathode materials. Many kinds of compounds with tunnel and

layered-type structures work in this mechanism. Zn^{2+} ions intercalate into and deintercalate from their frameworks because of the small ionic diameter of Zn^{2+} (0.74 Å). The first and typical insertion/ extraction mechanism was found by Kang's group[29] from α-MnO_2 with a tunnel structure inside. The reaction is depicted as follows:[25]

Cathode process: $Zn^{2+} + 2\,e^- + 2\,\alpha\text{-}MnO_2 \leftrightarrow ZnMn_2O_4$ *(1.1)*

Anode process: $Zn \leftrightarrow Zn^{2+} + 2\,e^-$ *(1.2)*

Furthermore, this mechanism was also be found in other materials with open crystal structures, such as various phases of MnO_2 and vanadium oxides with different phases.

Zn^{2+}/H^+ insertion/extraction: In some host materials, they also can insert and extract the H^+ with Zn^{2+} during cycles, especially the intercalation/ deintercalation of H^+ first because of the smaller diameter and higher thermodynamics and kinetics. The first one with this mechanism was illustrated by Wang's group,[30] which was supported by the GITT characterization. And this cointercalation mechanism also be found in some vanadium-based materials, such as $NaV_3O_8 \cdot 1.5H_2O$.[31]

Chemical conversion reaction: Unlike the insertion/ extraction of ions, some types of cathode materials can be converted into some hydroxides reversibly. This mechanism was first found in α-MnO_2, there is a reversible chemical conversion reaction between α-MnO_2 and MnOOH.[32] This mechanism always been discovered in manganese-based materials and their main conversion reactions are between oxides and hydroxides.

1.3.2 Materials in zinc-ion battery

In terms of the materials in ZIBs, they mainly consist of anode, cathode and electrolyte. The main types of materials will be introduced as follows (in Figure 1.10)[25]:

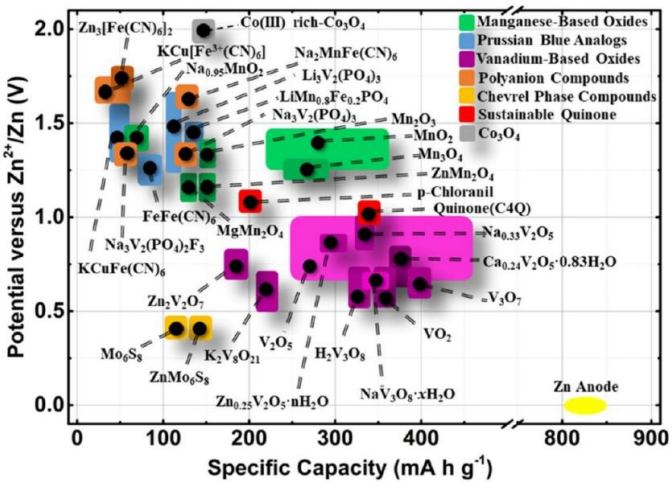

Fig. 1.10 Operating potential vs. specific capacity for various cathode materials and Zn anode recently applied for aqueous ZIBs.[25]

Cathode materials

The main cathode materials are manganese-based, vanadium-based and Prussian blue-based materials (in Table 1.2)[26]:

Table 1.2 Comparisons of the advantages and disadvantages for the Mn-based, V-based and PBA-based cathode materials.[26]

	Mn-based ZIBs	V-based ZIBs	PBA-based ZIBs
Advantages	1. High working potential (~1.3 V); 2. Moderate theoretical capacity (~310 mAh g^{-1}); 3. Acceptable cycling performance (100~5000 cycles)	1. Diversity of V-based compounds; 2. Good cycling stability; 3. High theoretical capacity (~600 mAh g^{-1});	1. High working potential (~1.7 V);
Disadvantages	1. Poor rate stability;	1. Low working potential (0.6-0.8 V); 2. Toxicity;	1. Low theoretical capacity (~70 mAh g^{-1}); 2. Poor cycle performance; 3. Poor rate performance;

Manganese-based cathode materials

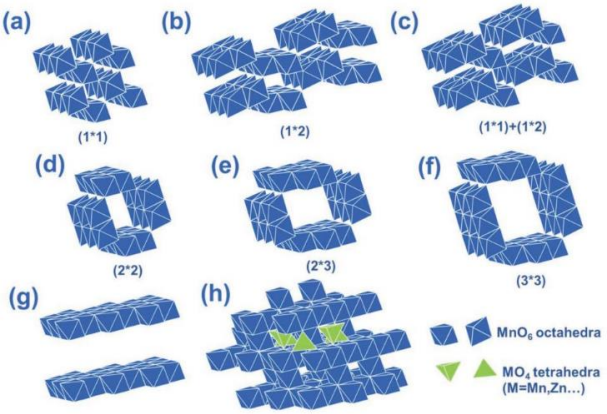

Fig. 1.11 Typical polyhedral crystal structures of manganese oxides: a) β-MnO_2; b) R-MnO_2; c) γ-MnO_2; d) α-MnO_2; e) romanechite-type MnO_2; f) todorokite-type MnO_2; g) δ-MnO_2; h) λ-MnO_2.[28]

Manganese-based oxides have the advantages of low-cost, abundant resource, low-toxicity, environmental friendliness and various valence states (for instance, Mn^{0}, Mn^{2+}, Mn^{3+}, Mn^{4+} and Mn^{7+}).[25] As for manganese oxides, they have many phases with various open crystal structures. For instance, the MnO_2 exist many polymorphs, their MnO_6 octahedra can be arranged by sharing corners in various ways, such as edges into chain, tunnel and layered types. And they also have different tunnel, layered and spinel structures. Figure 1.11 lists some types of manganese oxides.[28]

Vanadium-based cathode materials

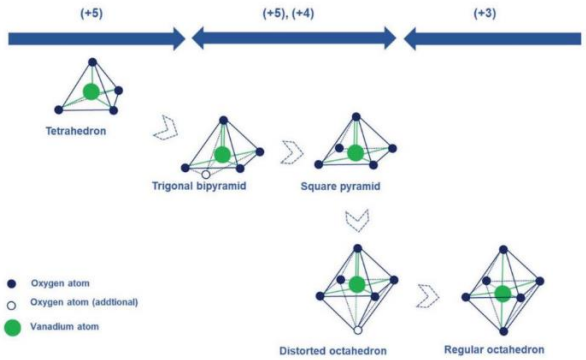

Fig. 1.12 Polyhedrons metamorphosis of crystal coordination in vanadium oxides. [28]

In terms of vanadium oxides, they also have plenty of phases. Their polyhedrons vary tetrahedron to distorted regular octahedra via square pyramid and trigonal bipyramid (Figure 1.12).[28] The different assembly formations and distortions result in diverse inner frameworks, which can accommodate zinc ions inside at different places reversibly. Except for vanadium oxides, vanadium-base derivatives also can be used as cathode materials in ZIBs, such as a series of $M_xV_2O_5$ compositions (M is alkali and alkaline earth metals).[26, 29]

Prussian blue-based cathode materials

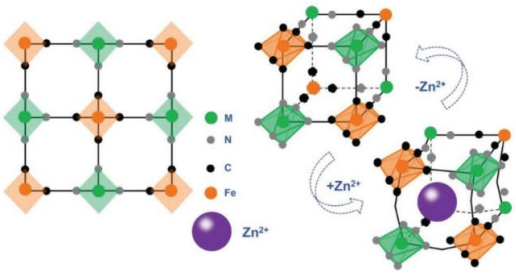

Fig. 1.13 Schematically crystal structure of PBAs $MFe(CN)_6$ (M is Fe, Co, Ni, Cu and Mn) with the insertion and extraction of Zn^{2+}.[28]

Like the Prussian blue analogues ($A_xMM'(CN)_6{\cdot}yH_2O$, wherein A is an alkaline metal ion or a water molecule, and both M and M′ are transition metals.) in rechargeable metal ion batteries, they also be studied in ZIBs due to the open crystal structures (in Figure 1.13)[28]. They are also fabricated with metal ions and organic groups liking in various ways. Zinc ions can intercalate into the metal-organic frameworks with a high potential, which can enlarge the voltage of the full battery, although they have low specific capacities. For instance, NiHCF, CuHCF and FeCHF with a typical cubic framework and ZnHCF with a rhombohedral crystal structure have been investigated as cathode materials in ZIBs.[27]

Anode materials

For anode material in ZIB, the conventional material is zinc foil because of its cheap cost, abundant resource, low toxicity and high electrical conductivity. Furthermore, the relatively high theoretical capacity of 820 mAh g^{-1} is enough to match the cathode. However, there are also some issues that should be handled, such as the corrosion of zinc foil and dendrite growth problem during cycling. Some efforts are devoted to promoting the development of anode. Some researchers introduce some compounds by mixing zinc powder with other kinds of materials, such as carbon black, conducting polymer and 3D rGO. For example, Kang's group mixed 12 wt% activated carbon with zinc particles, which exhibited better capacity retention (85.6% after 80 cycles) than that using unmodified zinc foil.[33] They found that the addition of activated carbon can suppress the formation of inactive basic zinc sulfates ($Zn_4SO_4(OH)_6{\cdot}nH_2O$) and accommodate the deposition of zinc dendrites and insoluble anodic products. Some articles also reported the deposition of zinc on hierarchical current collectors is a useful method to suppress the dendrite growth and improve electrochemical performance. They deposited zinc on all kinds of conducting materials, such as carbon fiber, 3D graphene foam and carbon cloth.[34-36] For instance, Fan's group designed a zinc nanoflakes array coated on 3D graphene foam.[36] The 3D graphene foam has high conductivity and its porous structure can be used to accommodate the dendrite growth. The Zn/GF exhibits lower charge-transfer resistance and electrochemical polarization in the cell than those of untreated zinc foil. And Tong's group reported the deposition of tiny zinc nanoparticles on N-doped porous carbon cloth.[34] The Zn/CC was directly used as freestanding anode, which displayed higher specific capacity and better cyclability than those of commercial zinc

foil. Moreover, the morphology of zinc anode is also an important factor to the electrochemical performance. For instance, Chen's group fabricated zinc anode by electroplating with organic additives in the plating solution.[37] The zinc anodes were synthesized with different crystallographic orientation and surface texture with the additives of cetyltrimethylammonium bromide (CTAB), sodium dodecyl sulfate (SDS), polyethylene-glycol (PEG-8000) and thiourea (TU). Zn-SDS, Zn-PEG, and Zn-TU displayed improved cycle performance than the commercial zinc foil. And Rolison and their co-workers fabricated a highly porous and 3D zinc sponge anode to enhance the zinc utilization and rechargeability.[38] The 3D structure minimizes the local current density with the large active area and suppress the zinc dendrite growth. Benefiting the control of void in 3D structure, the zinc sponge maintains a dendrite-free anode after 54,000 cycles and exhibits a high zinc utilization (~90 %). And some articles also reported the protecting layer (such as conducting polymer, carbonaceous materials and metal oxides) can improve the cyclability and specific capacity. For example, Mai's group deposited the protecting coating layer of TiO_2 on zinc foil via atomic layer deposition (ALD).[39] The TiO_2 coating layer suppresses the corrosion of zinc plate and dendrite growth, resulting in less gas evolution and $Zn(OH)_2$ byproduct formation.

Electrolyte

The conventional electrolyte in ZIBs is the aqueous solution, which has the advantages of abundant resource, high operational safety, high ion diffusivity, facile fabrication and environmental friendliness. However, the aqueous electrolyte has limited working potential, which is less than 2 V generally. Various zinc-salts are used in electrolytes, such as $ZnSO_4$, $Zn(CF_3SO_3)_2$, $ZnCl_2$, $Zn(NO_3)_2$, $Zn(TFSI)_2$ and $Zn(CH_3COO)_2$.[31, 40-41] The common used electrolytes are $ZnSO_4$ and $Zn(CF_3SO_3)_2$. The former is very cheap, and the latter can improve cycle performance. In general, they always be used with a concentration of 1~3 M. However, some literature reported the electrolytes with high concentration can promote the capacitance retention, such as the concept of "water-in-salt". The optimization of electrolyte is a very effective method to improve the electrochemical performance in ZIBs, including enlarge the working potential beyond the 1.23 V (the decomposition potential of water) and hinder the formation of zinc dendrite and irreversible ZnO. Wang's group introduced the modified high concentration electrolyte (1 M $Zn(TFSi)_2$ + 20 M LiTFSi).[42] This unique electrolyte not only enables dendrite-free Zn plating/stripping at nearly 100% columbic efficiency

(CE), but also retains water in the open atmosphere, which makes hermetic cell configurations optional. The pH value is also an important parameter to determine the performance. Most articles introduced that the mild acidic aqueous electrolyte is preferred to AZIBs, because the mild acid can restrict the formation of zinc dendrites and ZnO effectively. Qiao's group added 0.1 M H_2SO_4 into the electrolyte (1M $ZnSO_4$ + 1M $MnSO_4$) for AZIB.[43] The modified electrolyte with mild acid property can provide high output voltage of 1.95 V and an imposing gravimetric capacity of about 570 $mAhg^{-1}$ in electrolytic Zn–MnO_2 system. The introduction of mid acid electrolyte can also improve the capacity retention of 92% for 1,800 cycles. Simultaneously, some nonaqueous electrolytes are also considered, such as gel and solid-state electrolytes, but they show unsatisfied rate performance now.[44]

1.4 Introduction to in-situ mechanistic study of batteries

1.4.1 The current state of mechanism study

As our society is faced with continuously increasing energy demand and the rapid development of portable energy storage systems, the exploration of cheap and efficient energy storage techniques is urgent and significant. Although LIB technique has been studied tremendously and commercialized successfully, the optimization of LIB technique and development of next-generation batteries have become the new issues for researchers. Based on these problems, the understanding of energy storage mechanism is fundamental and significant.[1, 3, 45]

For the development of mechanism studies, the electrochemical principles of rechargeable metal ion batteries have been studied for several decades, which based on the mechanisms of non-rechargeable batteries and some commercialized rechargeable batteries, such as alkaline zinc-manganese battery, lead-acid battery and Ni-Cd battery. In terms of the conventionally commercialized LIB, the intercalation/ deintercalation of lithium cations in positive ($LiCoO_2$) and negative (graphite) materials crossing organic electrolyte and separator is its electrochemical principle. As for the optimization of LIB, it needs to investigate the energy storage with different electrode materials under diverse circumstances. As for the development of next-generation batteries, such as SIBs and ZIBs, researchers should investigate the electrochemical principles with different configurations and new kinds of metal cations, although their principles are similar.[5, 46-47]

In terms of the mechanism researches on rechargeable metal ion batteries, the main researches have transferred from macro electrochemical principles to some micro issues. Their main electrochemical principles are similar. The metal cations intercalate into and deintercalate from the electrode materials crossing the electrolyte during charge and discharge processes. However, there are still some micro issues needed to be investigated, such as the morphology and structural evolution, composition and crystalline transformation, surface and interfacial reconstruction and reaction intermediates during electrochemical processes. They are related to the optimization and realization of practical energy storage performance.[48]

Except for the researches on changes before and after charge or discharge processes, researchers shift many interests on the changes during charge and discharge processes in recent years. Some researchers study the equilibrium states of batteries with ex-situ characterization techniques under different electrochemical conditions. These ex-situ studies can be conducted with conventional characterization equipment. The samples are charged or discharged at different states, such as different potentials and current densities, and then they are disassembled from the batteries and measured with characterization techniques, such as XRD, Raman spectroscopy, XPS, FTIR and so on. This process is named ex-situ characterization, which studies the equilibrium states of samples during electrochemical reactions.[49] For instance, Sun and co-workers investigated the phosphorene-graphene hybrid material with ex-situ XRD technique.[50] The obtained composite consists of a few phosphorene layers sandwiched into graphene layers, which exhibited a high specific capacity of 2,440 mAh g^{-1}. The large capacity for SIB results from the formation of Na_3P composition through a dual storage mechanism of sodium ions insertion along with the x axis of the phosphorus layers, which was demonstrated with the ex-situ XRD characterization. They observed the composition changes at different potentials through the XRD method. Wang's group also used ex-situ Raman spectroscopy to study the structural changes of graphene at different sodiation conditions.[51] They synthesized the expanded graphene and used it as anode material in SIB. Raman spectroscopy is an effective and simple technique to study the structural vibration modes of graphene according to the intensity ratio between D and G bands. The observation of ex-situ Raman spectroscopy indicates the increment of structure randomness after sodiation. However, the characterization of equilibrium states needs to disassemble batteries and take out the samples, which possibly bring about some contaminants and be polluted by the outside environment, such as the oxidization by

oxygen and decomposition of electrolyte on the surface of electrodes. Thus, the continuous observation in cell directly under or close to the working conditions should be more persuasive and explicit.

As the rapid development of large-scale scientific facilities, some researchers can establish the in-situ/operando facilities to study the non-/quasi- equilibrium states of electrochemical processes under various circumstances with specially designed systems or cells. For example, Wang and co-workers studied the microstructure evolution and crystalline transformation of Sn nanoparticle with in-situ TEM during cycles.[52] They fabricated the nano-sized SIB with Sn nanoparticles. The two-step sodiation processes were observed directly. The crystalline Sn nanoparticle was sodiated to amorphous Na_xSn alloy via a two-phase storage mechanism, and then further changed to several Na-rich amorphous phases and finally to the crystallized $Na_{15}Sn_4$ (x = 3.75) via a single-phase storage mechanism. The in-situ TEM provides the visualized observation of phase and morphology evolution during electrochemical charge and discharge processes. And Gerbrand Ceder's group also devoted much effort to in-situ characterization techniques. They discovered the reversible O3–O'3 phase change of layered $NaTiO_2$ in SIB with in-situ XRD, which contains an unusual crystal structure evolution companied by complex Na vacancy coordination in a series of second order phase changes.[53] This is the reason to the excellent capacitance retention of layered $NaTiO_2$ in SIB. As for in-situ characterization techniques, some of them can be modified from conventional facilities with specially designed electrochemical cells. However, as the researches transferred from the surface to inner structures, some facilities cannot meet the requirements of some mechanism investigations, such as the low intensity of X-ray and poor sensitivity of detectors. Thus, some special in-situ characterization techniques need more advanced and designed facilities, such as synchrotron radiation-based characterization.

Synchrotron-radiation based characterization techniques have been utilized to mechanism study in recent years. The advantages of high brilliance, flux and good stability of synchrotron radiation can meet some special requirements of in-situ characterization.[54-55] For instance, Huang's group had utilized synchrotron radiation-based techniques to investigate many kinds of electrode materials in SIBs. They synthesized a kind of layered material of P2-$Na_{0.66}[Li_{0.22}Ti_{0.78}]O_2$ and used it as anode material in SIB, which exhibited good cycle performance.[11] In order to study the reason of excellent cycling performance, they studied the structure evolution with synchrotron radiation based in-situ XRD during cycles. The in-situ observation indicated the ~0.77 %

volume evolution during cycles, so the near zero-strain characteristic ensures excellent capacity retention. And Zulipiya Shadike and co-workers also investigated the reversible intercalation/deintercalation redox chemistries with synchrotron-based X-ray absorption near-edge structure.[56] They found the reversible anionic redox reaction of S^{2-}/S_2^{2-} in layered $NaCrS_2$ rather than Cr. The occurrence of Cr/Na vacancy antisite indicated the intercalation and deintercalation of sodium ions without changing its lattice parameter during cycles. Synchrotron radiation-based characterization techniques show the potential trend of characterization development. However, they are scare, and only several countries have the resource, which cannot meet the demand.[57]

In conclusion, the current state of mechanism study of rechargeable metal ion batteries is transferred from macro electrochemical principles to some micro changes, such as from electrochemical reactions to some practical optimization, from equilibrium states to non-/quasi- equilibrium states, from morphological changes to inner crystal structures and from electrochemical performance to fine transformation of materials. Thus, these trends also provoke the development of characterization techniques, more and more elaborate facilities are utilized in mechanism studies.

1.4.2 The in-situ characterization techniques for mechanism study

The urgency of promoting the electrochemical performance of LIBs and developing the next-generation energy storage systems need advanced characterization techniques. As the in-depth investigation of batteries, the researches have been developed from conventional characterization techniques to ex-situ equipment, to in-situ/operando facilities, even synchrotron radiation based larger-scale scientific facilities. In this part, some advanced characterization techniques will be introduced according to some mechanism studies, including the morphological and structural evolution, composition and crystalline transformation, surface and interfacial reconstruction.[48]

The morphological and structural evolution

Morphological and structural evolution is the basic change of electrode materials during cycles. As the intercalation and deintercalation of metal ions in the electrode materials, their structures will change simultaneously. The structure change is an important parameter to electrochemical performance, especially to the cycling performance. The severe expansion and shrinkage of electrode materials during cycles will damage the integrity and robustness of electrodes, and then result in poor

electrochemical performance. Some characterization techniques can be utilized to investigate the morphological and structural evolution during cycles.

Scanning electron microscope (SEM): The conventional and typical characterization technique for morphological and structural evolution is SEM, which is a kind of electron microscope that uses the similar principle with the optical microscope and utilize electron instead of natural light. The SEM can achieve the spatial resolution about 1 nm with recent development, which is an effective technique to observe the diameter of nanoparticles, surface morphology and 3D structures. Researchers always apply the SEM to investigate the morphological changes at different equilibrium states, which can provide clear and exact images. The in-situ SEM is developed in these years with designed electrochemical cells, which can explore the surface of electrodes under the electrons without damage and observe the evolution during cycles.

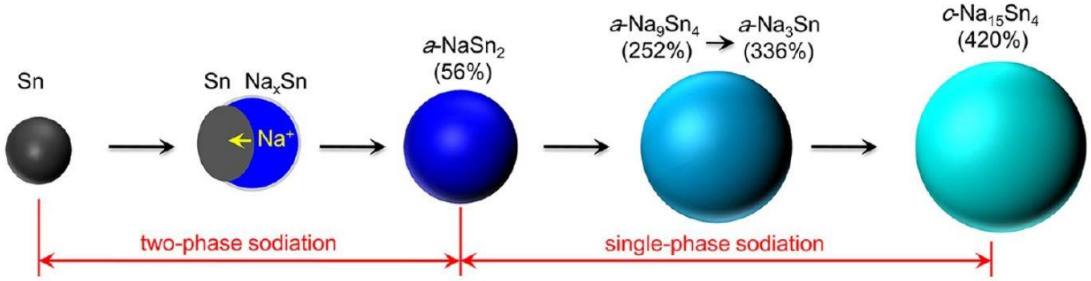

Fig. 1. 14 Schematic diagram of the composition and volume changes of Tin nanoparticles during the sodiation process.[52]

Transmission electron microscopy (TEM): TEM is also an effective technique to study the morphological and structural evolution, even its spatial resolution can down to the atomic scale. The electron density of TEM is much stronger than that of SEM. According to the transmission mode, the sample should be ultrathin (below 100 nm). The methodologies of TEM can be classified into three typical three kinds: imaging, diffraction and spectrometry according to the different information processing and presentation formations.[58-59] The conventional TEM equipment can be modified to in-situ TEM easily. Some researchers investigated the volume changes of alloying anode materials during cycles with the in-situ TEM. For example, Huang's group observed the volume changes during sodiation and desodiation processes.[52] They founded the two-step sodiation process: Tin first was sodiated to amorphous Na_xSn alloy ($x \sim 0.5$) with a volume expansion of 60 % and then further be sodiated into crystallized $Na_{15}Sn_4$ ($x = 3.75$) with a volume expansion of 420 % (Figure 1.14). This is very meaningful to observe and estimate the volume expansion directly. Moreover, the TEM has been

developed with more fine functions. For instance, the promoted scanning transmission electron microscopy (STEM) can provide structural, chemical and electronic information on an atomic scale, such as the atomic orientation and defects information. It also can be modified to in-situ mode. STEM has two kinds of modes, high-angle annular-dark-field (HAADF) mode and annular-bright-field (ABF) mode. The former is sensitive to heavy elements, the latter is effective to light atoms. The combination of these two modes can visualize the heavy and light atoms in one slot. Furthermore, some other characterization techniques can be modified in the STEM chamber, such as the element EELS, as the associated function, which can identify the chemical bonds and valence states. The combination of EDS can be used to observe the element distribution on the surface of the samples. These combined functions can provide more information and without other special equipment. As for the required cells for in-situ TEM, they contain the working electrodes coated with an ionic-liquid electrolyte or solid-state electrolyte and a counter metal electrode. Figure 1.15 exhibits the two types of in-situ TEM cells.[60-61] A bias potential is applied to the two electrodes to conduct the electrochemical processes.

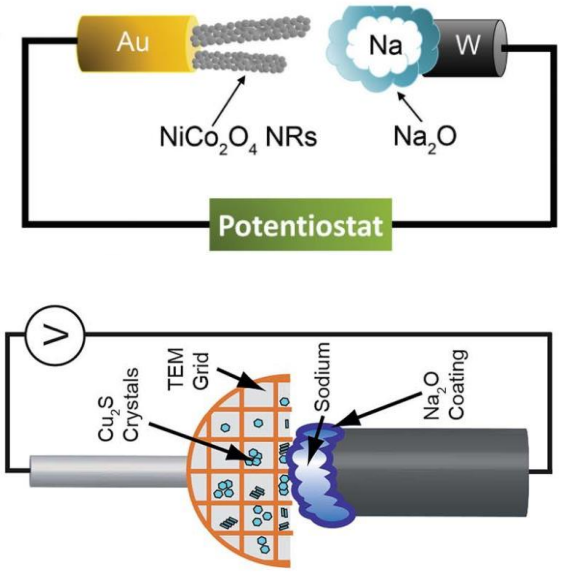

Fig. 1.15 Schematic diagram of the inner structure of in-situ TEM setups during cycle in SIBs.[60-61]

Atomic force microscopy (AFM): For the surface morphology of the sample, AFM is also an effective characterization method, which enables to provide the topography evolution information on the surface based on a tip-shaped cantilever. The surface evolution can be monitored with the line-by-line scanning mode. The Young's modulus of samples can also be obtained via the AFM method with two kinds of nanoindenters, pyramidal AFM tips and spherical colloidal probes. The real-time related information

can be obtained within designed cells. One simple cell is illustrated in Figure 1.16.[62] A voltage is applied to the two electrodes of sodium metal reference and working electrode, which are contacted on the same conductive foil. And the characterization environment is Ar-filled and should avoid the air and moisture insides. For example, Hu's group utilized the in-situ AFM to observe the morphology changes on the surface of the MoS_2 flakes.[62] They monitored the topographical evolution of solid-state interphase (SEI). They found the permanent wrinkling behavior of MoS_2 electrodes upon discharge to 0.4 V vs. Na^+/Na and estimated the thickness of SEI for the first time.

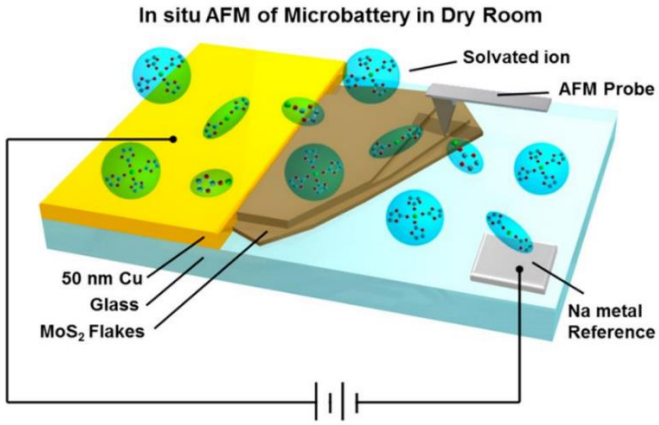

Fig. 1.16 Structure diagram of microbattery for in-situ AFM measurement within a liquid electrolyte and dry room environment.[62]

Composition and crystalline transformation

Although the electrochemical principles in rechargeable metal ion batteries are more and more clear in recent years, the reaction processes of different electrode materials are complex. The tendency of the mechanism study has been transferred from macro electrochemical principles to micro reaction processes. Thus, the investigations of the composition changes, phase transitions, crystalline transformations, crystal defects and reaction intermediates are meaningful to mechanism study. In terms of these investigations, they need some advanced characterization techniques.

X-ray diffraction (XRD): XRD is the common and simple method to study the materials, including the phase composition, crystal structure and phase purity. The ex-situ XRD can be conducted with conventional equipment directly, and the in-situ XRD can also be performed with these common machines, but with some specially designed cells.[63] Furthermore, the more advanced in-situ measurements are conducted with the synchrotron radiation-based facilities. As for the designed cell, one simple structure is presented in Figure 1.17.[64] Compared with the normal coin cells, the in -situ XRD cell needs some modifications. A Be sheet is attached to the bottom with a thermoplastic film

because of its high X-ray transmittance and enough electrochemical stability. The X-rays transmit to electrode materials through the holes on the shells and the Be window. For instance, Xu and co-workers observed the structural evolution and phase transitions of $Na_xCo_{1/3}Ni_{1/3}Mn_{1/3}O_2$ (NCM) with in-situ XRD technique.[65] They found the emergence of O3/O1 phases above 655 °C, while the P2/O3/O1 phases coexisted beyond 1000 °C. The O3/O1 phases disappeared below 364 °C during the cooling process and P2 and P3 phases are dominant further. Thus, the in-situ observation provides us the information of controlling the phases at a specific temperature, and this real-time observation cannot be obtained by conventional XRD, even ex-situ XRD. However, XRD characterization has some limitations, for example, it is difficult to obtain the information in amorphous materials. Thus, other advanced characterization techniques should be utilized combined.

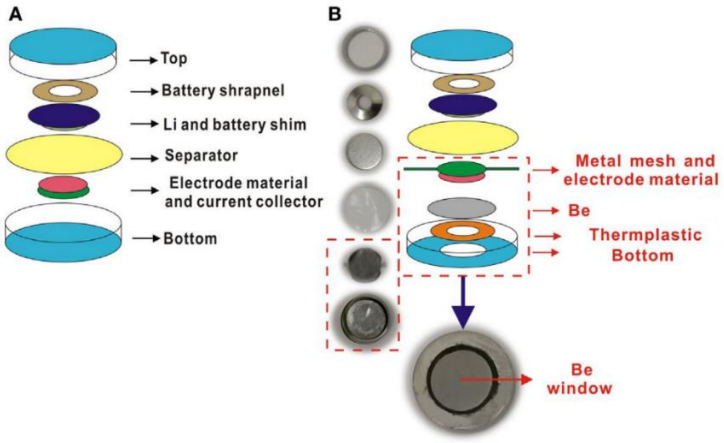

Fig. 1.17 Schematic illustration and real photos of conventional and in-situ coin cell. (a) Conventional coin cell and (b) in-situ XRD characterization coin cell.[65]

X-ray absorption spectroscopy (XAS): XAS is an effective technique to study the local symmetry and electronic structure. Compared with XRD, it can be used to study amorphous materials. The XAS can be classified into two types. The region near the absorption edge is named as X-ray absorption near-edge structure (XANES). The region above 40 eV is defined as extended X-ray absorption fine-structure (EXAFS). The former is an effective technique to study the oxidation states and the site-symmetry changes resulting from the absorbing atoms. The latter with stronger energy density can be used to obtain the quantitative local structural information, such as the degree of ordering, bond length and coordination number around the adsorbed atoms. And the XAS also be divided into hard X-ray absorption spectroscopy (HXAS) (> 5 k eV) and soft X-ray absorption spectroscopy (SXAS) (< 3 k eV) by the energy of X-ray resource. The former can be applied to obtain the information of valence states and the contribution from each

element in some multielement systems. The latter is sensitive to the elements and orbitals, so it can provide the information on occupied and unoccupied electronic states.[66] The modified in-situ XAS can investigate the valence state evolution and phase transition of both crystalline and amorphous materials within a working condition with specially designed cells. The simple illustration is presented in Figure 1.18.[67] The choices of appendant materials are severe, because some components can absorb the incident X-rays. For example, Zhou's group synthesized a series of cathode materials of $Na_{0.66}Co_xMn_{0.66-x}Ti_{0.34}O_2$ with the Co content increase from 0 to 0.33 for SIB.[68] They applied SXAS to study the evolution of valence states in the Mn and Co during sodiation and desodiation processes. They found that the substitution of Co can improve the valence state of Mn when the Co content is 0.22, which can suppress the Jahn–Taller distortion resulting from Mn^{3+} and protect the stability of P_2-type layered structure. The charge compensation phenomenon was demonstrated with the SXAS. XAS has another capability of detecting the surface and bulk information simultaneously through total electron yield and fluorescence yield modes, respectively.

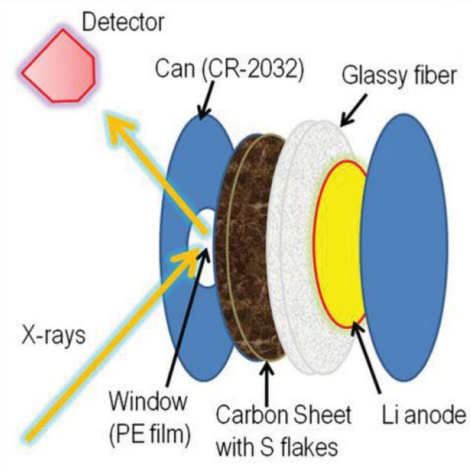

Fig. 1.18 Schematic diagram of in-situ coin cell for in-situ XAS measurement.[67]

Neutron diffraction: Neutron diffraction is also an effective approach to monitor the crystal structure and phase transitions, especially to the light atoms (such as H, Li and Na) and the elements with close atomic number (for instance, Ni, Fe and Co), even isotope. As for many electrode materials, they have close metal ions in the multi-metal oxides, they are difficult to be distinguished by some methods, such as TEM, but they can be monitored by neutron diffraction easily. The in-situ neutron diffraction equipment can be modified based on conventional equipment with specially designed cells. The simple setup is presented in Figure 1.19,[69] but they need to meet some requirements to

protect the diffraction from the disturbance resulting from current collectors, additive and so on. Thus, in-situ neutron diffraction is a significant technique to investigate the multi-metal oxides cathode materials. For instance, N.S.Nazer and co-workers conducted the in-situ neutron diffraction to study the crystal structure evolution of commercial graphite/(Ni, Mn, Co) oxides.[70] As for Ni, Co and Mn, they have close atomic numbers, neutron diffraction is effective to monitor them in the composite. The in-situ neutron diffraction revealed the structural change of graphite anode, which form a series of intercalation-type lithiated derivatives with a volume expansion up to 12.7 %. However, the neutron diffraction is mature, but the in-situ technique, especially the spallation neutron source is limited, and the spatial resolution of neutron is relatively low.

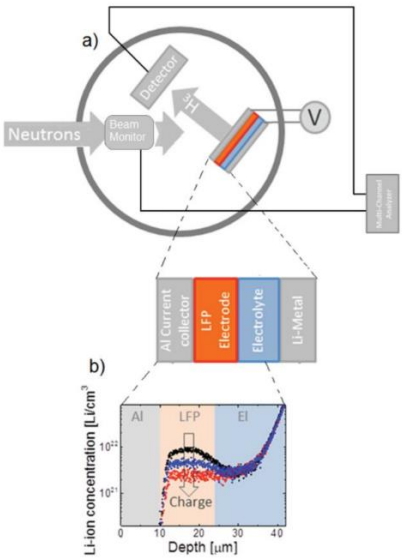

Fig. 1.19 a) The schematic diagram of neutron diffraction setup. b) The intensity distribution diagram of lithium elements within the inner structure of cell.[70]

Nuclear magnetic resonance (NMR) spectroscopy: NMR spectroscopy is an effective method to detect the local structural information, electronic structure and ion dynamics.[71-73] The NMR signal results from the movement of the nuclear spin angular momentum under an applied external magnetic field. A series of characteristic signals about the fine structural environment can be obtained according to the peak chemical shift, relaxation time, coupling constant and peak shape of the nucleus in NMR spectroscopy. The modified in-situ technique can study the real-time changes and non-equilibrium states, and it also can be utilized to most materials, including crystalline and amorphous materials, even liquid materials. The combination of NMR and isotopic elements can provide the diffusion information of metal ions in electrodes in detail. The designed cell is illustrated in Figure 1.20.[74] The in-situ cells are modified based on coin

cells, which utilize the copper mesh as the both current collector and NMR detector. The use of polymer bag can diminish the influence on NMR signals. And the cell should be located at NMR probe during testing. Clare P. Grey's group devote much effort to mechanism study in batteries with NMR spectroscopy. They conducted the solid-state NMR characterization with isotopic elements (^{23}Na and ^{31}P) to study the dynamics of $Na_3V_2(PO_4)_2F_3$ cathode materials in SIB.[75] They found that the sodium ions are removed nonselectively from the two distinct sodium sites of the fully occupied Na1 site and the partially occupied Na2 site. The mobility of sodium ion has been enhanced in the cathode material during the charging process, because the more sodium vacancies are formed. The rapid sodium motion can explain the good rate performance. The in-situ technique can provide fine information of atoms located at different sites in detail.

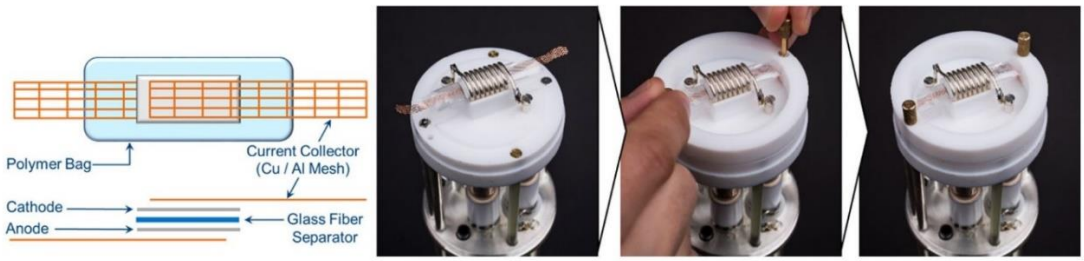

Fig. 1.20 Schematic inner configuration of a polymer bag cell and its setup for the in-situ NMR measurement.[74]

Surface and interfacial reconstruction

Batteries consist of several parts, such as anode, cathode, separator and electrolyte, they are assembled with a sequence and the metal ions shuttle through them. The diffusivity and mobility of metal ions in all kinds of electrodes, electrolytes and separators can influence the electrochemical performance, such as the rate and cycle performance. Thus, the observation and monitoring of surface and interface of them are important and significant to promote their performance. Their surfaces and interfaces will be reconstructed during cycles, which contain the solid electrolyte interphase, surface of electrodes and separators, growth of dendrites and so on. Some advanced characterization techniques are utilized to investigate them.

Raman spectroscopy: Raman spectroscopy is an effective technique to distinguish the structural evolutions and electronic properties on the surface according to the laser-induced vibrational, rotational and transformation modes. Researchers have done some work about the ex-situ Raman studies, but the surface of samples always be influenced by the environment, such as oxygen and moisture, the modified in-situ technique based on conventional equipment attract tremendous interests in recent years. The designed in-

situ cell is presented in Figure 1.21,[65] which is similar to in-situ XRD coin cell, except quartz window instead of Be window. The combination of in-situ Raman spectroscopy and electrochemical instrument, the continuous structure evolution has been obtained. The Raman spectroscopy enables to detect the vibration irrelevant to the central symmetry in some compositions. For example, Xie and co-workers synthesized a freestanding electrode of molybdenum disulfide nanosheets aligned vertically on carbon paper and studied its electrochemical properties in SIB.[76] They utilized the in-situ Raman spectroscopy to investigate the phase transition during sodiation and desodiation processes, because Raman technique is very sensitive to transition metal dichalcogenides. They found the reversible phase transition between 2H and 1T-phases inside MoS_2 during the insertion and extraction processes of sodium ions. However, sometimes the signal of Raman spectrum is weak and be disturbed by some components, such as electrolyte, so the combination with other characterization techniques is meaningful.

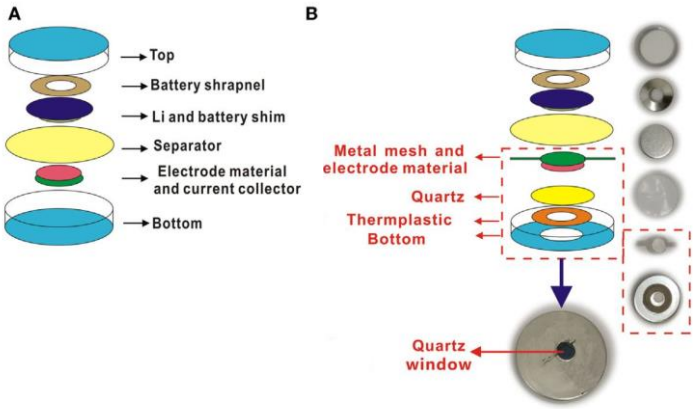

Fig. 1.21 Schematic illustration and real photos of conventional coin cell and in-situ coin cell. (a) Conventional coin cell and (B) the coin cell for in-situ Raman spectroscopy.[65]

Fourier-transform infrared (FTIR) spectroscopy: FTIR spectroscopy is also a surface-sensitive characterization approach. FTIR can provide the qualitative and quantitative information of the structure based on the infrared spectrum of absorption or emission of samples and the Fourier transformation. It can be applied to investigate solid, liquid and gas samples. FTIR can investigate the vibration associated with the symmetry of center, such as the chemical functional groups, while Raman spectroscopy cannot. Thus, the combination of FTIR and Raman measurements can provide abundant information of composition. In the mechanism study of batteries, in-situ FTIR can be applied to study the electrode or electrolyte materials during cycles, especially to the decomposition process of electrolyte. A simple configuration of in-situ cell is illustrated in Figure 1.22.[77] However, the in-situ FTIR technology is not mature for SIBs. For

instance, Mai's group utilized the ex-situ FTIR to detect the surface chemistry of $V_2O_5 \cdot nH_2O$ electrode material.[78] They found the red shift of the V=O stretching bond after a deep discharge, which indicated the reduction of V^{5+} to V^{4+}. While the unchanged vibration of V-O-V demonstrated the stability of layered vanadium oxide during cycles.

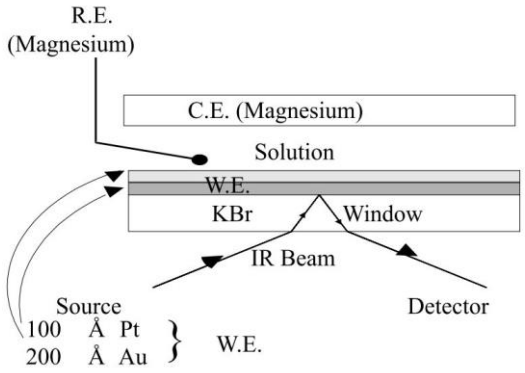

Fig. 1.22 Schematically inner configuration of an in-situ cell for in-situ FTIR characterization with the single internal reflectance mode.[77]

X-ray photoelectron spectroscopy (XPS): XPS is an effective method to study the surface chemistry, including the valence states and electronic structures of elements. It can quantitatively analyze the contents and ratios of elements within the depth of 2~5 nm. In terms of batteries, there are some electrochemical reactions insides that can be monitored by XPS exactly. XPS is a good method to study the SEI layer on the surface of electrodes.[79] For example, Soto and co-workers studies the SEI films on hard carbon in SIBs.[80] They analyzed the content changes of SEI with or without additives (FEC, fluoroethylene carbonate) in electrolytes. Combining the calculation, they can control the specific capacities of hard carbon via the controlled ratios of additives. However, the X-rays have some influence on the chemical states due to electron beam. And the in-situ XPS technique is difficult, because the severe measurement environment cannot meet the requirements of electrochemical processes. Thus, some in-situ investigations of valence states and electronic structures are conducted by in-situ XAS.

In conclusion, more and more advanced characterization techniques are utilized to investigate the fine mechanism during electrochemical processes. The conventional facilities are also modified and promoted to meet the demand of mechanism study. Real-time observation and analyses have attracted extensive interests in recent years. Except for the advanced characterization facilities, the material preparation and delicate design of cells are also important. And the combination of various characterization techniques is the tendency in near future.

Chapter 2 Experimental Methodology

The experimental methodology applied in this doctoral thesis will be introduced in detail, which contains the synthesis methods, material characterization and electrochemical measurements.

2.1 Synthesis methods

This chapter briefly introduces the synthesis methods applied to prepare the materials in this thesis. Each technique will be explained comprehensively below:

(1) Hydrothermal Method

Hydrothermal method is one kind of solvothermal technique, which uses the water as the solvent. It is one of the most general and effective synthesis methods to fabricate nanomaterials. During the fabrication process, the solvents with reactants are poured into an autoclave to carry out the reaction under suitable temperature and pressure for a period of duration. The source materials will decompose or react with each other under the specified temperature and pressure. The advantage of hydrothermal method is the ability to precisely fabricate many kinds of inorganics, for instance, metal oxides, sulfides and nitrides, with specified crystal structure, crystallinity, morphologies and size distribution via the elaborate control of precursor type, pH value, duration, reaction temperature, surfactant type and ratio of reactants. Moreover, the hydrothermal technique is also one of the simple and low-cost methods. In these experiments, hydrothermal method is used to synthesize powder and freestanding electrode materials. The active materials of MoS_2/graphene foam in chapter 4, $H_2V_3O_8$ and VOOH in chapter 5 were synthesized with the hydrothermal method.

(2) Chemical vapor deposition (CVD)

CVD is an effective method to the formation of active material on the substrate or on the precursor directly with a chemical reaction. The fabricated materials can possess good crystallinity and specified phase. In the synthesis process, the characteristics of products can be controlled exactly by some parameters, for instance, working temperature, pressure, gas flow and concentration. And the synthesis process can also be monitor and adjusted effectively. In our experiments, the Mo-based thin nanosheets @N-doped carbon in chapter 3 was synthesized via CVD method with different vapors. In chapter 4, the graphene foam was also fabricated with CVD method. The methane was

decomposed to carbon on the surface of nickel foam with designed flow rate and under the specific temperature. And the CVD technique is also served to substitute the sulfur atoms in MoS_2 with selenium elements.

2.2 Material characterization

In term of this chapter, the material characterization techniques used in these experiments will be introduced comprehensively. Each one will be explained below:

(1) X-Ray Diffraction (XRD)

XRD is a common and rapid analytical technique that can identify the crystal phase and structure, crystallinity, crystallite size of materials. X-ray striking an electron produces secondary spherical waves emanating from the electron, which is named elastic scattering. A few of the regular array of spherical waves have a specific direction, which can be identified by Bragg's law: $2d \sin\theta = \lambda$ (where d is the spacing between diffracting planes, θ is the incident angle, n is any integer and λ is the wavelength of the beam). According to the wavelength λ, researchers can obtain the information of atomic arrangement. In our XRD characterization in this thesis, a powder X-ray diffraction (XRD, Bruker D-8 Advance) has been used to characterize the samples.

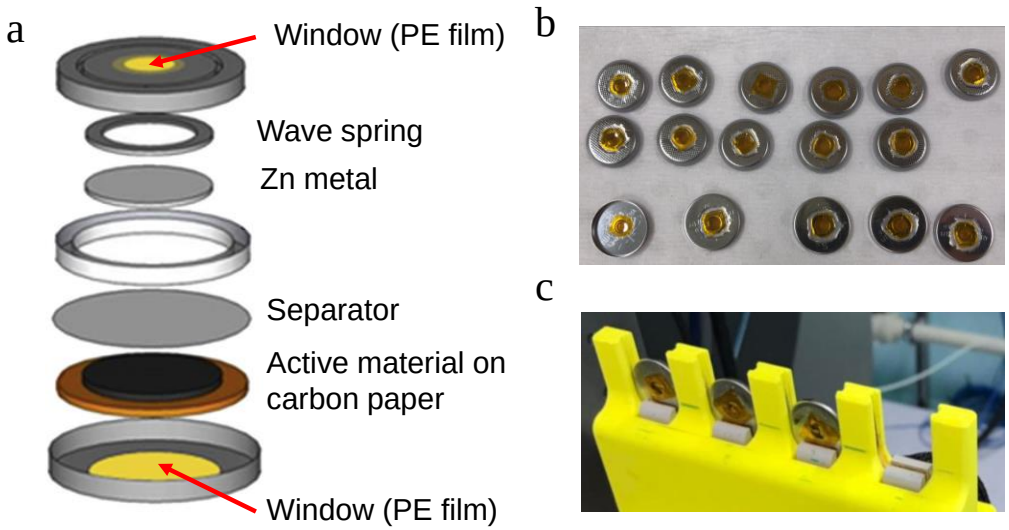

Fig. 2.1 (a) The inner structure, (b) the assembled in-situ XRD cell and (c) the cell mounted on a specially designed holder for the powder diffraction beamline.[81]

And the synchrotron-based in-situ XRD was also applied to investigate the composition changes and crystal structure evolution of electrode materials. The inner structure of in-situ XRD cell is illustrated in Figure 2.1 a. The slurry of active materials was coated on carbon paper, which can decrease the influence of X-ray beam. The holes

with PE film rather than steel shell can let the X-ray penetration easily. The assembled cells and setup of in-situ XRD measurement are presented in Figure 2.1 b and c, respectively. The XRD data were collected at the Australian Synchrotron with a wavelength (λ) of 0.6888 Å, using the NIST LaB6 660b standard reference material. In this thesis, the cell for in situ test was cycled at the current density of 50 mA g^{-1} within the potential range between 0.2 and 1.6 V (vs. Zn^{2+}/Zn).

(2) Scanning Electron Microscope (SEM)

SEM is one of the basic and regular characterization techniques to define the morphology of materials, which is a kind of electron microscope that can visualize the surface morphology of sample by scanning the surface with a focused electron beam. The images are determined mainly by the secondary electrons generating from atoms excited by the focused electron beam on the material surface with different intensities and directions. In this doctoral dissertation, the morphologies of the materials are featured by a field emission scanning electron microscope (FESEM, JEOL, Model JSM-7600F) coupled with EDX spectrometer.

(3) Raman Spectroscopy

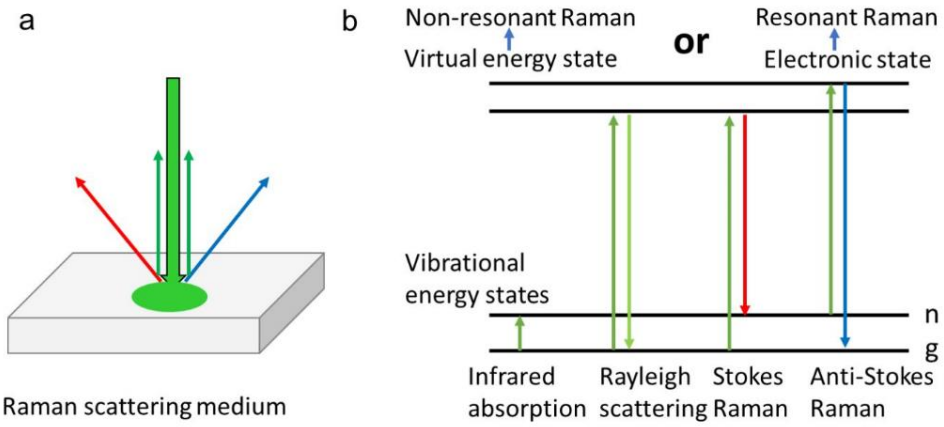

Fig. 2.2 (a) Light-matter interaction when a Raman scattering medium is illuminated by an electromagnetic field. The arrows with different colors representing different emitting signals, e.g. PL, Rayleigh scattering, Raman scattering etc. (b) Absorption and emission schematics in a typical Raman scattering process.

Raman spectroscopy is a characterization approach on the material surface, which is used to define the type of chemical bond derived from the inner molecular vibration modes. The Raman spectroscopy characterization technique is developed from the inelastic scattering of monochromatic light. The laser beam is the conventional monochromatic light. Figure 2.2 illuminates the light-matter interaction and several kinds of scattering light. Once the wavelength of vibration mode is closed to that of the

monochromatic light, it will produce Rayleigh scattering, which can provide the information of chemical bonds on the surface of samples.

In terms of the in-situ Raman spectroscopy characterization in this thesis, the conventional Raman equipment can be used directly with a special in-situ cell. The setup of in-situ Raman spectroscopy measurement is shown in Figure 2.3 a. The inner structure of the in-situ cell is illustrated in Figure 2.3 b. The cell has a hole with a quartz window on the shell, which can penetrate the laser light and scattering light. In this thesis, the conventional and in-situ Raman spectra were obtained via a WITec-CRM200 confocal microscopy Raman system with a 532 nm excitation source.

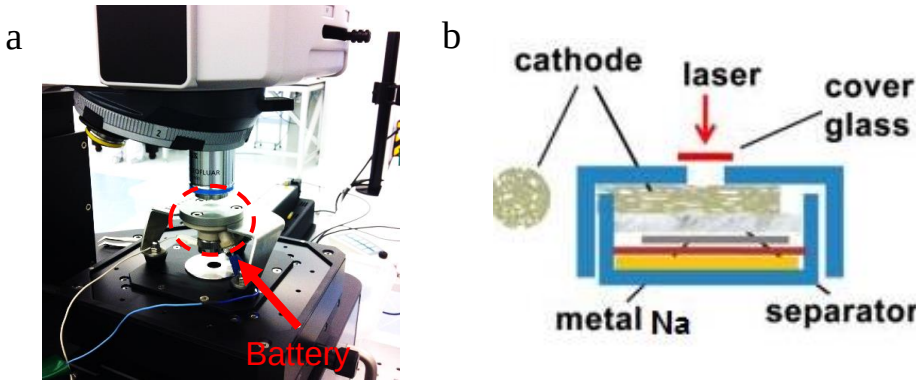

Fig. 2.3 (a) The setup of in-situ Raman spectroscopy measurement and (b) the inner structure of the in-situ cell.

(4) Transmission Electron Microscopy (TEM)

TEM is a kind of electron microscopy that can be employed to identify the morphology and crystallographic information via the interactions between the atoms in the sample and the high energy beam transmitting through the ultrathin specimen. TEM has the same principles as the light microscope but uses electrons instead of light, because the wavelength of employed electron beam is much smaller than that of light. Thus, it also can be used to feature the crystal dislocations and grain boundaries. The images of TEM are presented via the transmitted electrons on the phosphor screen or charge coupled device (CCD) camera. The selected area electron diffraction (SAED) also can be obtained with TEM by converging the electron beam over the selected area of the sample, which can produce a convergent electron beam diffraction pattern. The SAED can be applied to obtain the information of crystal structure and lattice parameters. And energy dispersive X-ray spectroscopy (EDS) can also be performed with TEM equipment, which is an analytic approach applied to identify the chemical analysis and element characterization. Its principle relies on the emitted X-rays excited by the high energy electron beam on the specimen. Researchers can obtain the chemical information

according to the comparison between the emitted spectra and the characteristic electromagnetic emission spectrum derived from each element. As for the TEM characterization in these experiments, a high-resolution TEM (HRTEM, JEOL, Model JEM-2100F) working with 200 *k*V was applied and elemental distribution analyses are conducted with attached EDS with the JSM 2100F. The specimens are made by dispersing in ethanol, and then coated on holey copper grids and dried at room temperature before testing.

(5) X-ray Photoelectron Spectroscopy (XPS)

XPS is a non-destructive characterization technique to quantitatively distinguish the chemical states and electronic states of the elements on the surface of specimens. The measurements of kinetic energy and number of electrons, escaping from the surface of samples (from 0 to 10 nm) irradiating with a beam of X-rays, can provide the XPS information. Every element with a specified valence state has its characteristic binging energy, which is the feature to determine its chemical and electronic states. Thus, researchers also can measure the element composition on the surface. Combining with some etching techniques, the chemical state information inside the sample can be studied further, especially some air-sensitive specimens. In this thesis, the XPS characterization is performed through a Thermo Fisher Scientific Theta Probe XPS system with a monochromatic Al Kα (1486.7 eV) X-ray source.

(6) Thermogravimetric Analysis (TGA)

TGA is one kind of thermal analysis method to characterize the mass change of sample along with the change of temperature. It can be used to identify the phase transitions, thermal decomposition, oxidation, solid-gas reactions and so on. Researchers also can determine the content ratios of composition because of the mass changes at different temperatures. In this thesis, the content ratios of composition were measured by a thermogravimetric analysis system of SDTQ600.

2.3 Electrochemical measurement

(1) The assemble of coin-type battery

Before measuring the electrochemical properties of batteries, the working electrodes should be prepared first. There are two types of electrode materials introduced in this thesis. One is active powder material. The standard slurry coating technique was employed to fabricate the working electrodes. Typically, the working electrodes are

prepared by casting a slurry on a clean metal foil current collector, which consists of the active material, carbon black and polyvinylidene fluoride (80: 10: 10 in weight) dissolved in N-methylpyrrolidone (NMP), and drying at 100 °C in a vacuum oven for 12 hours. Another one is freestanding electrode materials, such as active materials grown on substrate and a film derived from active materials, which do not need any additive and can be directly divided into slices with specified area as electrode. Their mass loadings are determined by a balance. As for sodium ion batteries, CR2032 coin-type cells are assembled in an Ar-filled glove box (Mbraun, Unilab, Germany). The moisture and oxygen contents in the glove box are below 0.1 ppm. 1 M $NaClO_4$ or $NaPF_6$ in ethylene carbonate-diethyl carbonate-fluoroethylene carbonate (1:1:0.02 in volume) and glass fiber are used as the electrolyte and separator, respectively. The slurry is coated on clean copper foil. Sodium foils serve as both counter and reference electrodes. As for aqueous zinc ion batteries, we can assemble the CR2032 coin-type cells in air instead of in the glove box. 2 M $Zn(CF_3SO_3)_2$ and glass fiber are served as the electrolyte and separator, respectively. The slurry is coated on clean titanium foil. And zinc foil is used as both counter and reference electrodes.

(2) Cyclic Voltammetry (CV)

CV is one of the common and simple electrochemical technique, which is conducted to study the kinetics and composition changes of electrochemical reaction process. In the CV measurement, there are usually three electrodes, which contains a counter electrode, working electrode and reference electrode. The working electrode is made of active material, and its electrochemical reaction process can be investigated by applying a linear and cyclic sweep voltage within a potential range in Figure 2.4 a. The potential is measured between the working and reference electrodes. The current is measured between the counter and working electrodes. The separate measurements of potential and current can guarantee their accurate measurements. By sweeping the voltage slowly, electrochemical reaction information may be extracted from a graph of potential versus current going through the working electrode. Figure 2.4 b shows the measured current versus the applied potential, where the i_{pc} and i_{pa} exhibit the peak cathodic and anodic current for a reversible reaction, respectively. Their reversible response of the electron transfer reaction is: $A + n\,e^- \leftrightarrow B^{n-}$. As for the reversibility of the electrochemical reaction, the ΔE_p is defined as: $\Delta E_p = |E_{pc} - E_{pa}|$, where $E_{pc}\ and\ E_{pa}$ are the peak potentials in the cathodic and anodic sweep. When the electrochemical process is

reversible, $\Delta E_p = 0.059 / n$ and it is independent of sweep rate. The shape and position of the redox peaks depend on both sweep rate and the kinetic parameters of the electrode reaction. In these experiments, the CV curves of batteries are conducted with an electrochemical workstation (CHI 760D, Chenhua, Shanghai).

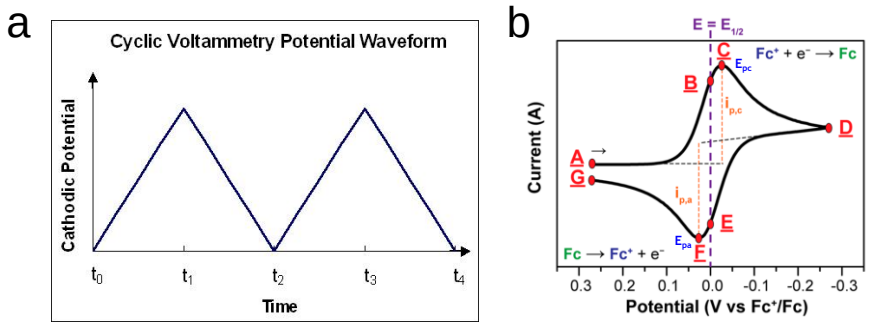

Fig. 2.4 (a) The applied linear and cyclic potential versus time and (b) the typical CV of measured current versus applied potential.[82]

(3) Galvanostatic Charge and discharge (GCD) measurement

GCD measurement is one of the simple and reliable technique to evaluate the electrochemical capacitance of electrode materials under controlled constant current conditions. In this measurement, a constant current is applied or released between the working and counter electrodes and its corresponding potential is detected against the reference electrode. Thus, the rate performance of electrode materials can be measured with different current densities, which is a significant parameter to the battery. During charge and discharge processes, the current always be expressed as a C-rate, calculated from the battery capacity. The C-rate is a measure of the rate at which a battery is charged and discharged relative to its maximum capacity. For instance, the 1 C is the necessary current applied or drained from the battery to completely charge or discharge in one hour. If the C-rate is 0.1 C, the necessary duration of complete charge or discharge is ten hours. The different current rates are illustrated in Figure 2.5 a. As for the calculation of capacity, the duration of charge or discharge step has been multiplied by the current applied during the process with the formula:

$$\text{Capacity: C (A} * \text{s)} = \int_{t0}^{t1} i(A) \cdot dt(s), C(A \cdot h) = C(A \cdot s)/3600(s) \quad (2.1)$$

$$\text{Specific capacity: C } (mAh \cdot g^{-1}) = C(A \cdot h)/m(g) \cdot 1000 \quad (2.2)$$

Energy density and power density are depicted as:

$$\text{Gravimetric energy density: E(Wh} \cdot Kg^{-1}) = \int_{t0}^{t1} i \cdot t \cdot dE/(2 \cdot m); \quad (2.3)$$

$$\text{Volumetric energy density: E(Wh} \cdot L^{-1}) = \int_{t0}^{t1} i \cdot t \cdot dE/(2 \cdot v). \quad (2.4)$$

Gravimetric power density: $\mathrm{P(W \cdot Kg^{-1})} = \int_{t0}^{t1} i \cdot dE/(2 \cdot m)$; (2.5)

Volumetric power density: $\mathrm{P(W \cdot L^{-1})} = \int_{t0}^{t1} i \cdot dE/(2 \cdot v)$. (2.6)

Where m and v is the weight and volume of the battery, respectively. The charge and discharge profiles are shown in Figure 2.5 b with different current densities. In terms of this thesis, the GCD measurements are carried out with a NEWARE battery testing system with different current densities at room temperature.

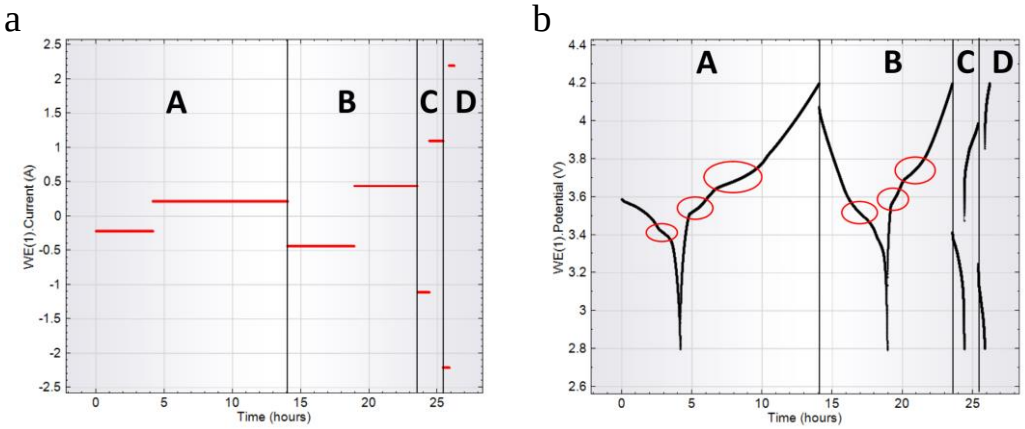

Fig. 2.5 (a) The applied current versus different duration at different C-rates and (b) the corresponding charge and discharge curves with different C-rates.

(4) Electrochemical Impedance Spectroscopy (EIS)

EIS is an important and significant electrochemical analytic technique to determine the resistance and impedance of the electrochemical working system. In general, an electrochemical cell can be considered an equivalent circuit of resistors and capacitors in Figure 2.6 a. The double-layer capacitance is nearly a pure capacitance, and hence it is represented in the equivalent circuit by an element C_d. And the resistance of electrode and solution is considered as R_Ω. The faradic process contains the redox reactions around the interface between the electrode and electrolyte. Because the faradaic process depends on the frequency (ω), it should be considered as a general impedance, Z_f. The faradaic process can be divided into two parts: charge transfer (a pure charge transfer resistance, R_{ct}) and mass transfer processes (a general *Warburg* impedance, Z_w) in figure 2.6 b.[82]

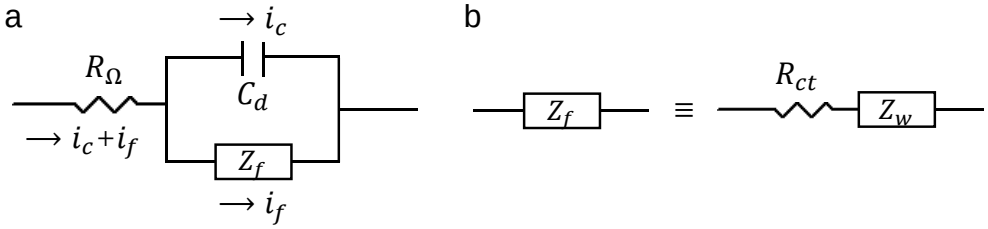

Fig. 2.6 (a) Equivalent circuit of an electrochemical cell and (b) the equivalent elements of Z_f.[82]

The Z_f can be expressed as:

$$Z_{Re} = R_\Omega + \frac{R_{ct}+\sigma\omega^{-1/2}}{(C_d\sigma\omega^{1/2}+1)^2+\omega^2C_d^2(R_{ct}+\sigma\omega^{-1/2})^2} \qquad (2.7)$$

$$Z_{Im} = \frac{\omega C_d(R_{ct}+\sigma\omega^{-1/2})^2+\sigma\omega^{-1/2}(\omega^{1/2}C_d\sigma+1)}{(C_d\sigma\omega^{1/2})^2+\omega^2C_d^2(R_{ct}+\sigma\omega^{-1/2})^2} \qquad (2.8)$$

σ is a parameter for the transfer process. The formulas can be considered at low-frequency and high-frequency. At very low frequency ($\omega \to 0$), the formulas can be expressed as:

$$Z_{Im} = Z_{Re} - R_\Omega - R_{ct} + 2\sigma^2C_d \qquad (2.9)$$

The plot of Z_{IM} versus Z_{Re} is linear and have unit slope, as shown in Figure 2.7 a. The linear correlation of Z_{IM} of Z_{Re} is characteristic of a mass-transfer controlled electrode process. At a high frequency, the relationship can be expressed as:

$$(Z_{Re} - R_\Omega - \frac{R_{ct}}{2})^2 + Z_{Im}^2 = (\frac{R_{ct}}{2})^2 \qquad (2.10)$$

The plot of this formula is exhibited in Figure 2.7 b. The center of the circular plot is at $Z_{Re} = R_\omega + R_{ct}/2$ and $Z_{Im} = 0$. The diameter is R_{ct}. This correlation is a charge-transfer controlled electrode process. The combined processes can be illuminated in Figure 2.5 c with kinetic controlled and mass-transfer controlled processes.[82]

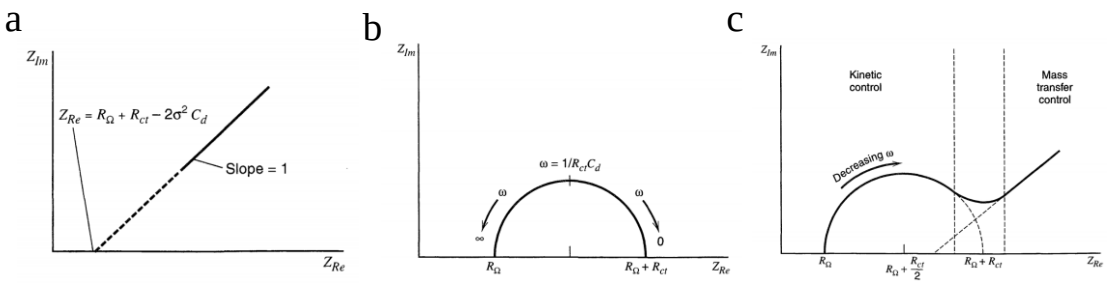

Fig. 2.7 Impedance plane plot for (a) low frequencies, (b) high frequencies and (c) combined two processes.[82]

The measurement is normally conducted by applying an AC potential with a sinusoidal potential excitation (usually 2-10 mV) to the electrochemical system and then recording the corresponding current signal through the system, which can be analyzed with a Fourier transformation. Simultaneously, the frequency of the applied potential is changed within a wide range (usually 0.1*M Hz* to 10 *m Hz*). The data will be processed by simulating the equivalent circuit in low and high frequencies and obtained the resistance and impedance of the electrochemical process. In terms of measurements in this thesis, the EIS is conducted to determine the interface resistance on the surface of the electrode, charge transfer resistance and the resistance of the working electrode. The

EIS measurements were carried out by applying an electrochemical workstation (CHI 760D, Chenhua, Shanghai) in the ambient environment.

(5) Galvanostatic intermittent titration technique (GITT)

GITT is one of the approaches to investigate the electrochemical thermodynamics and kinetics parameters of electrode materials during cycles. The measurement process contains a series of current pulses (transfer process), and each followed by a relaxation duration (diffusion process) without current pulses through the battery. The current pulses are positive and negative during the charge and discharge process, respectively in Figure 2.8 a. For instance, during the positive pulse, the potential of the cell will quickly increase to a value proportional to the inner resistance (R). And then the potential increase slowly due to the galvanostatic charge current. The metal ions maintain a constant concentration gradient inside the electrode materials. During the relaxation time, the current pulse is terminated, and metal ions tend to become homogeneous in the composition gradually. Simultaneously, there is an iR drop of the voltage. And then the voltage will decrease slowly until the concentration of metal ions in electrode becomes equilibrium (i.e., when dE/dt ~ 0) and the open circuit potential (V_{oc}) of the cell is reached. This sequence of charge pulse followed by a relaxation time is repeated until the battery is fully charged. A similar galvanostatic intermittent titration process happens during the discharging process until the battery is fully discharged.

The chemical diffusion coefficient can be calculated at each step with Fick's second law. Where i is the current (A); V_m is the molar volume of the electrode (cm^3/mol); z_A is the charge number; F is the Faraday's constant (96485 C/mol); S is the electrode/electrolyte contact area (cm^2); $dE/d\delta$ is the slope of the coulometric titration curve, found by plotting the steady state voltages E (V) measured after each titration step δ; $dE/d\sqrt{t}$ is the slope of the linearized plot of the potential E (V) during the current pulse of duration t (s).[83]

$$D = \frac{4}{\pi}\left(\frac{iV_m}{z_A FS}\right)^2 \left[\left(dE/d\delta\right) \Big/ \left(dE/d\sqrt{t}\right) \right]^2 \qquad (2.11)$$

If small enough current is applied for a short time interval, $dE/d\sqrt{t}$ can be considered linear and the coulometric titration curve can also be considered linear over the composition range involved in that step, the Equation can be simplified into:

$$D = \frac{4}{\pi\tau}\left(\frac{n_m V_m}{S}\right)^2 \left(\frac{\Delta E_s}{\Delta E_t}\right)^2 \qquad (2.12)$$

Where τ is the duration of the current pulse (s) and n_m is the number of moles (mol). ΔE_s is the voltage change of two adjacent steady-states, due to the current pulse and ΔE_t is the voltage change of the adjacent constant current pulse, eliminating the iR drop. These parameters can be obtained from the GITT curves directly, as shown in Figure 2.8 b.

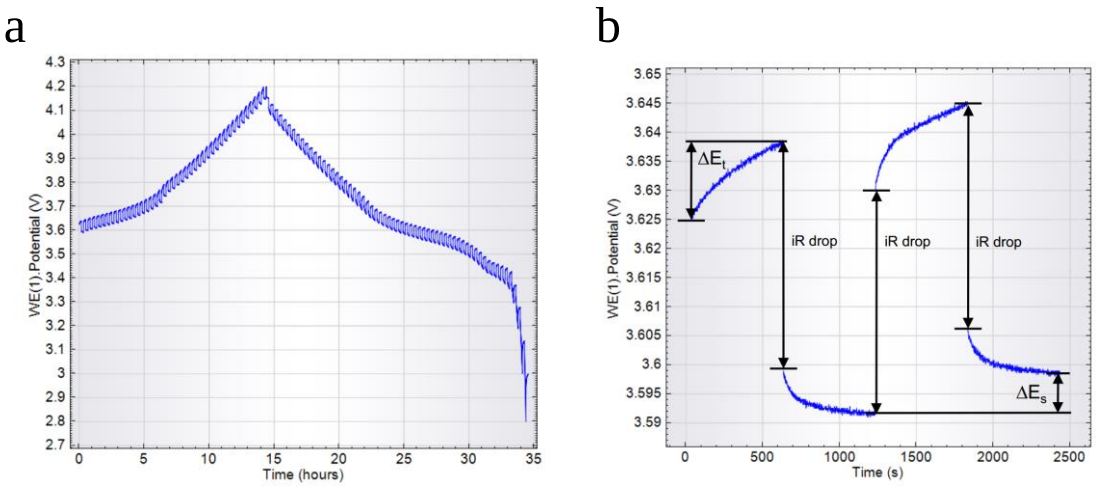

Fig. 2.8 (a) Galvanostatic intermittent titration curve with charge and discharge pulses and (b) the amplified curves.[83]

In these experiments, the chemical diffusion coefficients are conducted within half-cells, composed of metallic anode (as counter and reference electrode), electrolyte and working electrode (prepared with active material). The GITT was measured with a NEWARE battery testing system with a current density of 10 mA for 10 minutes followed by an interval of 30 minutes in room temperature.

Chapter 3 Mo-based Thin Nanosheets @N-doped Carbon Nanospheres for Sodium-ion Storage

Two-dimensional (2D) transition metal dichalcogenides are widely studied as anode materials for metal ion batteries. This application requires high electric conductivity which can be achieved by forming composites with conductive carbon. In this work, we demonstrate the creation of nanospheres composed of Mo-based thin nanosheets (MoS_2, $MoSe_2$ and Mo_2C) uniform embedded within a N-doped carbon matrix. Using $MoSe_2$/N-doped carbon nanospheres as example, we investigate in detail the electrochemical property in Na ion storage and reveal the advantage over previously reported $MoSe_2$ electrodes (higher capacity and improved capacity retention up to 500 cycles). Furthermore, we provide evidence by ex situ X-ray diffraction to the nominal irreversible conversion reaction during the first discharge.

3.1 Introduction and motivation

Sodium-ion batteries (SIBs), as the appealing candidate for lithium-ion batteries (LIBs), have drawn extensive attention recently. The potentially low price and earth abundancy of sodium salt, as well as the similar working mechanism to the state-of-art LIB, have motivated intensive exploration of suitable electrode materials and new battery structures for SIBs.[14, 47] Due to the larger radius of sodium ion (1.06 Å for Na^+ *versus* 0.76 Å for Li^+) and higher transport barrier compared with lithium ion, there still exists much difference between these two technologies in terms of electrode material selection and kinetics control.[5]

A judicious design of nanostructure and smart hybridization of the active materials are important to obtain high specific capacity and good cycling capability for rechargeable metal-ion batteries.[84-85] Recently, transition metal dichalcogenides (TMDs) with the formula of MX_2 have been widely studied as anode materials for LIBs and SIBs, because of their typical 2D layered structure and high theoretical capacities.[86-91] It is claimed that the stacked atom layers by weak van der Waals force allow favorable intercalation/deintercalation of metal ions between the layers.[87, 89] For example, MoS_2 as a typical TMD, has been demonstrated as a useful anode material for SIBs.[76, 92-93] $MoSe_2$, as the close 2D candidate to MoS_2, shows a graphene-like layered structure, larger

interlayer spacing (6.46 Å for $MoSe_2$ *versus* 6.2 Å for MoS_2),[94-96] higher electric conductivity and electrochemical activity, so it is also regarded a potential electrode material for SIBs. However, $MoSe_2$ have been scarcely investigated for SIBs.[97-100] The shuttle effect of polyselenides, similar with that of polysulfides in lithium-sulfur batteries, leads to the loss of active materials and fast capacity degradation.[98, 101-104] Furthermore, to improve the performance of $MoSe_2$ in SIBs, especially rate capability and cycle stability, it is necessary optimize the electrode structure design and form smart hybridization with conductive carbon.[105-107] Last, the commonly claimed conversion reaction in MoS_2 and in MoSe has not been verified.

Typically, the fabrication of active material with conductive shell (core/shell structure) can alleviate the shuttle effect and enhance the electric conductivity, but it is not an effective approach to accommodate the large volume expansion.[108-111] And the conductivity improves only at the surface of the active materials due to adhered conductive shell, but the conductivity of core part is still low. In view of these considerations, we propose a unique structure with uniform distribution of active materials in highly conductive matrix, which can meet the all needs.[112-115] Herein, we develop a generic method to synthesize Mo-based active materials dispersed in N-doped carbon matrix. Carbon is a kind of robust and conductive material, which can accommodate the large volume expansion of active materials better than metal oxides. Furthermore, the heteroatom doping, especially the nitrogen doping, can not only improve the conductivity of carbon, but also increases the reactive sites and decreases the energy barrier of ion diffusion.[116-117] Meanwhile, the nitrogen atoms can suppress the shuttle effect by bonding with poly-chalcogenides.[118] To date, the uniform distribution of Mo-based active materials in conductive matrix for SIBs has not been realized and reported.

In order to achieve the above design, we managed to achieve first Mo-polydopamine hybrid precursors, which are derived from dopamine-assisted self-assembly into a sea urchin-like structure. After a controlled calcination process, Mo-based nanosheets uniformly distributed in N-doped carbon matrix with the same urchin-like morphology are formed. As an example, the sodium ion storage properties of ultrathin $MoSe_2$/N-C are studied in detail. We attest that these composite spheres indeed show improved rate capability and cycling stability compared with pure $MoSe_2$ sample. It is reasonable to predict that the MoS_2/N-C sample will have similar enhancement. As for the Mo_2C/N-C, the electrocatalyst application will be studied and presented elsewhere. This work

provides the insight of fabricating the uniform distribution of active materials in conductive matrix for applications in catalysis and energy storage and conversion fields.

3.2 Materials preparation

Ultrathin Mo-based active materials/N-doped carbon nanosphere was prepared via the combination of a self-assembly method and a calcination process.

3.2.1 Synthesis of Mo-based precursor

For the synthesis of Mo-based precursor, we adopt the self-assembly method. 400 mg of the $(NH_4)_6Mo_7O_{24}\cdot 4H_2O$ (Sigma-Aldrich) and 25 mg dopamine hydrochloride (Sigma-Aldrich) were dissolved with 20 mL of distilled water at ambient temperature until an orange-red solution was formed. 40 ml of C_2H_5OH was added into the above solution. After continuously stirring for about 20 min, 0.3 ml of $NH_3\cdot H_2O$ (28 %) was added into the above mixture dropwise with continuous stirring. Then the precipitate was obtained by centrifugation after gentle stirring for 30 min, rinsed with ethanol and distilled water in turn for three times, and dehydrated in vacuum oven at 70 °C for 12 h.

3.2.2 Synthesis of Mo-based thin nanosheets @N-doped carbon nanosphere

In terms of the synthesis of Mo-based thin nanosheets @N-doped carbon nanosphere, a series of calcination processes with different conditions were applied. The $MoSe_2$/N-C was synthesized with a selenization process of Mo-polydopamine hybrid precursor using selenium as the Se resource at a temperature of 650 °C with a ramped rate of 10 min^{-1} and maintained for 3 h under a constant Ar/H_2 (98 %/2 %) flow (100 sccm). The MoS_2/N-C was fabricated with a sulfurization process using the sulfur as S resource and the same other conditions as the selenization process. The Mo_2C/N-C was obtained with the similar calcination process at 850 °C only using Mo-polydopamine hybrid precursor.

The pure $MoSe_2$ powder was synthesized by a hydrothermal reaction. 136 mg of Se powder was dissolved into 10 mL of $N_2H_4\cdot H_2O$ to form a red solution. Then the red solution was added into another solution dissolved 484 mg of $Na_2MoO_4\cdot 2H_2O$ into 50 mL distilled water and kept continuously stirring for about 30 min. Then, the mixture was transferred into an 80 mL Teflon-lined stainless-steel autoclave. The autoclave was kept at 200 °C for 24 h and then the powder was collected by centrifugation and rinsed three times with distilled water and ethanol. Finally, the as-synthesized sample was

obtained by drying at 70 °C in vacuum oven for 12 h and annealing at 650 °C for 3 h in Ar atmosphere.

3.3 Results and discussion

3.3.1 Materials characterization

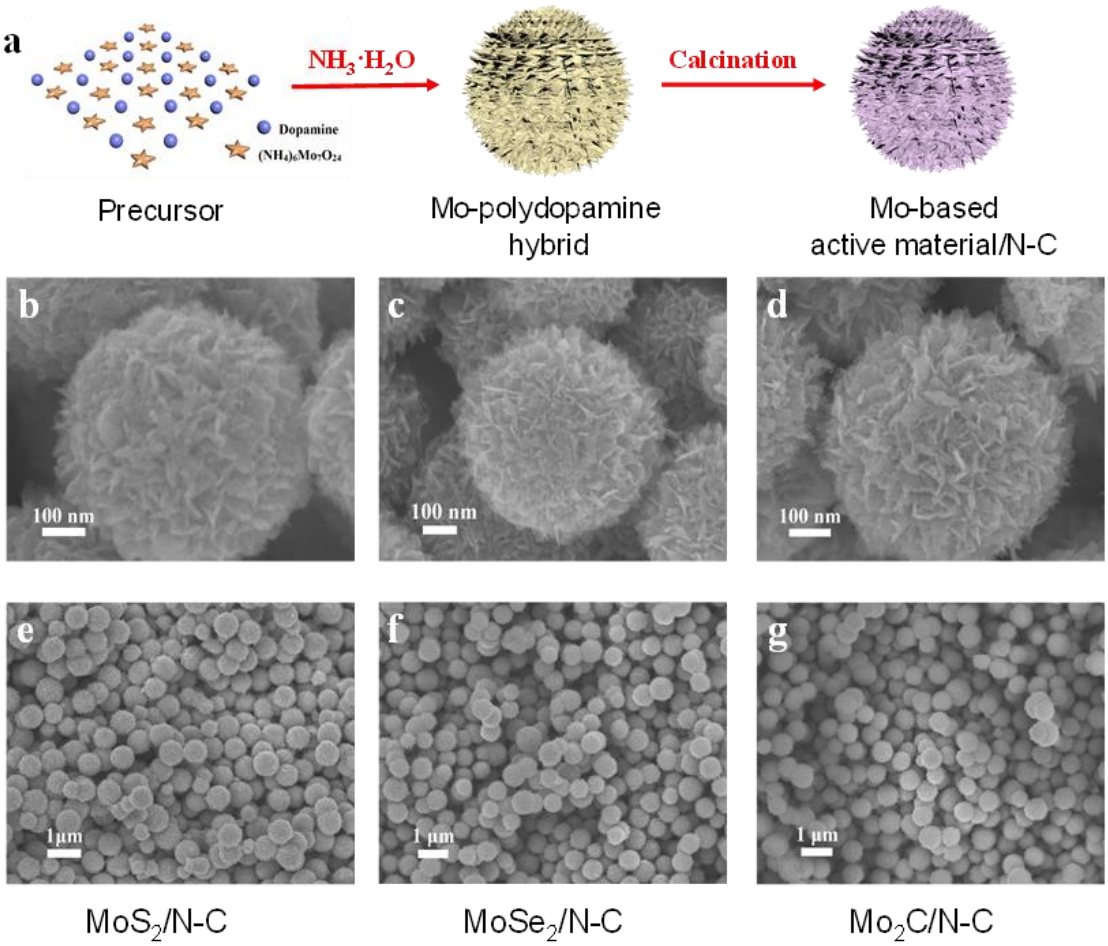

Fig. 3.1 (a) Schematic illustration for the preparation process of ultrathin Mo-based active materials/N-doped carbon nanosphere; SEM images showing the morphology of (b, e) MoS_2/N-C, (c, f) $MoSe_2$/N-C, and (d, g) Mo_2C/N-C.

The synthesis process of the ultrathin Mo-based active material/N-doped carbon nanosphere is illustrated in Figure 3.1 a. First, the Mo-polydopamine hybrid precursor was prepared with a simple chemical self-assembly method. The dopamine with rich catechol groups has an intriguing feature of complexation ability with various ligands, such as molybdate.[119-120] After simply mixing ammonium molybdate tetrahydrate ($(NH_4)_6Mo_7O_{24} \cdot 4H_2O$) with dopamine hydrochloride in aqueous solution, the oligomer of Mo-dopamine complex was synthesized due to the chelate interaction between the

catechol groups and the ligands of molybdate ions. The organic solvent ethanol can facilitate the uniform distribution of the Mo-dopamine complexes. After adding the polymerization initiator of $NH_3 \cdot H_2O$ dropwise, the self-polymerization process of dopamine molecules was triggered. The Mo-polydopamine hybrid precursors with nanosphere structure were formed with the self-assembly of the oligomers. Then the different kinds of ultrathin Mo-based active materials/N-doped carbon nanosphere (Figure 3.1 b, e for MoS_2/N-C; c, f for $MoSe_2$/N-C; d, g for Mo_2C/N-C) were obtained by the calcination of Mo-polydopamine hybrid precursor with different conditions, and the carbonization of the polydopamine occurred simultaneously.[121]

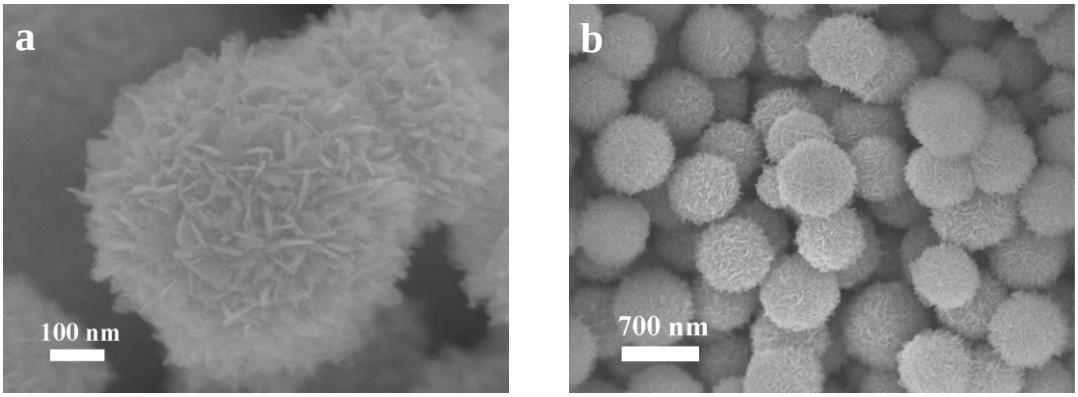

Fig. 3.2 Morphologies of Mo-polydopamine hybrid precursor with different resolutions.

The obtained Mo-polydopamine hybrid precursor, as depicted in Figure 3.2, has a uniform diameter distribution of around 600 nm with urchin-like structure, which was self-assembled with nanosheets and interconnected by polydopamine. Figure 3.1 b-g clearly show the morphologies of Mo-based active materials/N-doped carbon nanospheres, the size and urchin-like structure are preserved after calcination process at high temperature, which indicates its good structural integrity and mechanical stability. Ultrathin nanosheets with a width of around 10 nm could be observed on the surface, which can improve the approach of electrolyte and facilitate the intercalation and deintercalation of sodium ions in the composite. The uniform size could also be confirmed by the SEM images with a low resolution presented in Figure 3.1 e-g. As for the pure $MoSe_2$ powder, the morphology images are shown in Figure 3.3, which show aggregated structure with some flakes on the surface.

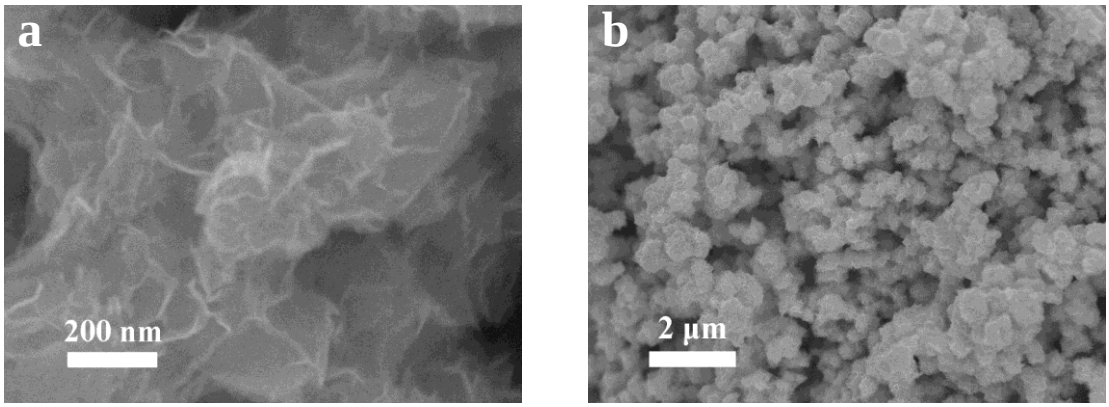

Fig. 3.3 Morphologies of pure $MoSe_2$ powder with different resolutions.

The $MoSe_2$/N-C with urchin-like structure and uniform size was further characterized by high-resolution transmission electron microscopy (HRTEM) illustrated in Figure 3.4 a and b. A representative HRTEM image (Figure 3.4 c) shows the ultrathin (2-4 nm) $MoSe_2$ active material with 3-5 layers and the lattice fringes with an inter-planar spacing of 0.648 nm, corresponding to the (002) crystal plane of $MoSe_2$.[115, 117]

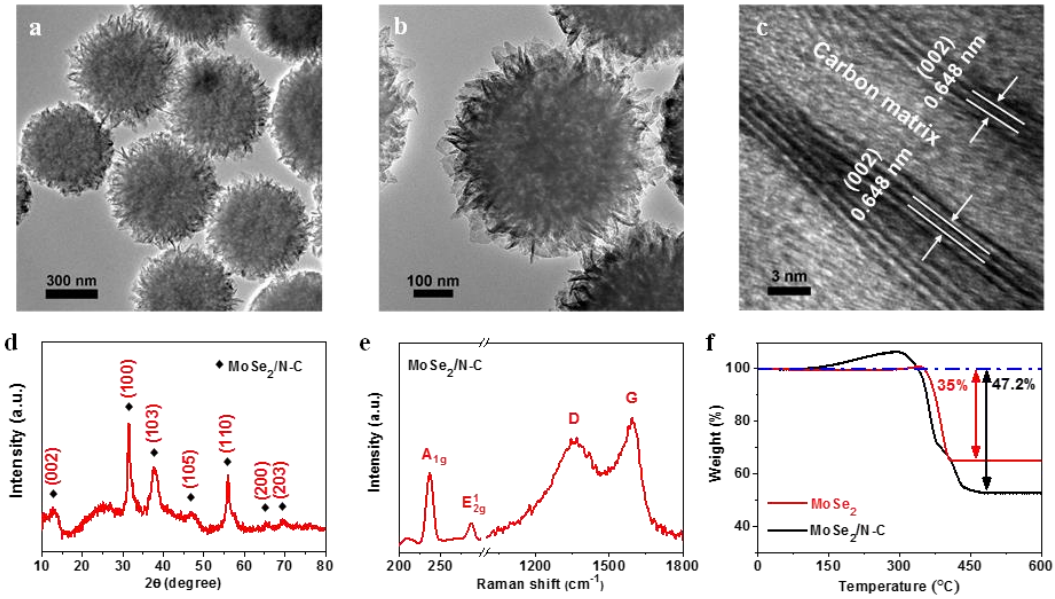

Fig. 3.4 (a-c) HRTEM images, (d) XRD pattern and (e) Raman spectrum of $MoSe_2$/N-C, (f) TG analyses of $MoSe_2$ and $MoSe_2$/N-C.

This urchin-like structure is further explored by the element mapping of the energy dispersive X-ray (EDX) analysis in Figure 3.5, which demonstrates the uniform distribution of $MoSe_2$ and N-doping in the composite. The uniform distribution of ultrathin active material in highly conductive matrixes is more beneficial than hierarchical structure, such as core-shell and core-branch structures, to the improvement of conductive connection and enhancement of electron transfer in the electrode materials.

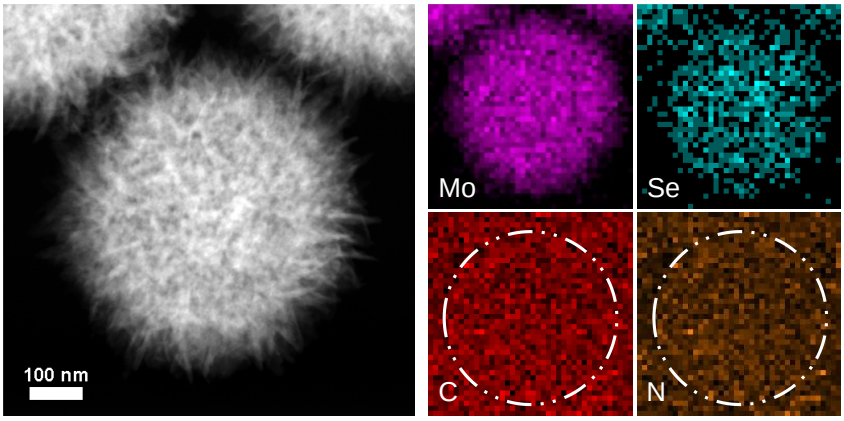

Fig. 3.5 Element mapping images of Mo, Se, C and N.

To confirm the phase and composition of the samples, X-ray diffraction (XRD), Raman spectroscopy and thermogravimetric (TG) analysis were performed. Figure 3.6 a shows the X-ray diffraction peak derived from Mo-polydopamine hybrid precursor. The MoS_2/N-C is demonstrated with good crystallinity (2H phase, JCPDS 37-1492) in Figure 3.6 b.[76, 93] X-ray diffraction peaks, shown in Figure 3.4 d and Figure 3.6 c, suggest the high crystalline structure of $MoSe_2$ (JCPDS 29-0914) with 2H phase, which is more stable than that of 1T phase.[97-98] The weak and broad diffraction peaks of carbon indicate its amorphous property in the composite. The Mo_2C/N-C with hexagonal crystal structure (JCPDS 45-1013) is also verified in Fig. 3.6 d.[122-123] From the Raman spectrum in Figure 2e, the characteristic peaks at Raman shifts of 236.5 and 287 cm^{-1} can be well indexed to the Raman vibrational modes of A_{1g} (out of plane) and E^1_{2g} (in plane) derived from $MoSe_2$, as well as the broad D and G bands at 1350 and 1579 cm^{-1} coming from carbon.[95-96] In comparison, the XRD pattern and Raman spectrum of pure $MoSe_2$ sample are presented in Figure 3.7 a and b.

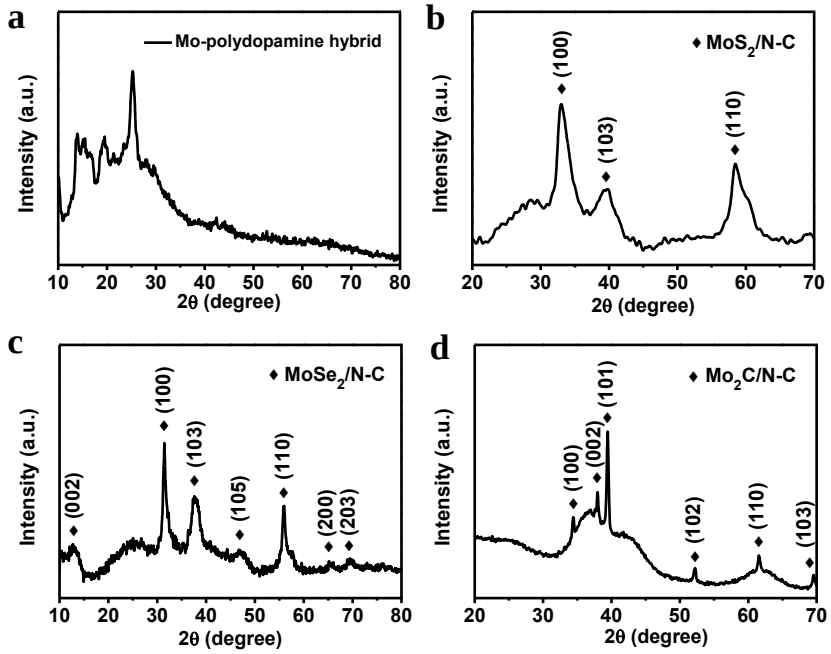

Fig. 3.6 XRD patterns of (a) Mo-polydopamine hybrid precursor, (b) MoS_2/N-C, (c) $MoSe_2$/N-C and (d) Mo_2C/N-C.

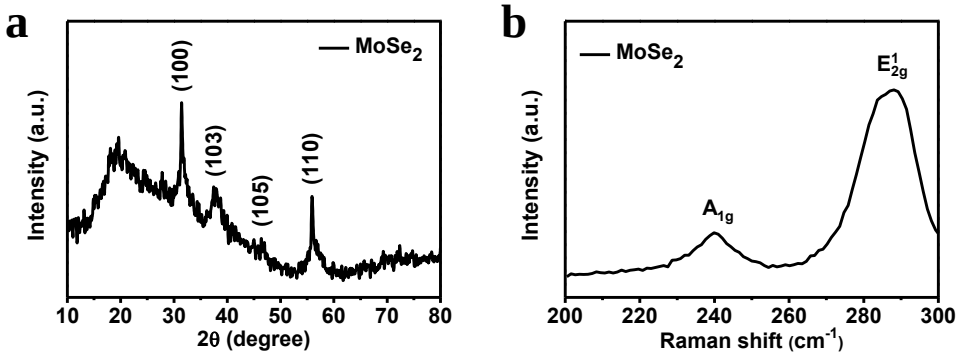

Fig. 3.7 (a) XRD pattern and (b) Raman spectrum of pure $MoSe_2$ powder.

Additionally, the accurate content of $MoSe_2$ in the $MoSe_2$/N-C composite was determined by the thermogravimetric analysis (TGA) under air atmosphere. In terms of the pure $MoSe_2$ sample, as illustrated in Figure 3.4 f, 35 % of weight is lost at around 400 °C owing to the reaction of $MoSe_2$ into MoO_3 in air. In contrast, the weight loss of $MoSe_2$/N-C composite is about 47.2 %, which contains the weight losses of $MoSe_2$ and carbon. After inverse derivation, the accurate weight percentage of $MoSe_2$ in the $MoSe_2$/N-C composite is 81.23 %.[99, 124] The high loading of active material in the composite is favorable for the practical application.

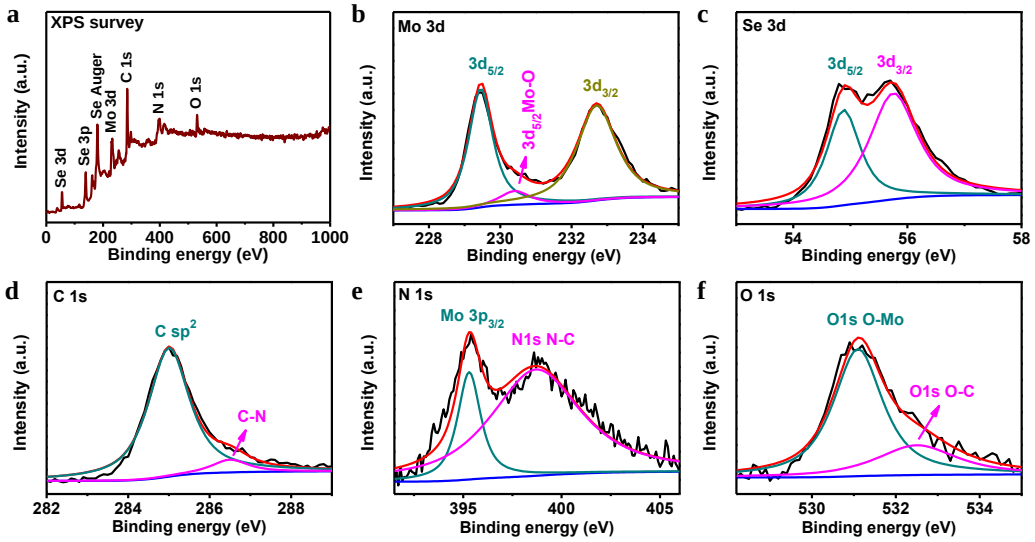

Fig. 3.8 XPS spectra of $MoSe_2$/N-C: (a) survey, (b) Mo 3d, (c) Se 3d, (d) C 1s, (e) N 1s and (f) O 1s.

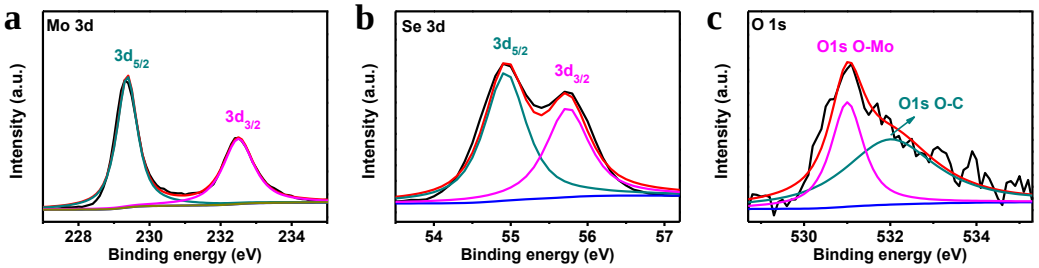

Fig. 3.9 XPS spectra of pure $MoSe_2$: (a) Mo 3d, (b) Se 3d and (c) O 1s.

As shown in Figure 3.8, X-ray photoelectron spectroscopy (XPS) measurement was used to investigate the surface elements of $MoSe_2$/N-C nanosphere. The survey scan spectrum detects the existence of Mo, Se, N, C and O elements. Two main peaks located at 229.5 and 232.6 eV are shown in Figure 3.8 b, which correspond to Mo $3d_{5/2}$ and Mo $3d_{3/2}$, respectively. And a weak peak with bonding energy of 230.4 eV is deconvoluted, which is assigned to the Mo-O bond because of the slight oxidation of $MoSe_2$ in air. For the Se 3d spectrum (Figure 3.8c), the observed bonding energies of 54.9 and 55.7 eV are attributed to the Se $3d_{5/2}$ and Se $3d_{3/2}$ in the $MoSe_2$.[97-98] The C 1s peak is detected at the bonding energy of 285.0 eV (Figure 3.8 d), the emergence of C-N peak at 286.5 eV demonstrates the existence of nitrogen doping in carbon matrix, and the N-C bond is also detected in Figure 3.8 e.[121] Two peaks of O-Mo and O-C are shown in Fig. 3.8 f, which are also the proof of the oxidation.[125] In addition, the XPS analyses of pure $MoSe_2$ sample are illustrated in Figure 3.9, which also demonstrate the composition and slight oxidation of $MoSe_2$.

3.3.2 Electrochemical analysis

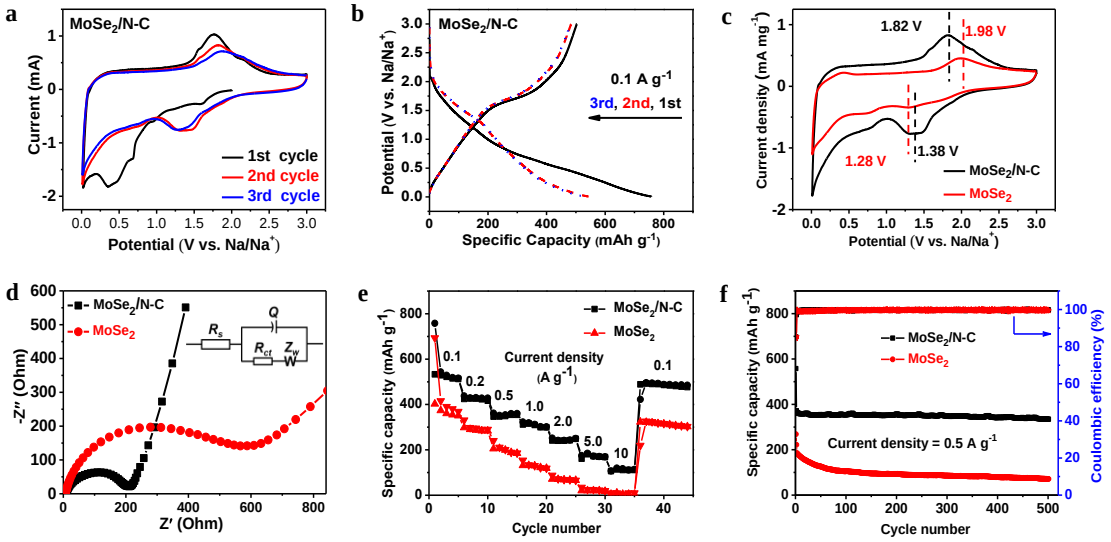

Fig. 3.10 Electrochemical properties of $MoSe_2$/N-C and pure $MoSe_2$ for SIBs between 0.01 and 3.0 V (vs. Na/Na^+): (a) CV curves with a scan rate of 0.1 mV s^{-1} and (b) charge-discharge curves at a current density of 0.1 A g^{-1} in the first three cycles for $MoSe_2$/N-C; (c) CV curves comparison at the second cycle for $MoSe_2$/N-C and pure $MoSe_2$; (d) Nyquist plots at 3.0 V after three cycles (the resistance is simulated using the same equivalent circuit inset in figure d), (e) rate capability with different current densities and (f) cycling stability at 0.5 A g^{-1} of $MoSe_2$/N-C and pure $MoSe_2$.

Detailed electrochemical measurements were conducted to investigate the sodium ion storage properties of $MoSe_2$/N-C nanosphere. Pure $MoSe_2$ powder was served as the control sample to reveal the advantage of uniformly distributed active materials in highly conductive matrix for electrochemical energy storage application. The typical cyclic voltammetry (CV) curves of $MoSe_2$/N-C nanosphere for the initial three cycles at a scan rate of 0.1 mV s^{-1} are depicted in Figure 3.10 a. A shoulder peak located at around 0.65 V in the first discharge process can be assigned to the intercalation of sodium ions in the 2D framework of $MoSe_2$, which leads to the formation of Na_xMoSe_2. And the broad peak observed at around 0.35 V is attributed to the conversion reaction from Na_xMoSe_2 to Mo metal nanograins accompanied by the formation of Na_2Se, which is similar with the sodiation behavior of MoS_2. The big irreversible capacity in the low voltage range (mainly below 0.5 V) also results from the formation of solid electrolyte interface (SEI) on the surface of electrode materials during the first cathodic process, which consumes Na. In the reversible charge and discharge processes, the anodic peak at around 1.82 V could be observed, which corresponds to the formation of Se by the oxidation of Na_2Se. The cathodic peaks blow 1.0 V shrink, but the new cathodic peak appears at ~1.38 V from the second cycle, which is due to the formation of Na_2Se with a similar mechanism

to that of Se-based active materials in SIBs.[104, 124] Starting from the second cycle, the CV curves almost overlap substantially, which suggests the good cycling reversibility of the composite.

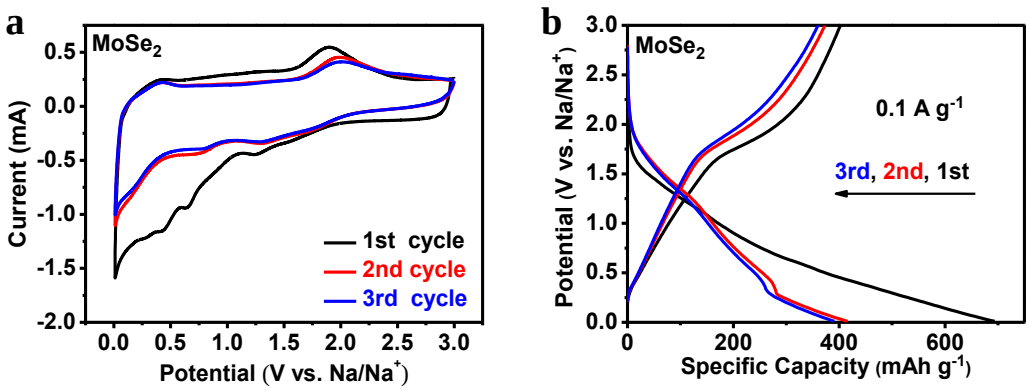

Fig. 3.11 (a) CV curves with a scan rate of 0.1 mV s^{-1} and (b) charge and discharge profiles at a current density of 0.1 A g^{-1} in the first three cycles for pure $MoSe_2$ electrode.

The CV curves of pure $MoSe_2$ electrode material are presented in Figure 3.11, which has similar sodiation/desodiation behaviors. The charge and discharge profiles of the $MoSe_2$/N-C nanosphere at a current density of 0.1 A g^{-1} in the potential range from 0.01 to 3.0 V (vs. Na/Na^+) are presented in Figure 3.10 b. The unapparent potential plateaus at around 1.38 V in the discharge processes are consistent with the cathodic peaks in CV curves. In the charge process, there is an obvious potential plateau at around 1.82 V, which in agreement with the anodic peak in CV curves. Similarly, the charge and discharge curves of pure $MoSe_2$ are displayed in Fig. 3.11 b, which are consistent with the CV curves in Figure 3.11 a. The $MoSe_2$/N-C nanosphere also shows better coulombic efficiency of 66.4 % than that of pure $MoSe_2$ about 58.0 % in the first cycle, which attests the enhanced reversibility of electrode material in this design.

However, the pure $MoSe_2$ has larger electrochemical polarization than that of $MoSe_2$/N-C nanosphere (see CV comparison in Figure 3. 10 c). The higher current density of ultrathin $MoSe_2$/N-C implies the higher electrochemical reactivity due to the introduction of highly conductive carbon matrix. And the pure $MoSe_2$ shows a pair of redox peaks at 1.28 and 1.98 V, which are wider than those of $MoSe_2$/N-C nanosphere at 1.38 and 1.82 V. The large electrochemical polarization indicates the slow charge transfer kinetics of pure $MoSe_2$, which reveals the kinetics enhancement and improved electrochemical reversibility.[97-98] In terms of the electrochemical impedance spectroscopy (EIS), as shown in Fig. 3.10 d, both samples exhibit a semicircle in high frequency region and an inclined line in low frequency region, which correspond to the

electrochemical reaction impedance (namely, charge-transfer resistance) in electrode and ion diffusion impedance in electrolyte, respectively. The simulated values of Ohmic resistance (R_s) and charge-transfer resistance (R_{ct}) for the $MoSe_2$/N-C nanosphere electrode are 5.4 and 198.6 Ω, respectively, which are lower than those of the pure $MoSe_2$ electrode (7.5 and 549.7 Ω). The lower impedance also reveals the improved charge transfer kinetics of the active materials.

The advantage of uniform distribution of active materials in conductive matrix is also verified by the rate capability and cyclic stability. Figure 3.10 e depicts the rate performance for the two types of electrode materials. The $MoSe_2$/N-C nanosphere electrode deliveries the specific capacities of 533, 426, 355, 310, 248, 180, 113 mAh g^{-1} at the current densities of 0.1, 0.2, 0.5, 1, 2, 5, 10 A g^{-1}, respectively, which are much higher than those of pure $MoSe_2$ electrode. The charge and discharge capacities recovered to the initial magnitude as the current density reduced back to the initial rate of 0.1 A g^{-1}, implying the good rate performance of the composite. To study the cycling stability, the two kinds of electrode materials were measured under a current rate of 0.5 A g^{-1} (Figure 3.10 f). The $MoSe_2$/N-C nanosphere delivers a high specific capacity of 558 mAh g^{-1} in the first discharge process, which is higher than that of pure $MoSe_2$ active material. Indeed, the $MoSe_2$/N-C nanosphere electrode outperforms most $MoSe_2$ composite electrodes in the literature (see detailed comparison in Table 3.1).

From the second cycle, the composite shows a high capacity retention of 89.8 % after 500 cycles. In contrast, the pure $MoSe_2$ electrode decays from 368 to 71 mAh g^{-1} after 500 cycles. The $MoSe_2$/N-C electrode exhibits better cycling stability than that of pure $MoSe_2$ active material for sodium ion storage. In addition, the SEM images (Figure 3.12 a and b) of $MoSe_2$/N-C electrode material after 500 cycles exhibits the better dispersion and morphological preservation of nanosphere structure than the pure $MoSe_2$ powder with severe agglomeration (Figure 3.12 c and d), except the destruction of nanosheets on the surface.

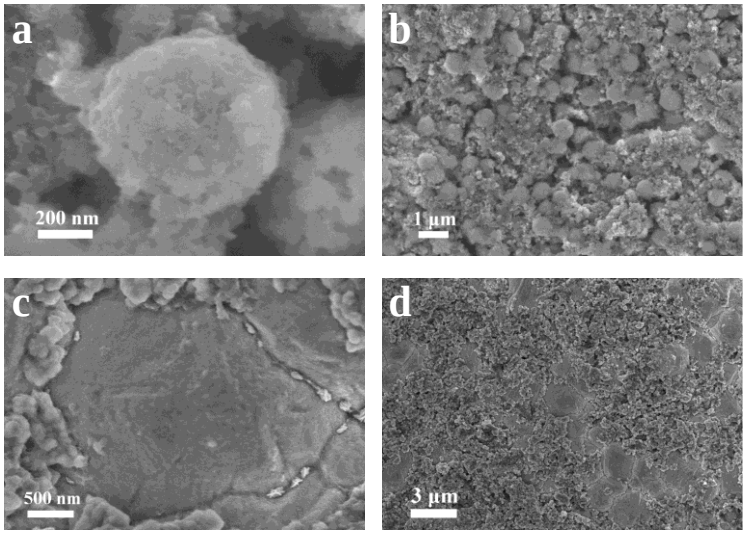

Fig. 3.12 Morphologies of (a, b) $MoSe_2$/N-C and (c, d) pure $MoSe_2$ electrode after 500 cycles at 0.5 A g^{-1}.

Table 3.1 A survey of electrochemical Na-ion storage properties of $MoSe_2$ and its composites measured in half cell (Na metal as counter electrode).

Electrode description	**Specific capacity** (voltage range)	**Cycling stability**
$MoSe_2$/N-C (this work)	533 mAh g^{-1} at 0.1 A g^{-1} (0.01–3.0 V)	89.8 % (334 mAh g^{-1}) after 500 cycles at 0.5 A g^{-1}
$MoSe_2$ yolk–shell microsphere[104]	448 mAh g^{-1} at 0.2 A g^{-1} (0.001–3.0 V)	82.2 % after 50 cycles at 0.2 A g^{-1}
$MoSe_2$ Nanosheets/rGO[126]	~490 mAh g^{-1} at 0.1 A g^{-1} (0.01–3.0 V)	430 and 380 mAh g^{-1} after 200 cycles at 0.5 and 1 A g^{-1}
$MoSe_2$ Nanospheres[127]	520 mAh g^{-1} at 0.04223 A g^{-1} (0.1–3.0 V)	80 % after 200 cycles at 0.04223 A g^{-1}
$MoSe_2$/carbon fiber[128]	452.6 mAh g^{-1} at 0.2 A g^{-1} (0–3.0 V)	85.5 % after 100 cycles at 0.2 A g^{-1}
$MoSe_2$@porous hollow carbon spheres[99]	575 mAh g^{-1} at 0.2 A g^{-1} (0–3.0 V)	580 mAh g^{-1} after 100 cycles at 0.2 A g^{-1}
$MoSe_2$/hollow carbon fiber[129]	---	423 and 395 mAh g^{-1} after 100 cycles at 0.5 and 1 A g^{-1}
$MoSe_2$ nanoplates[100]	513 mAh g^{-1} at 0.04223 A g^{-1} (0.1–3.0 V)	71.9 % after 50 cycles at 0.04223 A g^{-1}
$MoSe_2$/CNTs[124]	~450 mAh g^{-1} at 0.2 A g^{-1} (0.01–3.0 V)	102.0 % after 90 cycles at 0.2 A g^{-1}

3.3.3 Investigation of the storage mechanism

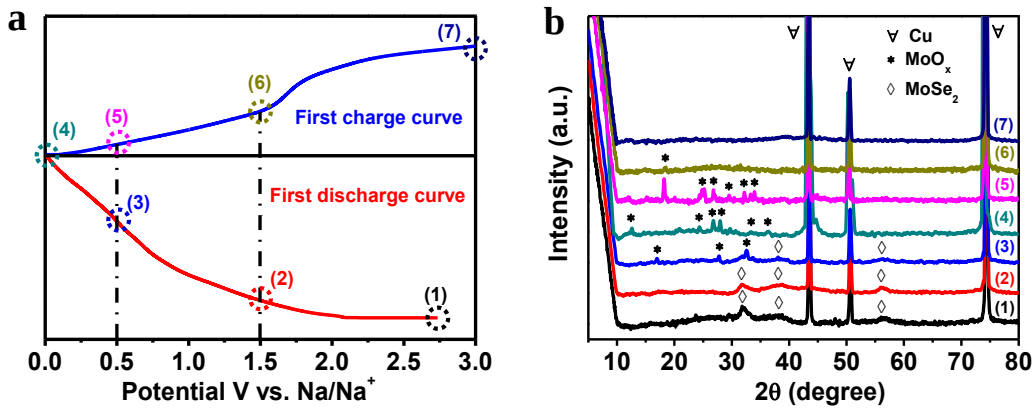

Fig. 3.13 Ex-situ XRD measurements at different potentials. (a) The discharge and charge profiles at a current density of 0.1 A g^{-1} and (b) ex-situ XRD patterns at the corresponding potentials in the first cycle for $MoSe_2$/N-C electrode.

Finally, the sodium ion storage mechanism of $MoSe_2$ was investigated by ex-situ XRD to the $MoSe_2$/N-C electrodes. For this measurement, six cells made from identical electrodes were stopped at different potentials in their first discharge and charge processes (see Figure 3.13 a), and then disassembled in the Ar-filled glove box. The $MoSe_2$/N-C electrodes were rinsed with diethyl carbonate (DEC) and dried in the vacuum chamber completely. Their corresponding XRD patterns are depicted in Figure 3.13 b. When the electrode is discharged to 0.5 V, the intensities of characteristic peaks of $MoSe_2$ decrease greatly, and the peaks of molybdenum oxide start to appear. When further discharged to 0.01 V, the $MoSe_2$ peaks vanish completely, while only peaks of molybdenum oxide exist. During the discharge below 0.5 V, the $MoSe_2$ is converted to elemental Mo and Na_2Se.[93, 98] So the oxide should result from a rapid oxidation of the nanostructured elemental Mo in the air during XRD measurement. When the electrode was charged back from 0.01 V to 3.0 V, the diffraction peaks of $MoSe_2$ could not be detected anymore, and some obvious peaks due to molybdenum oxide remains. This implies that the material after the full charging is no longer a layered $MoSe_2$ nor a Na-intercalated $MoSe_2$. The result above verifies the irreversible conversion reaction of $MoSe_2$ during the first cycle, and implies that the subsequent Na-ion storage process should be based on an alloy reaction between Se and Na.[98, 130]

3.4 Conclusion

The generic method of synthesizing Mo-based thin sheet materials ($MoSe_2$, MoS_2, and Mo_2C) within N-doped carbon composite nanospheres has been demonstrated. The formation process is determined to be induced by polydopamine assisted self-assembly, which also provides N-doping in the carbon. The uniform embedding of nanosheets within the conductive carbon matrix renders enhancement in the charge transfer and the sodiation/desodiation kinetics. In particularly, the $MoSe_2$/N-C nanospheres, as the anode materials, are introduced into Na-ion batteries, which exhibit a high capacity of 533 mAh g^{-1} (at 0.1 A g^{-1}) and long cycle stability (a capacity retention of 89.8 % after 500 cycles at 0.5 A g^{-1}). We also provide evidence to the charge storage mechanism, which is irreversible decomposition reaction during the first discharge followed by reversible Na-S alloy reaction. Our study may provide a promising strategy toward high-performance battery electrodes through smart hybridization of active nanomaterials with carbon.

Chapter 4 Selenium Substitution of $MoS_{2-x}Se_x$ for Sodium-ion Storage

Two-dimensional (2D) layered transition-metal dichalcogenides has been regarded as promising electrode materials for fast-rate Li-ion and Na-ion batteries. Monolayer or multilayer MoS_2 nanoflakes have been employed for metal ion batteries but the material suffers from poor cyclic stability due to damage of the layered structure in a decomposition reaction. Herein, we synthesize ultrathin $MoS_{2-x}Se_x$ nanoflakes quasi-vertically aligned on the graphene-like carbon foam (the obtained material is referred to as $MoS_{2-x}Se_x$/GF) and investigate the Na-ion storage property using in-situ Raman spectroscopy and ex-situ XRD measurements. We show that by choosing appropriate potential range, it is possible to maintain the 2D layered structure and thus significantly improve the capacity retention due to the intercalation mechanism. As a freestanding electrode, the $MoS_{2-x}Se_x$/GF demonstrates high-rate reversible Na-ion storage, where both the capacity and rate-performance are enhanced by the selenium substitution. This study sheds new light on better understanding of the metal ion storage mechanism of 2D transition metal chalcogenides that are being widely investigated.

4.1 Introduction and motivation

In the pursuit of the large-scale energy storage systems, sodium-based energy storage devices, such as sodium-ion batteries (SIBs), sodium-sulfur batteries and sodium ion capacitors, have drawn enormous attention recently. SIBs have been investigated as promising alternative to lithium-ion batteries (LIBs) due to lower cost of sodium salt and similar processing technology as LIBs. In comparison with the ionic radius of lithium ion (0.67 Å), the larger sodium ion (1.06 Å) leads to inferior electrochemical performance, resulting from its sluggish ion transport kinetics in the crystal structure. Furthermore, the large ionic diameter also results in severe structural distortion of the active material accompanied by phase changes or structural pulverization.[85, 131] Current research efforts are being devoted to development of new electrode materials and surface engineering to improve the rate and cycle performance.

2D layered transition metal dichalcogenides (TMDs) have been intensively investigated as anode materials in LIBs and SIBs, because they have larger lattice

spacings than the diameters of Li^+ and Na^+ and their electrochemical potentials of storing Li^+ and Na^+ are mainly below 2 V, which is relatively lower than those of cathode materials at about 4 V.[84, 92-93, 132] Among them, MoS_2 has been leveraged as the anode material in SIBs, because of its high theoretical capacity (~670 mAh g^{-1}, based on 4 mol of Na^+ insertion) and small lattice expansion during sodiation and desodiation processes.[133-134] However, the cycling performance of MoS_2 anode material in SIBs has been poor, for which an accepted reason is the irreversible decomposition reaction during the first discharge to a low potential region. It has been proposed that the sodiation mechanism of MoS_2 proceeds in two stages,[93, 135] and the corresponding reaction can be written as:

$$\textit{Stage 1:} \quad MoS_2 + x\,Na^+ + x\,e^- \leftrightarrow Na_xMoS_2 \qquad (4.1)$$

$$\textit{Stage 2:} \quad Na_xMoS_2 + (4\text{-}x)\,Na^+ + (4\text{–}x)\,e^- \rightarrow Mo + 2\,Na_2S \qquad (4.2)$$

In the high potential range, sodium ions first intercalate into the lattice (Eq. 4.1), followed by decomposition reaction in the low potential range (Eq. 4.2). During the first sodiation process, MoS_2 decomposes to metallic Mo, which is regarded as the main cause to poor cycle performance. Maier and coworkers prepared the single-layered ultrasmall MoS_2 nanoplates embedded in thin carbon nanowires, which showed a remarkable discharge capacity of 623 mAh g^{-1} at 1 A g^{-1}.[136] However, the capacity dropped to 56 % only after 100 cycles. Choi at al. enhanced the cycle performance with nearly no capacity loss for 100 cycles by adopting the liquid-phase exfoliated MoS_2 nanosheet and adjusting the potential range to 0.4-2.6 V.[137] Unfortunately, it was sacrificed with capacity (around 110 mAh g^{-1} at 0.8 A g^{-1}). Therefore, maintaining a good cycle performance without sacrificing capacity is highly meaningful but so far remains a challenge. In this work, we made big progress towards this goal by introducing selenium into MoS_2 crystal structure to expand the layer spacing (atomic size of selenium is ~1.2 Å and ~1.05 Å for sulfur) and choosing a proper potential range. The increased lattice spacing can facilitate the intercalation of sodium ions into the layers, which can enhance the electrochemical kinetics and rate performance.

Ex-situ X-ray diffraction (XRD) measurements have been conducted to unveil the sodiation mechanism of MoS_2.[135, 138] Wang et al. investigated the process with ex-situ XRD at three stages.[138] The diffraction peak of Na_2S emerged when the electrode was fully discharged to 0.005 V, and still existed when the electrode was fully re-charged to 2.5 V. In contrast, the peak of MoS_2 fully disappeared and could not recover. Similarly,

Dou et al. have also studied the process with ex-situ XRD and observed the same phenomenon when the electrode was discharged to 0.01 V and re-charged to 2.5 V.[135] These data imply irreversible reaction in the first cycle. Nevertheless, the ex-situ XRD measurements cannot provide accurate information once the 2D nanomaterial becomes amorphous or oxidized during exposure to air ambient. *Herein*, we employed both ex-situ XRD and in-situ Raman measurements to track the sodiation and desodiation processes of our $MoS_{2-x}Se_x$ nanosheet electrode. Raman peaks are very sensitive to composition and phase change, it is especially a useful investigative tool for 2D materials.

To implement the ideas mentioned above, we judiciously designed the electrode by growing $MoS_{2-x}Se_x$ alloy with an ultrathin nanoflake structure on 3D graphene foam backbone. The obtained $MoS_{2-x}Se_x$/GF material is directly used as freestanding anode for SIBs. We have observed higher capacity and rate performance due to selenium substitution induced lattice expansion and pseudocapacitive effect. Furthermore, we also provide strong evidence by in-situ Raman measurement to the intercalation mechanism in a properly selected potential range. Our study provides better understanding and manipulation of the metal ion storage in layered TMD materials.

4.2 Materials preparation

4.2.1 Synthesis of MoS_2/GF

For the synthesis of MoS2/GF, the hydrothermal reaction is conducted. $MoS_{2-x}Se_x$ nanoflake/3D graphene foam ($MoS_{2-x}Se_x$/GF) was prepared with a hydrothermal reaction and a selenization process. A 0.06 g amount of sodium molybdate ($Na_2MoO_4 \cdot 2H_2O$) and 0.12 g of thiourea were dissolved with 30 mL of distilled water at ambient temperature. After the complete dissolution, the mixture was transferred into a Teflon-lined stainless-steel autoclave. A piece of graphene foam substrate (~1 mg cm^{-2}, synthesized by the CVD method) was soaked inside the solution, then the autoclave was kept in an electric oven at 220°C for 12 hours. After cooling to room temperature, the sample was washed with distilled water and ethanol with three times. The obtained sample was dried under vacuum at 70°C for 12 h to achieve the 3D graphene foam supported MoS_2 nanoflake. Then MoS_2/GF was obtained after a calcination in Ar atmosphere for 2 h.

4.2.2 Synthesis of $MoS_{2-x}Se_x$/GF

In terms of the synthesis of $MoS_{2-x}Se_x$ nanoflake/3D graphene foam ($MoS_{2-x}Se_x$/GF), a selenization process has been performed. The $MoS_{2-x}Se_x$/GF was synthesized with a calcination at 700°C for 2h in a mixed Ar-H_2 (2% H_2) atmosphere with addition of selenium powder (0.3 g) placed at the upstream side of the furnace.

4.3 Results and discussion

4.3.1 Materials characterization

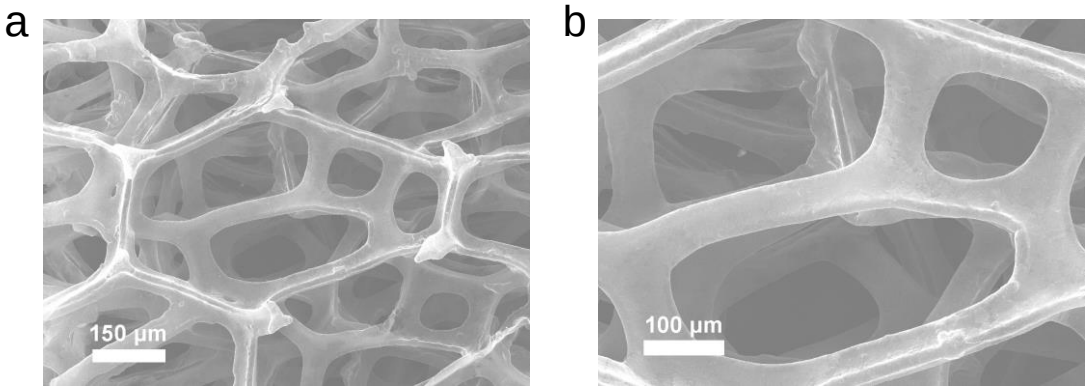

Fig. 4.1 SEM images of graphene foam in low (a) and high (b) resolution.

The pristine graphene foam framework was characterized by SEM with low and high resolution in Figure 4.1. The MoS_2 has a porous and frizzy nanoflake structure (Figure 4.2 a), which can enlarge the electrode surface area and enable efficient ion transport. After the selenium substitution with a suitable concentration, the obtained $MoS_{2-x}Se_x$/GF maintains the uniform nanoflake morphology (Figure 4.2 b and Figure 4.3). The phase and composition are identified with X-ray diffraction (XRD) and Raman spectroscopy measurement. The XRD patterns of both MoS_2/GF and $MoS_{2-x}Se_x$/GF depicted in Figure 4.2 c show the obvious characteristic peaks, which indicates their good crystallinity. In comparison with MoS_2, the corresponding XRD peaks of $MoS_{2-x}Se_x$ shift to lower degree. This reveals that the selenium substitution has enlarged the lattice spacing. For example, the (002) peak of the MoS_2 at 14.55°shifts to 13.6°after the selenization, corresponding to lattice spacing from 6.08 to 6.51 Å due to the larger diameter of selenium atom than sulfur. Larger lattice spacings are favorable in facilitating the intercalation and deintercalation of sodium ions between the interlayers.[139-140] The Raman spectrum of MoS_2/GF (black curve in Figure 4.2 d) shows two characteristic peaks located at 403 and 377 cm^{-1}, corresponding to the A_{1g} (out of plane) and E^1_{2g} (in plane) modes of MoS_2.[141-142] For the $MoS_{2-x}Se_x$/GF sample (red curve), additional Raman peaks due to Mo-Se vibrations appear after the selenization, and meanwhile the peak

intensities of Mo-S vibration modes decrease. The peak located at 287 cm^{-1} attributes to the E^1_{2g} vibration mode of Mo-Se.[95-96, 143] The two peaks at 237.7 and 250.6 cm^{-1} come from the splitting of $MoSe_2$-like A_{1g} mode, which results from the different coordination configuration of Se and S around Mo.[144-145]

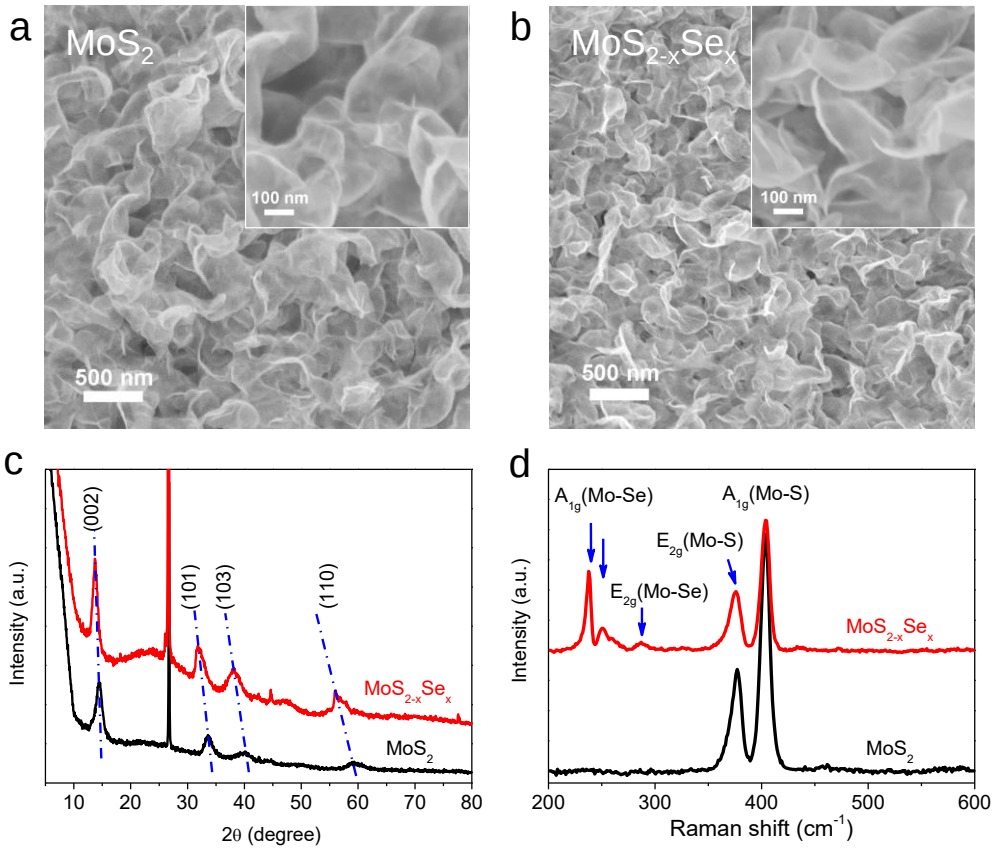

Fig. 4.2 FESEM images of (a) MoS_2/GF and (b) $MoS_{2-x}Se_x$/GF. (c) XRD patterns and (d) Raman spectra of MoS_2/GF and $MoS_{2-x}Se_x$/GF.

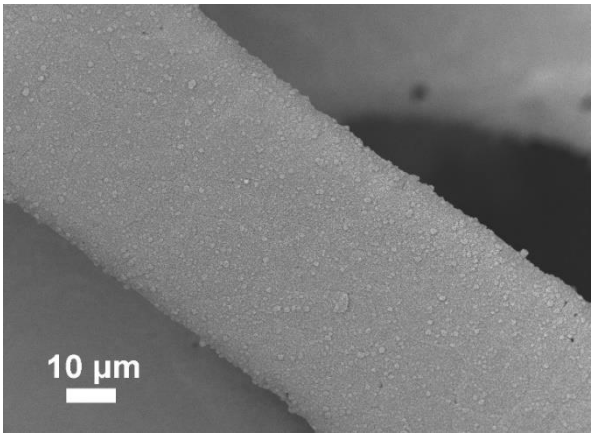

Fig. 4.3 The image of $MoS_{2-x}Se_x$/GF in low magnification.

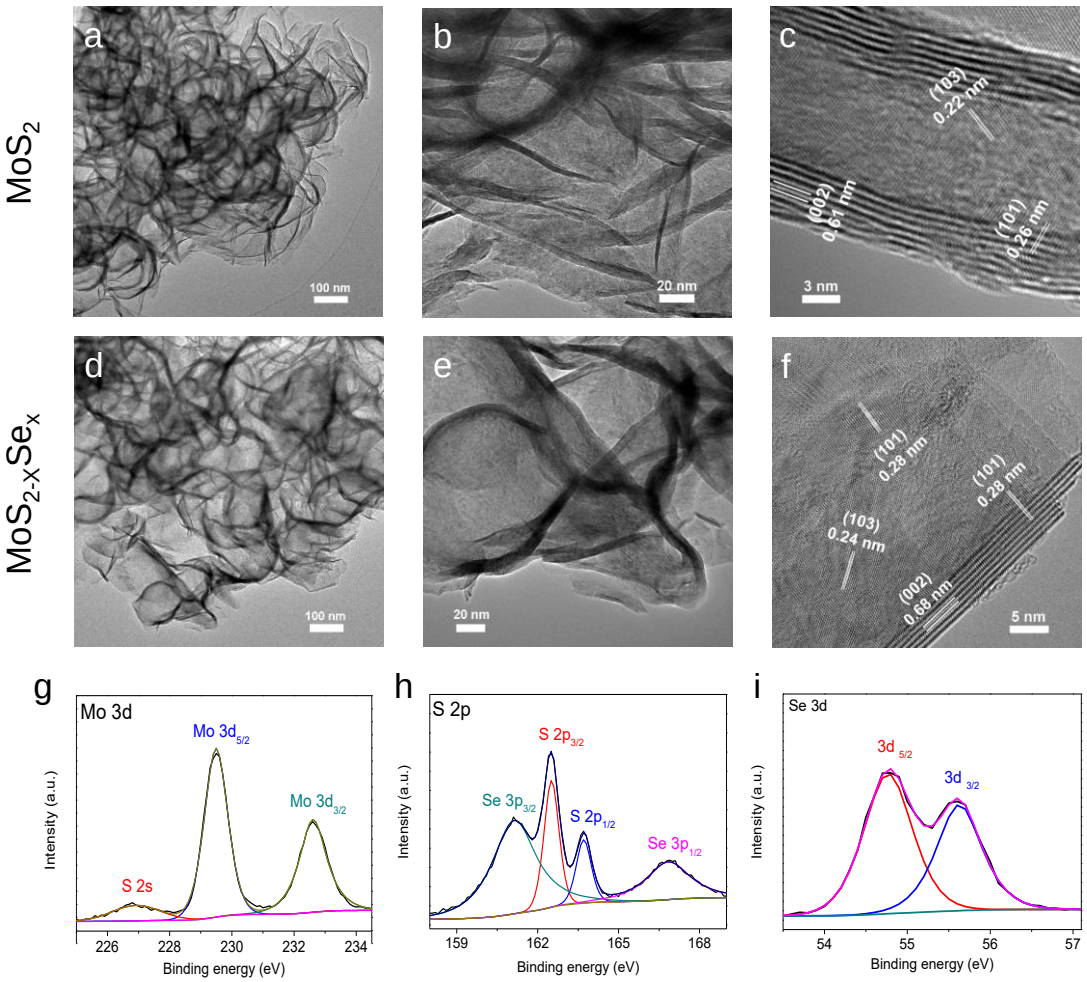

Fig. 4.4 TEM and HRTEM images of (a-c) MoS_2/GF and (d-f) $MoS_{2-x}Se_x$/GF. XPS spectra of $MoS_{2-x}Se_x$/GF: (g) Mo 3d and S 2s, (h) S 2p and Se 3p and (i) Se 3d.

The structures of MoS_2/GF and $MoS_{2-x}Se_x$/GF were further examined by high-resolution transmission electrode microscopy (HRTEM) (Figure 4.4 a-f). Indeed, both samples have similar thin flake structure with a thickness of ~7 nm. The lattice spacings of MoS_2, as identified in Figure 4.4 c, are 0.22, 0.26 and 0.61 nm, corresponding to the (103), (101) and (002) crystal planes. The corresponding lattice spacings of $MoS_{2-x}Se_x$ are 0.24, 0.28 and 0.68 nm (Figure 4.4 f). The expansion of lattice spacings due to selenium substitution is good accordance with the XRD result. X-ray photoelectron spectroscopy (XPS) measurement was used to investigate the surface chemical composition difference on the two samples. The two obvious peaks located at 229.3 and 232.4 eV (Figure 4.4 g) corresponds to Mo $3d_{5/2}$ and Mo $3d_{3/2}$ in the $MoS_{2-x}Se_x$/GF sample, which are very similar with the spectrum in the MoS_2/GF except for small energy shift around 0.5 eV (Figure 4.5 b).[140]

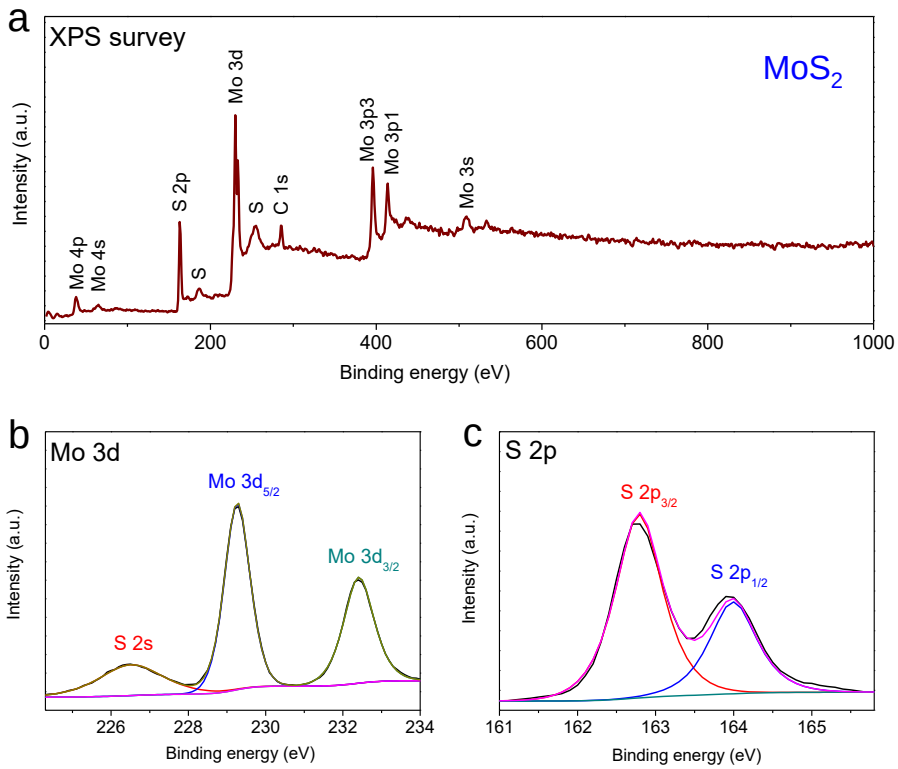

Fig. 4.5 XPS spectra of MoS_2/GF: (a) survey, (b) Mo 3d and (c) S 2p.

Selenium element was detected only in the $MoS_{2-x}Se_x$/GF sample: The peaks at 161.1 and 166.8 eV come from the Se $3p_{3/2}$ and $3p_{1/2}$ (Figure 4.4 h), and the peaks at 54.8 and 55.6 eV come from Se $3d_{5/2}$ and Se $3d_{3/2}$ (Figure 4.4 i). And the Se composition ratio in the $MoS_{2-x}Se_x$/GF sample was determined to be x=0.9 based on the XPS intensity ratios. Furthermore, energy dispersive X-ray spectroscopy (EDX) mapping analysis of $MoS_{2-x}Se_x$/GF (in Figure 4.6 a) also confirms the existence of Mo, S and Se elements and their homogeneous distribution. The S:Se ratio estimated from EDX spectrum is about 14:0.86 in the $MoS_{2-x}Se_x$ (Figure 4.6 b).

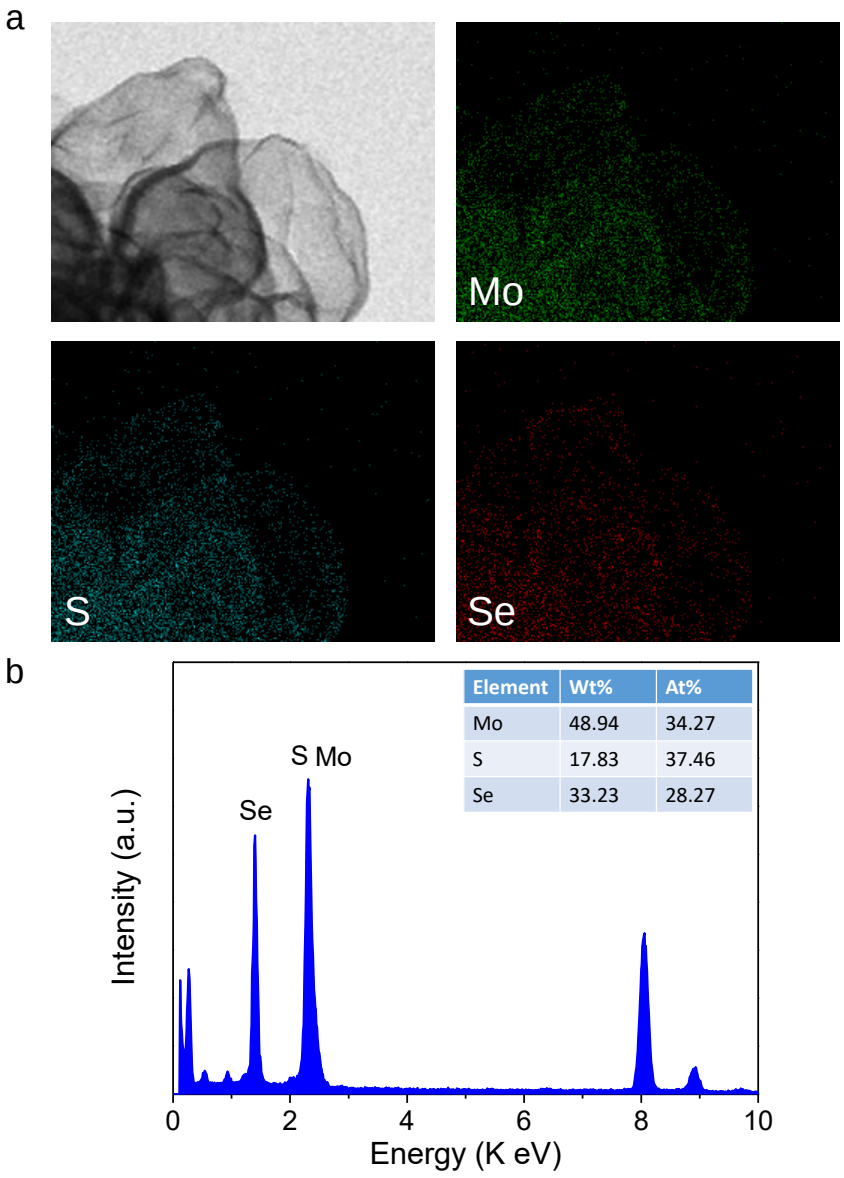

Fig. 4.6 (a) Element mapping images of Mo, S and Se. (b) EDX spectrum of $MoS_{2-x}Se_x$/GF electrode.

4.3.2 Electrochemical analysis

The freestanding MoS_2/GF and $MoS_{2-x}Se_x$/GF were directly used as electrodes to investigate the electrochemical measurements in SIBs. Their typical cyclic voltammetry (CV) curves for initial three cycles in a potential range from 0.5 to 3.0 V (vs. Na^+/Na) with a scan rate of 0.2 mV s^{-1} are illustrated in Figure 4.8 a and b.

They have obvious irreversible capacities in the low voltage range (mainly 0.8-0.5 V) during the first cathodic processes, which result from the formation of solid electrolyte interface (SEI) on the surface of electrode materials, but their reversibility has been enhanced from further cycles. The CV curves of both MoS_2/GF and $MoS_{2-x}Se_x$/GF

(Figure 4.7 a) show multiple redox peaks superimposed with capacitive currents. Especially the quasi-rectangular CV curves within the potential range from 0.5 to 2.4 V indicate the good capacitive-like electrochemical property.[134, 138] Their galvanostatic discharge-charge profiles (Figure 4.7 b) reveal the quasi-linear behavior, which is also indicative to capacitive-model dominating mechanism. In terms of the electrochemical impedance spectroscopy (EIS), as depicted in Figure 4.7 c, the electrochemical reaction impedance in electrode and ion diffusion impedance in electrolyte can be determined by the semicircle in high frequency region and the straight line in low frequency region, respectively. Based on the simulation equivalent circuit (Inset in Figure 4.7 c), the simulated values of Ohmic resistance (R_s) and charge-transfer resistance (R_p) for the $MoS_{2-x}Se_x$/GF electrode are about 4.2 and 420 Ω, respectively, which are lower than those of the MoS_2/GF electrode (5.2 and 585 Ω). It demonstrates the selenium substitution can improve the electrode conductivity.

The MoS_2/GF electrode displays higher first-cycle coulombic efficiency of 60 % than that of $MoS_{2-x}Se_x$/GF electrode with 55 % (Figure 4.7 d). After SEI stabilization, in the next 500 cycles, both them show nearly 100% coulombic efficiency. The third discharge capacities of the two electrodes are 208 and 178 mAh g^{-1}, respectively. Note that the capacities were calculated based on active materials only without adding the mass of graphene foam since our main purpose is to discuss the intrinsic electrochemical property of the material rather than performance of a full battery cell. The specific capacity of GF beyond 0.5 V is about 0.5 mAh g^{-1} at the current density of 0.2 A g^{-1} (see Figure 4.9), their capacity retentions are at about 77 % after 500 cycles.

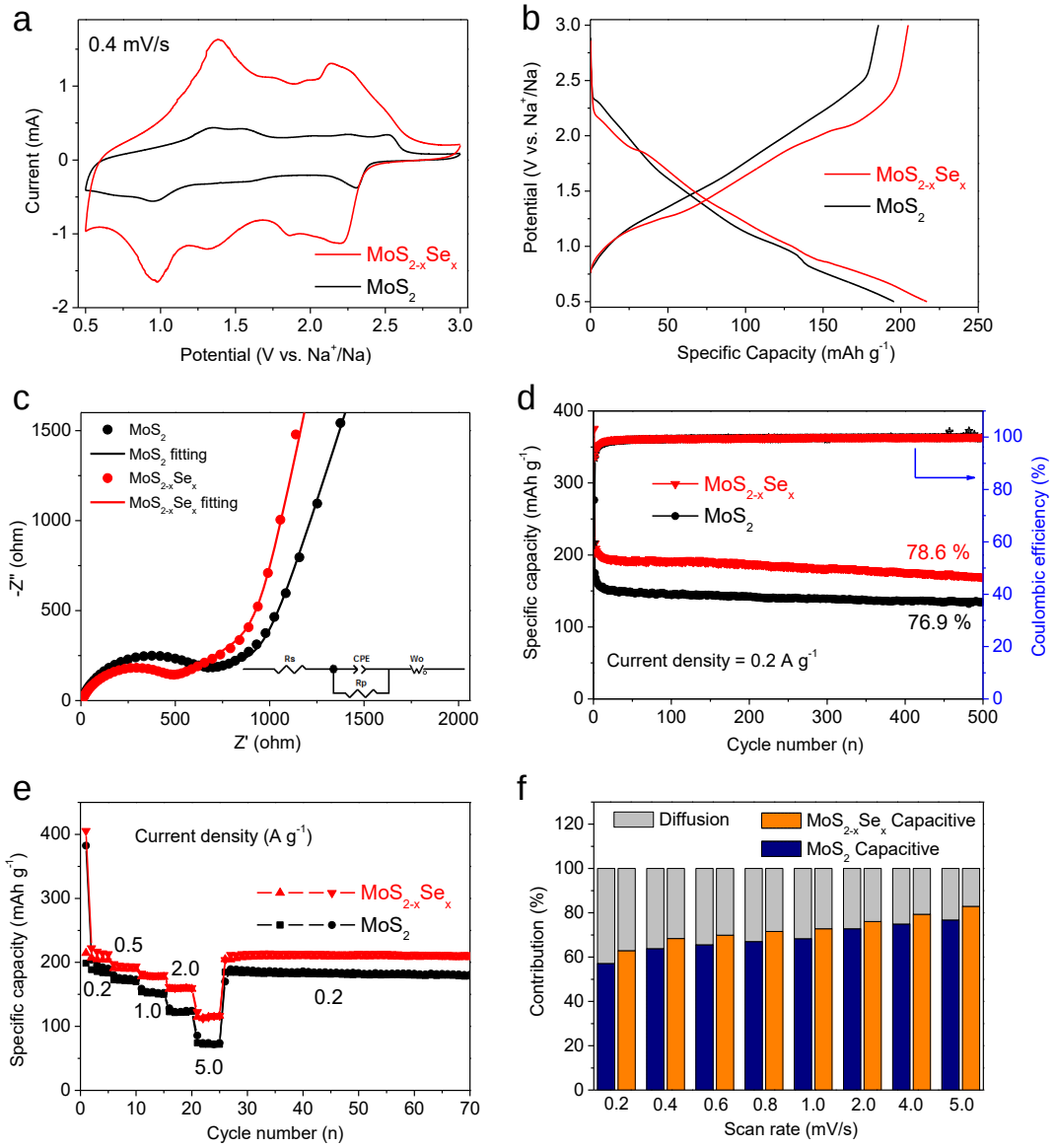

Fig. 4.7 Electrochemical properties of MoS_2/GF and $MoS_{2-x}Se_x$/GF for SIB in the voltage range of 0.5~3.0 V vs. Na^+/Na. (a) Third-cycle CV comparison with a scan rate of 0.4 mV s^{-1}, (b) galvanostatic discharge-charge profiles at a current density of 0.2 A g^{-1} and (c) Nyquist plots at 3.0 V after ten cycles (the resistance is simulated using the same equivalent circuit inserted in the figure). (d) Cycling stability at 0.2 A g^{-1}, (e) rate capability with different current densities and (f) normalized ratios about diffusion and capacitive current contribution.

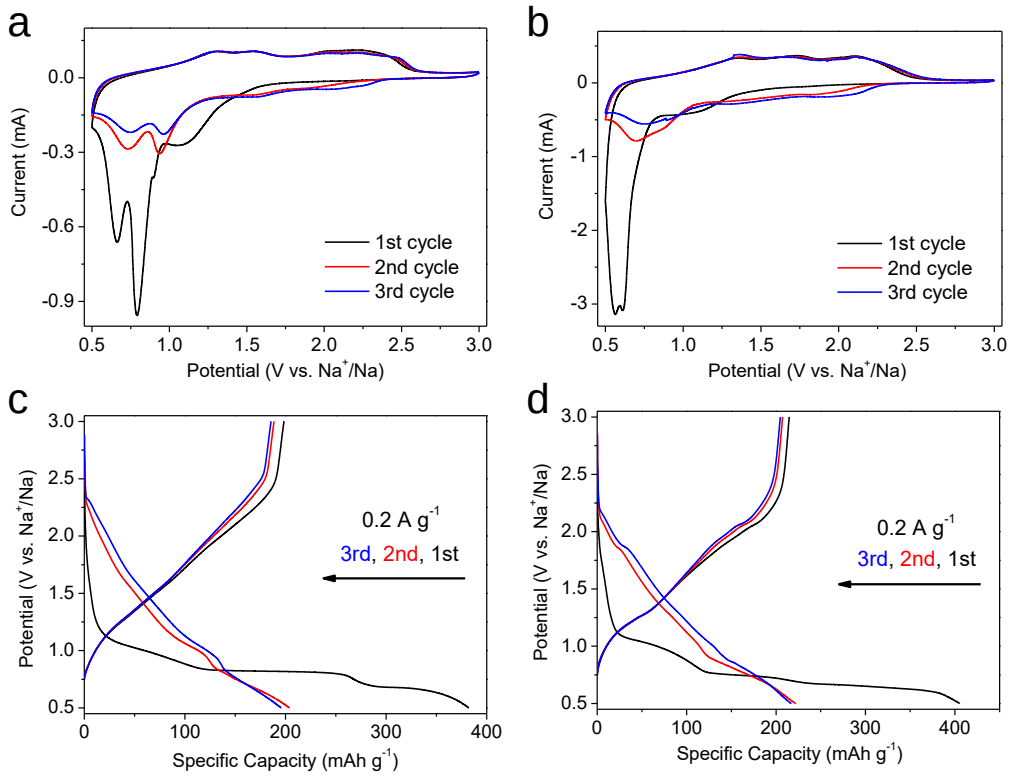

Fig. 4.8 CV curves with a scan rate of 0.2 mV s^{-1} of (a) MoS_2/GF and (b) $MoS_{2-x}Se_x$/GF electrodes and their first three discharge and charge profiles at a current density of 0.2 A g^{-1} in (c) and (d).

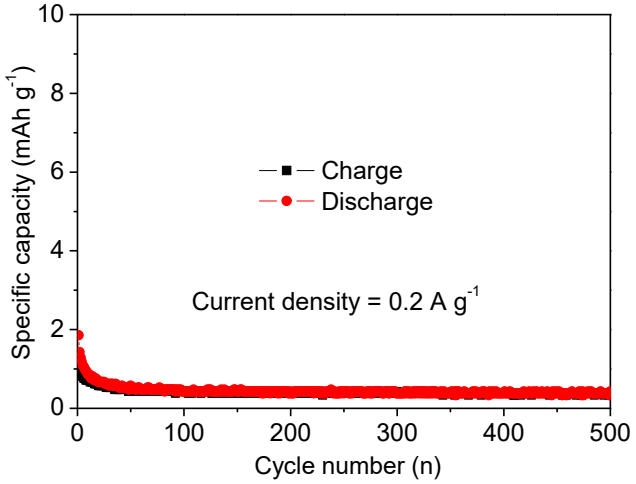

Fig. 4.9 Cycle stability of graphene foam at 0.2 A g^{-1} within the potential range of 0.5-3.0 V.

This significant improvement in capacity retention originates from a properly selected potential range. To compare, we also measured the cycling stability of our $MoS_{2-x}Se_x$/GF electrode in the potential range of 0.01-3.0 V vs. Na^+/Na (see Figure 4.10 a), which exhibits a much poorer cycle performance of about 60 % after 300 cycles.

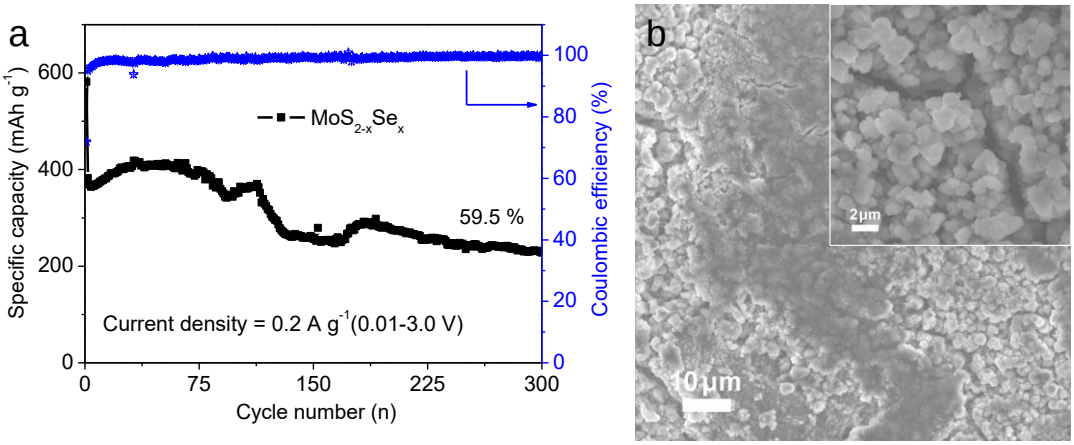

Fig. 4.10 (a) Cycling stability of $MoS_{2-x}Se_x$ at 0.2 A g^{-1} for 300 cycles within the potential range of 0.01-3.0 V vs. Na^+/Na. (b) Morphology of $MoS_{2-x}Se_x$/GF electrode after 300 cycles at 0.2 A g^{-1} with low and high (insert) resolution.

This electrochemical instability is correlated to the change of microscale morphology. The $MoS_{2-x}Se_x$/GF sample tested within the potential range of 0.01-3.0 V after 300 cycles shows severe agglomeration (see SEM images in Figure 4.10 b). In contrast, when cycled in the potential range of 0.5-3.0 V, both MoS_2/GF and $MoS_{2-x}Se_x$/GF electrodes still exhibit the nanoflake structure after 500 cycles with only slight agglomeration on the surface (see Figure 4.11 a and b).

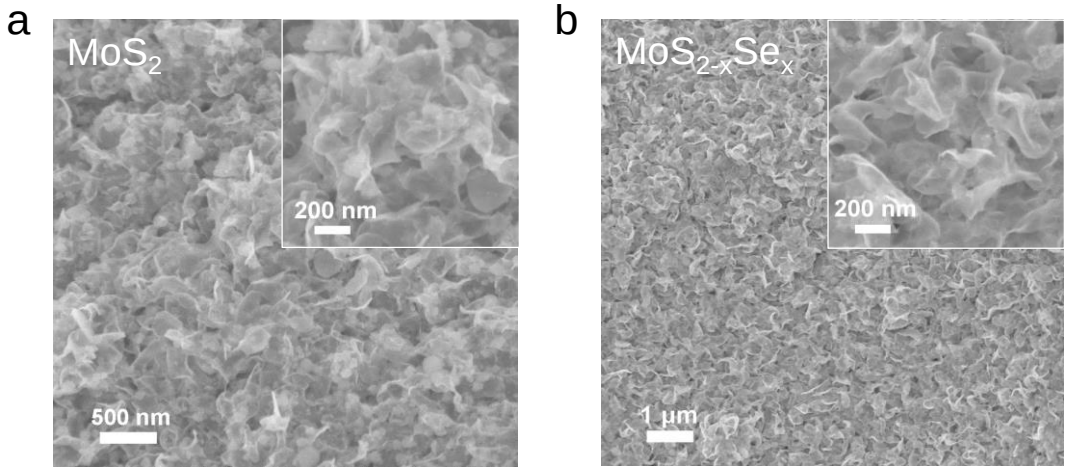

Fig. 4.11 Morphologies of (a) MoS_2/GF and (b) $MoS_{2-x}Se_x$/GF electrodes after 500 cycles at 0.2 A g^{-1} with low and high (insert) resolution.

In addition, both $MoS_{2-x}Se_x$/GF and MoS_2/GF electrodes show good rate performance, but the former has some enhancement (data presented in Figure 4.7 e). The better rate performance results from the expanded lattice spacing after the selenium substitution. After cycling at various current from 0.2 to 5 A g^{-1} and then back to 0.2 A g^{-1}, both electrodes can recover the initial capacities and maintain in the next 50 cycles. The above results demonstrate that adjustment of potential range is an effective approach

to improve electrochemical performance. The comparison on electrochemical properties of $MoS_{2-x}Se_x$/GF in this work and its analogues in half cells are displayed in Table 4.1, which shows the $MoS_{2-x}Se_x$/GF has relatively better cycle performance, but has relatively poor specific capacity, because it has narrow potential window of 0.5-3.0 V vs. Na^+/Na.

Table 4.1 A survey of electrochemical Na-ion storage properties of $MoS_{2-x}Se_x$ and its analogues in half cells (Na metal as counter electrode).

Electrode materials	**Specific capacity (mAh g^{-1}@A g^{-1}) (potential window vs. Na^+/Na)**	**Rate performance (mAh g^{-1}@A g^{-1})**	**Cycle performance (% /cycle@A g^{-1})**
$MoS_{2-x}Se_x$/GF (this work)	222@0.2 (0.5-3.0 V)	120@5	78.6/500@0.2
MoS_2 nanosheet[146]	148@0.012 (0.01-3.0 V)	120@0.12	/
MoS_2/graphene nanoribbon aerogel[147]	372@0.5 (0.01-3.0 V)	203@15	35.1/1,500@5
Sandwich-like graphene@MoS_2@C sheets[148]	480@0.1 (0.01-3.0 V)	320@5	54/200@0.1
MoS_2 nanosheet/C[149]	433@0.2 (0.01-3.0 V)	232@10	/
MoS_2-RGO[150]	305@0.1 (0.01-3.0 V)	214@1	50/50@0.1
MoS_2/electrospun carbon nanofibers (CNFs)[151]	347.5@0.1 (0.01-3.0 V)	147.5@3.2	50.3/50@0.05 66/500@1
MoS_2 Nanosheets/C[152]	447.9@1 (0.01-3.0 V)	306.9@5	60.6/200@1
MoS_2 nanosheet@ N-C nanofiber[153]	510@0.05 (0.01-3.0 V)	355@2	55/100@0.1
MoS_2[154]	372.4@0.5 (0.01-3.0 V)	301.5@5	84/340@1
MoS_2 hollow sphere[155]	391.4@0.1 (0.01-3.0 V)	308@2	28.5/20@2
MoS_2 ultrathin nanosheet[156]	419@0.2 (0.01-3.0 V)	184@4	67.2/50@0.1
MoS_2 nanoflakes @3D carbon[157]	483@0.2 (0.01-3.0 V)	358@5	34.6/200@0.5
MoS_2/cotton-derived carbon fiber[158]	442.7@0.1 (0.01-3.0 V)	355.6@2	58.5/150@0.5
MoS_2@RGO nanosheet[159]	450@0.1 (0.01-3.0 V)	280@2	43.1/160@1
MoS_2/C nanosphere[160]	535@0.1 (0.01-3.0 V)	242@5	15.9/5,000@2
MoS_2-RGO[161]	363.6@0.1 (0.01-3.0 V)	208.6@1	53.4/345@1

Pseudocapacitance enhancement

The better rate performance of $MoS_{2-x}Se_x$/GF draws our attention to understand the kinetics origin. The analyses of redox capacitive contribution of the two electrodes have been adopted to investigate their electrochemical kinetics. The capacitive effect of the electrode at different redox peaks can be qualitatively analyzed from CV curves according to the equation between measured current (i) and scan rate (v): $i=av^b$, where a and b are parameters.[84] When the b value approaches to 1, the electrode kinetics is controlled by capacitive processes; while the b is close to 0.5, the electrode kinetics is diffusion limited (including diffusion on surface, subsurface and bulk lattice). Details of the results for both electrodes are presented in Figure 4.12 and 4.13. Their CV shapes have been well preserved with increasing scan rate from 0.2 to 1.0 mV s^{-1}. The linear dependence ($b \approx 1$) of the current on the sweep rate is determined for both electrodes (Figure 4.12 b and 4.13 b). The $MoS_{2-x}Se_x$/GF electrode shows generally higher b values than those of the MoS_2/GF electrode, which suggests the enhanced capacitive process after the selenium substitution.

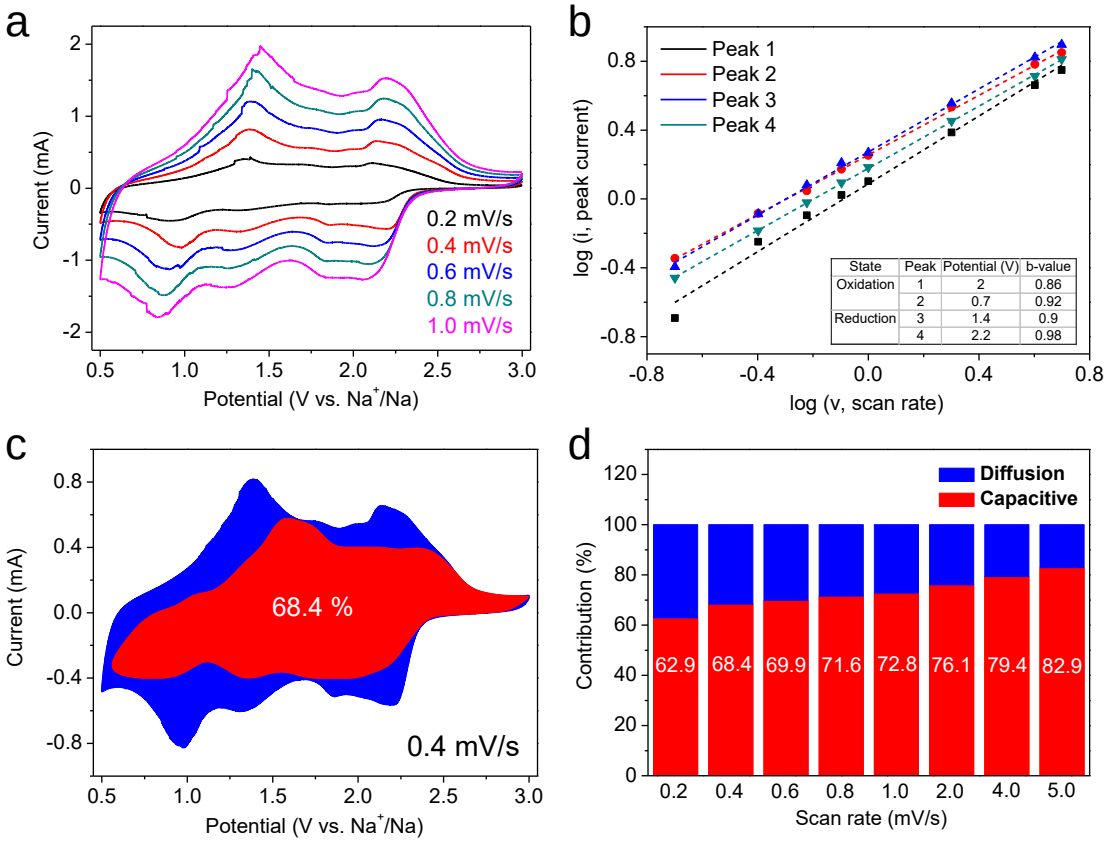

Fig. 4.12 Quantitative analysis of sodium storage behavior of $MoS_{2-x}Se_x$/GF electrode. (a) CV curves at different scan rates. (b) Relationship between logarithm redox peak current and logarithm scan rate. (c) Diffusion current contribution (blue area) and capacitive current contribution (red area) at 0.4 mV s^{-1}. (d) Normalized current contribution ratios of diffusion and capacitive parts at different scan rates.

While the total capacity of nanostructured material generally comes from both diffusion-limited and capacitive currents, we can empirically quantify the contributions of the two processes by conducting the standard CV fitting. To do this, we separate the current response (i) into capacitive-derived and diffusion-derived current at a fixed potential (v).[84] According to the relationship of $i(V)=k_1v+k_2v^{1/2}$, where k_1v is the capacitive part, $k_2v^{1/2}$ is the diffusion-controlled part, v is the scan rate, and k_1 and k_2 are constants. For example, at scan rate of 0.4 mV s^{-1}, the fitting analysis generates the capacitive fraction within the entire potential range of 0.5 ~ 3 V (shaded regions in Figure 4.12 c and 4.13 c), which are calculated to be 63.8 % and 68.4 % in MoS_2/GF and $MoS_{2-x}Se_x$/GF electrodes, respectively. Following this route, capacitive contribution ratios at other different scan rates are determined and presented in Figure 4.12 d and 4.13 d.

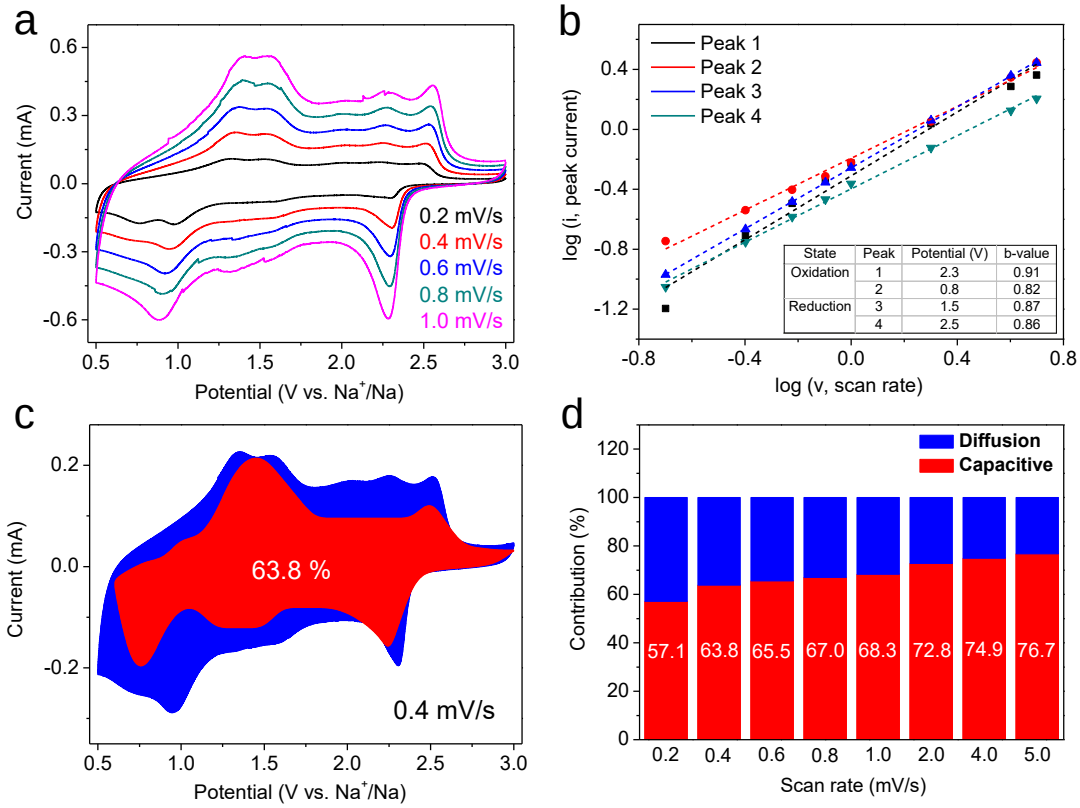

Fig. 4.13 Quantitative analysis of sodium storage behavior of MoS_2/GF electrode. (a) CV curves at different scan rates. (b) Relationship between logarithm redox peak current and logarithm scan rate. (c) Diffusion current contribution (blue area) and capacitive current contribution (red area) at 0.4 mV s^{-1}. (d) Normalized current contribution ratios of diffusion and capacitive parts at different scan rates.

One can see that, as the scan rate increases, the fraction of capacitive contribution enlarges, which is reasonable since the bulk diffusion *vs* capacitive (surface-dominated diffusion) processes depends on the scan rate. By comparing the contribution fractions between the $MoS_{2-x}Se_x$/GF and MoS_2/GF electrodes (see data in Figure 4.7 f), we can see

that former exhibits higher capacitive contribution than the latter at all scan rates. Recalling the above-mentioned rate performance result, we may conclude that the capacitive contribution plays an important role in improving the capacity retention at different discharge currents. And the selenium substitution has enhanced the pseudocapacitance effect by enhancing the lattice spacings.

4.3.3 Investigation of the storage mechanism

In-situ Raman measurement is an effective characterization tool to investigate the composition and crystal structure change during sodiation and desodiation processes. $MoS_{2-x}Se_x$, as one kind of 2D materials, has two types of Raman vibration modes, which can be detected and distinguished easily, so the Raman signal is very sensitive to the $MoS_{2-x}Se_x$. The growth of active material on graphene foam can be used as freestanding electrode to do the measurement without any additive and current collector, which can avoid the influence on Raman signals from additive and current collector. The explosion of active material on graphene foam without any coating layer also provides a good observation to Raman test. The Raman signals of active materials could be distinguished easily. Here, we conducted the in-situ Raman measurement of the $MoS_{2-x}Se_x$/GF electrode during the first sodiation and desodiation processes in two discharge/charge potential ranges: 0.01-3.0 V (Figure 4.14) and 0.5-3.0 V (Figure 4.15).

Therein, the Raman spectrum at open circuit voltage (OCV) of 2.4 V shows the fingerprint peaks of MoS_2 and $MoSe_2$ in the range of 200-500 cm^{-1}. The Raman peaks at 237.8 and 253.3 cm^{-1} come from the peak splitting of $MoSe_2$ A_{1g} vibration mode, and the peak at 287 cm^{-1} corresponds to the $MoSe_2$ E^1_{2g} vibration mode. The peaks located at 377.1 and 405.4 cm^{-1} are attributed to in-plane E^1_{2g} and out-of-plane A_{1g} modes of MoS_2, respectively. Discharging the cell down to 0.8 V results in continuous attenuation of the Mo-Se and Mo-S peaks (Figure 4.14 a), which is due to the increase of intercalated sodium ions. When the discharge potential further goes to 0.6 V, the characteristic Raman peaks become invisible and there is also no emergence of any new peak, suggesting the disappearance of $MoS_{2-x}Se_x$ 2D structure. And there is no emergence of new peak even when the cell was deep discharged to 0.01 V. Afterwards, the cell was charged from 0.01 V onwards until back to 3.0 V (Figure 4.14 b). Surprisingly, the Mo-Se and Mo-S Raman peaks never reappear. This implies that the pristine 2D structure in $MoS_{2-x}Se_x$ has been destroyed after the first discharge to 0.01 V. This is also confirmed by ex-situ XRD

measurement (Figure 4.14 c). Compared to the initial XRD curve, the characteristic peaks of $MoS_{2-x}Se_x$/GF disappear when the electrode is discharged to 0.01 V and re-charge to 3.0 V. The above results jointly confirm that the irreversible loss of the layered structure of $MoS_{2-x}Se_x$ in the first sodiation (discharge) process to 0.01 V.

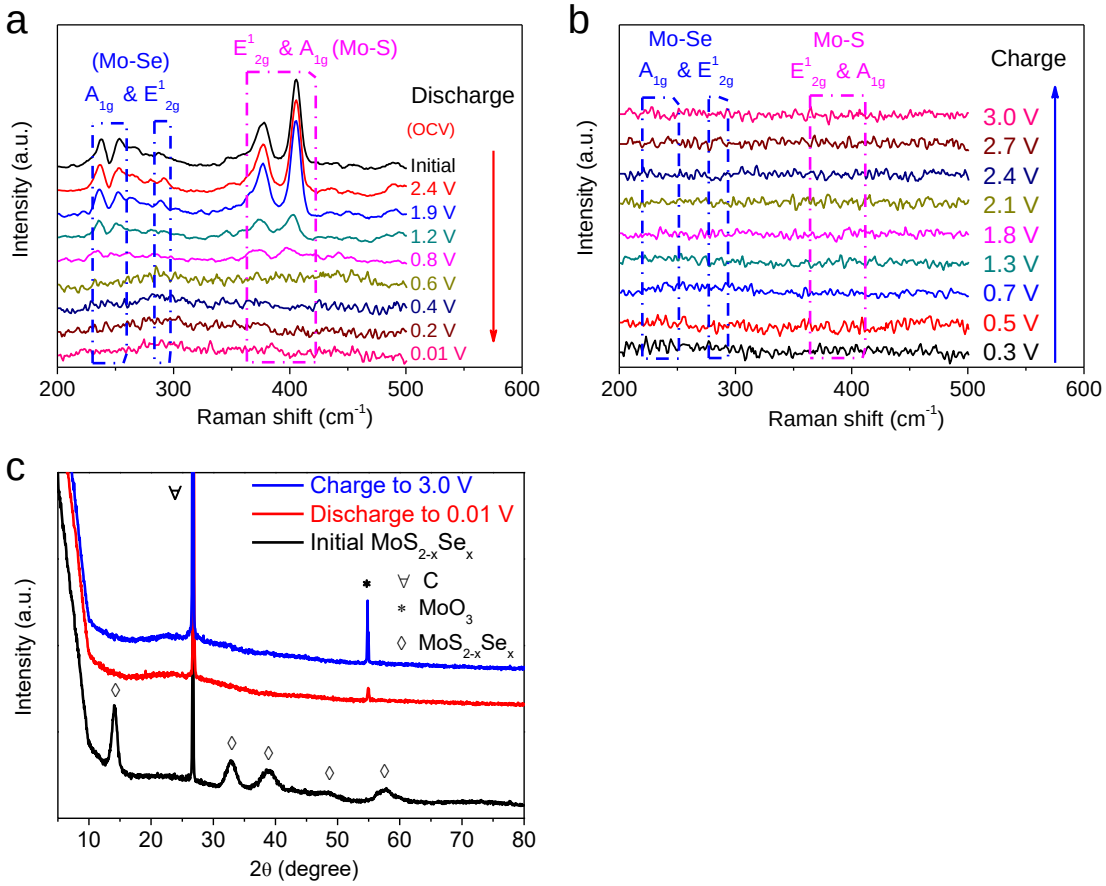

Fig. 4.14 In-situ Raman spectra of the $MoS_{2-x}Se_x$/GF electrode at different cut-off voltages during (a) discharge and (b) charge processes (0.01V-3.0 V) (c) Ex-situ XRD patterns of $MoS_{2-x}Se_x$/GF electrode at different stages.

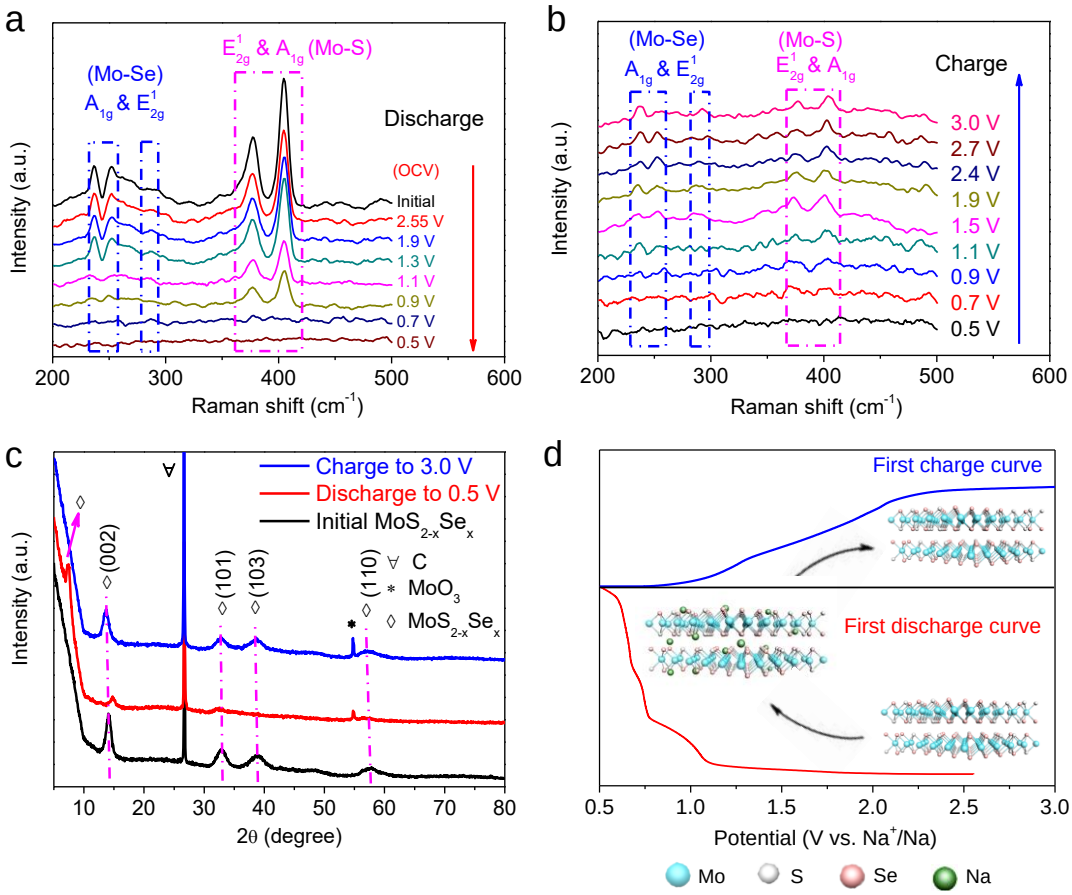

Fig. 4.15 In-situ Raman spectra of the $MoS_{2-x}Se_x$/GF electrode at different cut-off potentials during (a) discharge and (b) charge processes (0.5–3.0 V). (c) Ex-situ XRD patterns at different stages. (d) First sodiation/desodiation processes at different stages.

In contrast, it is found that the 2D structure is reversible in the potential range of 0.5-3.0 V. As shown in Figure 4.15, when first discharged to 0.7 V. The characteristic Raman peaks of Mo-S and Mo-Se become very weak and even unresolvable (Figure 4.15 a). However, in the subsequent charge process (Figure 4.15 b), the fingerprint peaks reappear beyond 0.9 V and grow in intensity with further increase in potential. We also conducted ex-situ XRD measurement at three stages to double confirm the crystal structure (see data in Figure 4.15 c). The new peak at 7.3° emerges when the electrode was discharged to 0.5 V, which results from the expansion of lattice spacing (1.22 nm) after the intercalation of sodium ions. All the characteristic peaks of $MoS_{2-x}Se_x$/GF reappear when the cell is charged back to 3.0 V, implying that the crystal structure is preserved during the full sodiation and desodiation cycle, and that the Na-ion storage occurs via intercalation into the layers rather than the commonly-discussed "decomposition" reaction (Figure 4.15 d).

Based on the in-situ Raman and ex-situ XRD results, we can see that whether or not the 2D layered crystal structure of $MoS_{2-x}Se_x$ (and also MoS_2 and $MoSe_2$) depends on the discharge potential range. When discharged to below 0.5 V, the 2D structure will be destroyed because of decomposition reaction. However, it can be well preserved if the discharge voltage is maintained just above 0.5 V. Therefore, the adjustment of potential range is key to maintaining the 2D structure in $MoS_{2-x}Se_x$ and therefore enhancing the cycle performance (note that most previous reported MoS_2 or $MoSe_2$ 2D electrodes suffer from severe instability). In addition, the selenium substitution enlarges the lattice spacing of the layered structure and improves the conductivity, which accounts for the enhanced rate performance.

4.4 Conclusion

In this work, thin $MoS_{2-x}Se_x$ nanoflakes grown quasi-vertically on 3D GF have been employed as freestanding and flexible electrode for Na ion storage. The $MoS_{2-x}Se_x$/GF electrode with a Se concentration (x=0.9) exhibits enhanced rate performance with a higher reversible capacity and capacity retention compared to pure nanoflake MoS_2/GF electrodes. Quantitative analysis reveals that the improved pseudocapacitive contribution, derived from enlarged interlayer spacing by selenium substitution, is the origin of good rate performance. The in-situ Raman together with ex-situ XRD measurements further reveals that the 2D structure in $MoS_{2-x}Se_x$ can be preserved due to Na-ion intercalation process in the potential range above 0.5 V. Discharge to 0.01 V leads to damage of the 2D structure and aggregation. The insight of this experiment may be extended to other layered 2D materials in fast-rate metal ion storage.

Chapter 5 Zn ions storage in layered lepidocrocite-VOOH

Rechargeable aqueous zinc-ion battery (AZIB), as a novel promising candidate to grid-scale energy storage system, has drawn tremendous attention recently. The electrochemical properties and storage mechanisms of various vanadium-based materials have been investigated in AZIBs. However, these reported vanadium-based cathode materials usually possess the high valence states of vanadium (such as V^{4+} and V^{5+}), the vanadium-based cathode materials with low valence states have scarcely been discussed yet. Herein, the lepidocrocite-VOOH with a low valence state (V^{3+}) has been introduced in this work, which was synthesized with a self-sacrificial template induced method. Its electrochemical properties and reaction kinetics are investigated in detail. And composition changes and crystal structure evolution are also characterized by synchrotron-based in-situ X-ray diffraction (XRD). Moreover, the combined density functional theory (DFT) calculation provides a new storage mechanism of zinc ions in vanadium-based materials.

5.1 Introduction and motivation

The extensive development of portable electronics and renewable energy technologies facilitates researches on energy storage techniques. Rechargeable lithium-ion battery (LIB), as an effective electrochemical energy storage system, has a great improvement in these three decades, which also inspires the studies of other alkali metal ion batteries, such as sodium-ion batteries (SIBs) and potassium-ion batteries (KIBs), because they have similar electrochemical mechanisms and behaviors within organic electrolytes.[1, 162] However, LIBs cannot meet the severe requirement for large scale energy storage due to the high cost of raw resource. And there are still some safety issues with the conventionally flammable electrolytes.[46] Multivalent metal-ion batteries using earth abundant elements (such as Zn, Al, Mg and Ca) have drawn tremendous attention as potential alternatives for alkali metal-ion batteries. Among them, AZIB has been revived recently because of the development of electrochemical principles, the advantages of low cost and earth-abundant materials, highly stable zinc element and high safety of aqueous electrolyte.[163] And the zinc anode has a relatively high theoretical

capacity (820 mAh g^{-1}) and a low redox potential (-0.76 V vs. standard hydrogen electrode). These merits of AZIB indicate its great application potential to large scale energy storage systems.[25-26, 28-29, 164-165]

Zinc foil can be directly served as anode in AZIB, which is simple and cheap enough, so most researchers focus on the cathode materials. Many kinds of zinc salts, such as conventional $ZnSO_4$ and $Zn(CF_3SO_3)_2$, can be used as solutes in aqueous electrolytes with different concentrations, which possess high ion diffusivities and low toxicity. These strengths can meet the requirements of economical, environment-friendly and massive-scale energy storage systems.[28, 165] Vanadium-, manganese- and Prussian Blue-based materials are the main cathode materials for AZIBs, their main electrochemical potentials are in the range of 0.2 to 2.0 V vs. Zn^{2+}/Zn. As for vanadium-based materials, many kinds of them with high valence states (such as V^{5+} and V^{4+}) have been investigated within different types of electrolytes, and their storage mechanisms have also been studied with various characterization techniques.[25, 28-29, 164-165] However, the vanadium-based materials with low valence states (such as V^{2+} and V^{3+}) have scarcely been reported yet. Some of them have suitable crystal structures to accommodate zinc ions inside. Moreover, common ex-situ measurements are not precise to detect the cyclic process because of the severe influence in the ambient environment. Thus, in-situ XRD technique is introduced in this work to reveal the zinc ion storage process.

Lepidocrocite-VOOH has a low valence state (V^{3+}) and the layered crystal structure with a lattice spacing of 6.255 Å in (020) crystal plane, which is much larger than the diameter of Zn^{2+} (0.75 Å). This implies the suitable crystal structure to store zinc ions inside. Herein, the lepidocrocite-VOOH nanobelt was synthesized with two-step hydrothermal reactions and served as cathode material to investigate its electrochemical properties with 2M $Zn(CF_3SO_3)_2$ electrolyte. The VOOH exhibits relatively good electrochemical performance within the potential range from 0.2 to 1.6 V vs Zn^{2+}/Zn. The electrochemical reaction kinetics is also investigated with galvanostatic intermittent titration technique (GITT) and redox capacity contribution analysis. Furthermore, the composition changes and crystal structure evolution are characterized with synchrotron-based in-situ XRD. Combined with DFT calculation, a new storage mechanism of zinc ions in vanadium-based materials has been proposed. This work provides an insight into the study of cathode materials in AZIBs.

5.2 Materials preparation and theoretical calculation

Lepidocrocite-VOOH nanobelt was synthesized with a self-sacrificial template induced method, which contains two step hydrothermal reactions.

5.2.1 Synthesis of $H_2V_3O_8$ precursor

First, the precursor of $H_2V_3O_8$ nanowire was prepared with a hydrothermal reaction. The 1 m mol $VO(ACAC)_2$ was dissolved in a 45 ml Teflon-lion stainless steel autoclave with 37 mL of distilled water at the ambient environment. And then 1.5 mL of 1M HNO_3 solution was added into the solution dropwise with a stir for 15 minutes. After the stirring, the autoclave was kept in an electric oven at 180 ℃ for 12 hours. After cooling to room temperature, the sample was collected by washing with distilled water and ethanol for three times. The $H_2V_3O_8$ nanowires were achieved by drying under vacuum at 60 ℃ for 12 hours.

5.2.2 Synthesis of VOOH nanobelt

The obtained $H_2V_3O_8$ nanowire was used as a precursor to fabricate lepidocrocite-VOOH nanobelt with another hydrothermal reaction. 94 mg of $H_2V_3O_8$ precursor was dissolved into an autoclave with 37 mL of distilled water under a stirring for 15 minutes, and then 0.6 mL of $N_2H_4{\cdot}H_2O$ was added into the solution dropwise with a stirring for 30 minutes. The autoclave was put into an electric oven with 180 ℃ for 12 hours. After cooling to the ambient temperature, the lepidocrocite-VOOH nanobelt was collected by washing with distilled water and ethanol for three times and drying under Ar gas at 60 ℃ for 12 hours.

5.2.3 Density functional theory (DFT) calculation

The CASTEP (Cambridge Serial Total Energy Package) program was utilized to calculate the bond parameters of lepidocrocite-VOOH unit cells before and after the combination with Zn ions, which is based on the density functional theory and plane-wave pseudopotential method. And the Perdew-Burke-Ernzerhof (PBE) function was applied to obtain the exchange-correlation potential in the generalized gradient approximation (GGA). Norm-conserving pseudopotentials were used for the description of electron-ion interactions. The cut-off energy of 520 eV was used for the expansion of plane waves. Tolerance for the self-consistence was employed at: 2×10^{-5} eV per atom for total energy, 0.05 eV $Å^{-1}$ for force, 0.1 GPa for maximum stress and 0.002 Å for the

maximum displacement. G-point sampling of 3 × 4 × 1 k-point was used for integration of Brillouin zone. The dimensions of unit cell were 3.873 Å × 3.072 Å × 12.516 Å. Periodic boundary conditions were employed in all three directions.

5.3 Results and discussion

5.3.1 Materials characterization

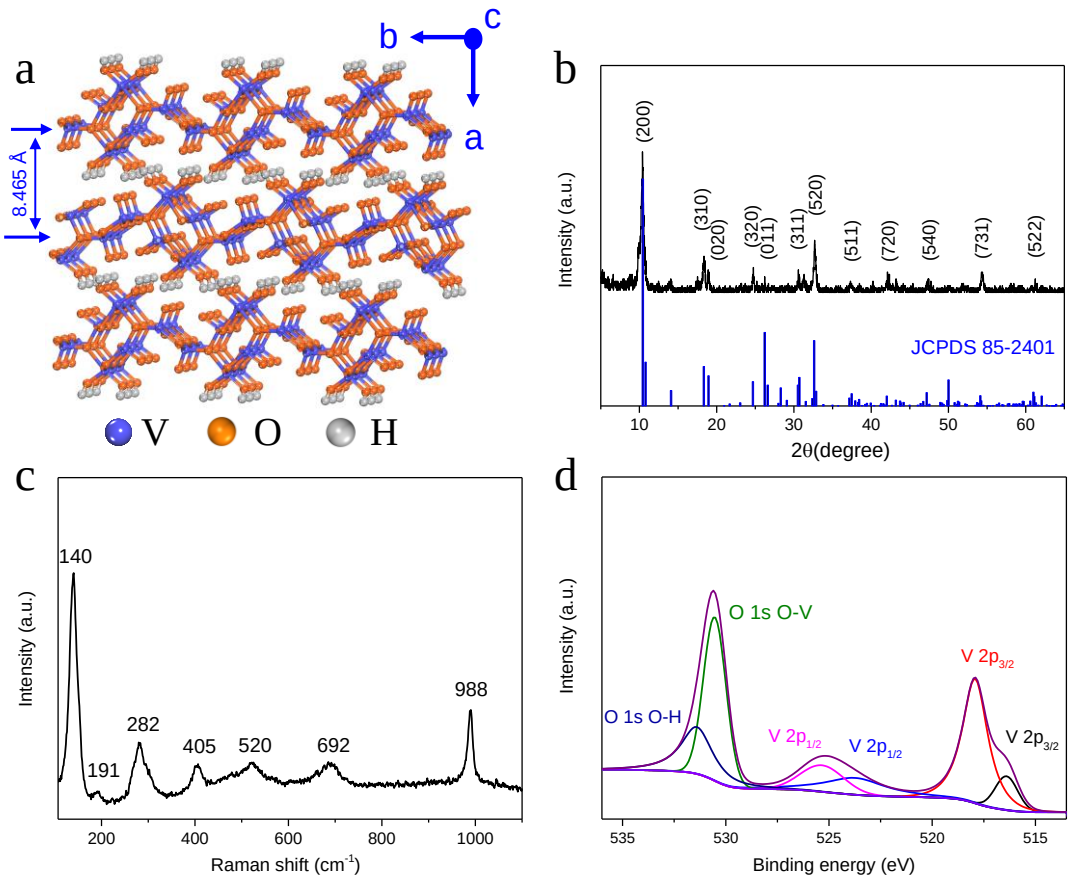

Fig. 5.1 (a) Schematic crystal structure, (b) XRD pattern, (c) Raman spectrum and (d) XPS spectra of $H_2V_3O_8$.

The precursor of $H_2V_3O_8$ nanowire was synthesized with hydrothermal reaction, which endows a layered structure (in Figure 5.1a). The phase and composition of $H_2V_3O_8$ are identified with XRD and Raman spectroscopy measurements. The XRD pattern in Figure 5.1b shows the obvious characteristic peaks, which are in good agreement with the trivanadium pentaoxide hydrate (JCPDS: 85-2401).[166-168] As for the Raman spectrum in Figure 5.1c, the absorption bonds at 140 and 191 cm^{-1} result from the stretching mode of $(V_2O_2)n$, indicating the layered structure.[169] The fingerprint peaks located at 282 and 405 cm^{-1} are attributed to the bending vibration mode of V-O. The peaks of 520 and 692 cm^{-1} come from the stretching vibration of V-O, and the peak at 988 cm^{-1} is indexed to

the stretching mode of V=O.[167, 170] The valence states of $H_2V_3O_8$ are further characterized by X-ray photoelectron spectroscopy (XPS). As shown in Figure 5.1d, the valence states of vanadium can be classified into representative V $2p_{3/2}$ and V $2p_{1/2}$ orbitals. The two peaks of V $2p_{3/2}$ can be identified into V^{4+} (516.4 eV) and V^{5+} (517.9 eV), respectively. Meanwhile, the spectrum of V $2p_{1/2}$ can be divided into 523.7 and 525.3 eV, which attribute to V^{4+} and V^{5+}. The XPS peaks of O 1s at 530.5 and 531.4 eV belong to the bonds of O-V and O-H.[168, 171-173] And energy dispersive X-ray spectroscopy (EDX) mapping analysis of $H_2V_3O_8$ (in Figure 5.2a-c) also confirms the existence of V and O elements and their homogeneous distribution.

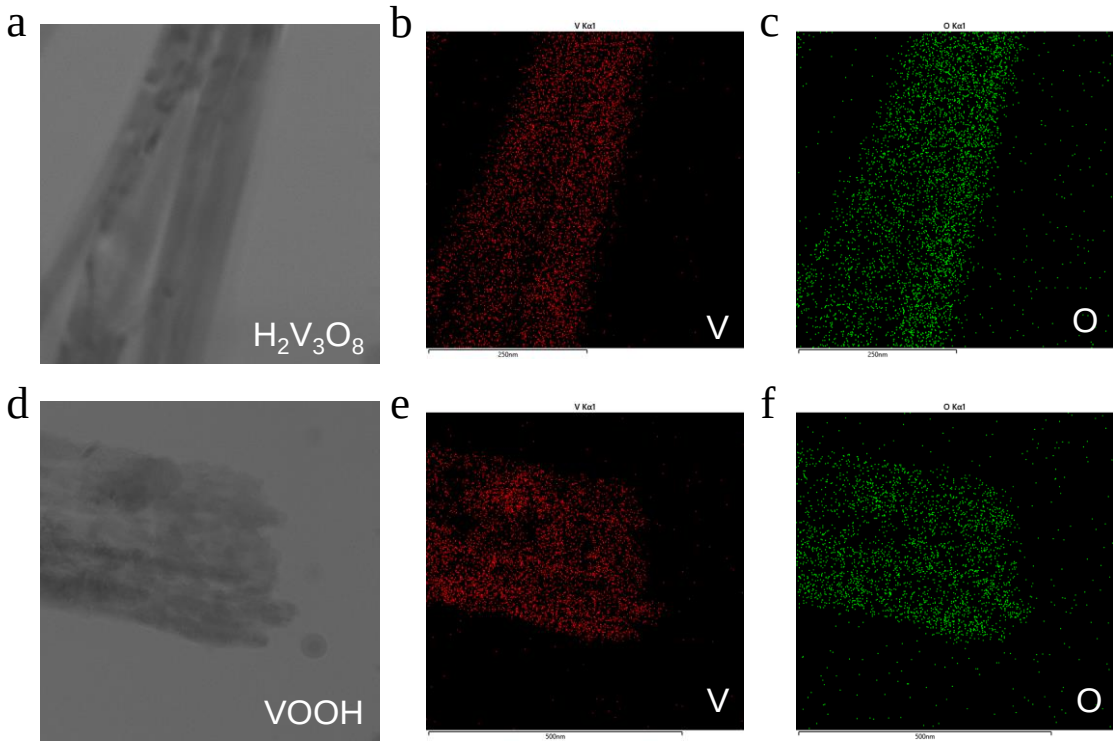

Fig. 5.2 Element mapping images of V and O in (a-c) $H_2V_3O_8$ and (d-f) VOOH.

The morphology of the precursor $H_2V_3O_8$ was observed by field-emission scanning electron microscopy (FESEM) and high-resolution transmission electron microscopy (HRTEM). The images in Figure 5.3a-c exhibit the nanowire morphology, which possess a size of about 200 nm in width and hundreds of micrometers in length. The lattice-resolved image of $H_2V_3O_8$ nanowire presented in Figure 5.3d was obtained from HRTEM. The characteristic lattice spacings of 0.353 and 0.485 nm correspond to the (011) and (020) crystal planes with an angle of 68.9°.[166-168] Moreover, the selected area electron diffraction (SAED) pattern, illustrated in the inset of Figure 5.3d, identifies the (020) and

(011) crystal planes, which demonstrate the intrinsic single-crystal structure of orthorhombic $H_2V_3O_8$.

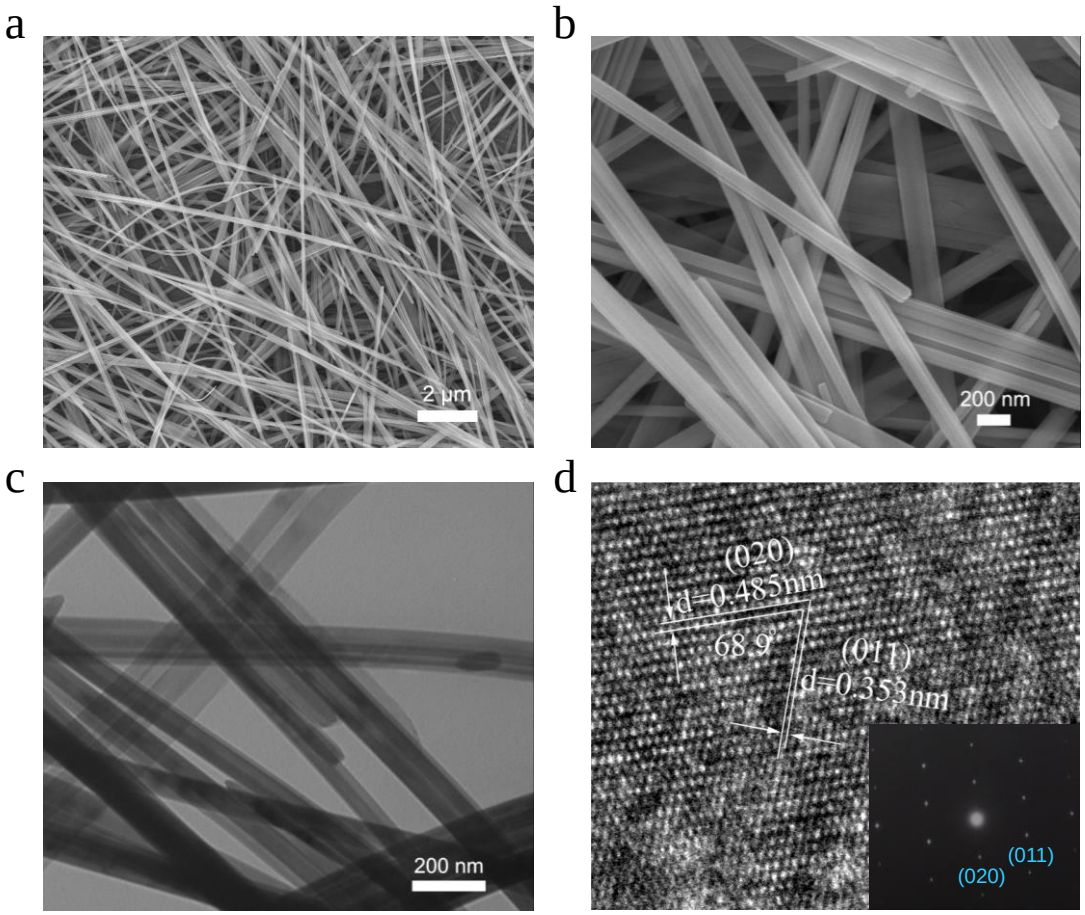

Fig. 5.3 (a and b) SEM and (c and d) HRTEM images with the SEAD pattern (inset in d) of $H_2V_3O_8$.

The lepidocrocite-VOOH nanobelt was obtained via a further hydrothermal reaction with $H_2V_3O_8$ nanowire precursor based on the self-sacrificial template induced synthesis. The inner crystal structure is presented in Figure 5.4a. The phase and composition of VOOH nanobelt were identified by XRD measurement. The obviously characteristic peaks of VOOH, as shown in Figure 5.4b, indicate the high crystallinity of the sample. According to the similarity of crystal structures between γ-FeOOH (JCPDS: 74-1877) and VOOH, the sample can be well indexed to the lepidocrocite-phase VOOH.[174-175] The phases of VOOH were further identified by Raman spectroscopy in Figure 5.4c. The peaks located at 139 and 191 cm^{-1} indicate the layered structure inside.[169] The peaks of 281 and 406 cm^{-1} come from the bending vibration of V-O, and the stretching vibration results in the Raman peak at 694cm^{-1}. The 990 cm^{-1} identifies the stretching vibration mode of V=O inside the VOOH.[174, 176] Furthermore, XPS is an effective technique to reveal the valence states of VOOH. As shown in Figure 5.4d, the vanadium peaks located

at 516.3 and 523.9 eV are attributed to V $2p_{3/2}$ and V $2p_{1/2}$, respectively, which are in good agreement with the reported valence state of V^{3+}. And the O 1s peaks at 530.5 and 531.5 eV, coming from O-V and O-H bonds, are also identified.[177-178] And EDX mapping analysis of VOOH, shown in Figure S2d-f, indicates the homogeneous distribution of V and O elements inside.

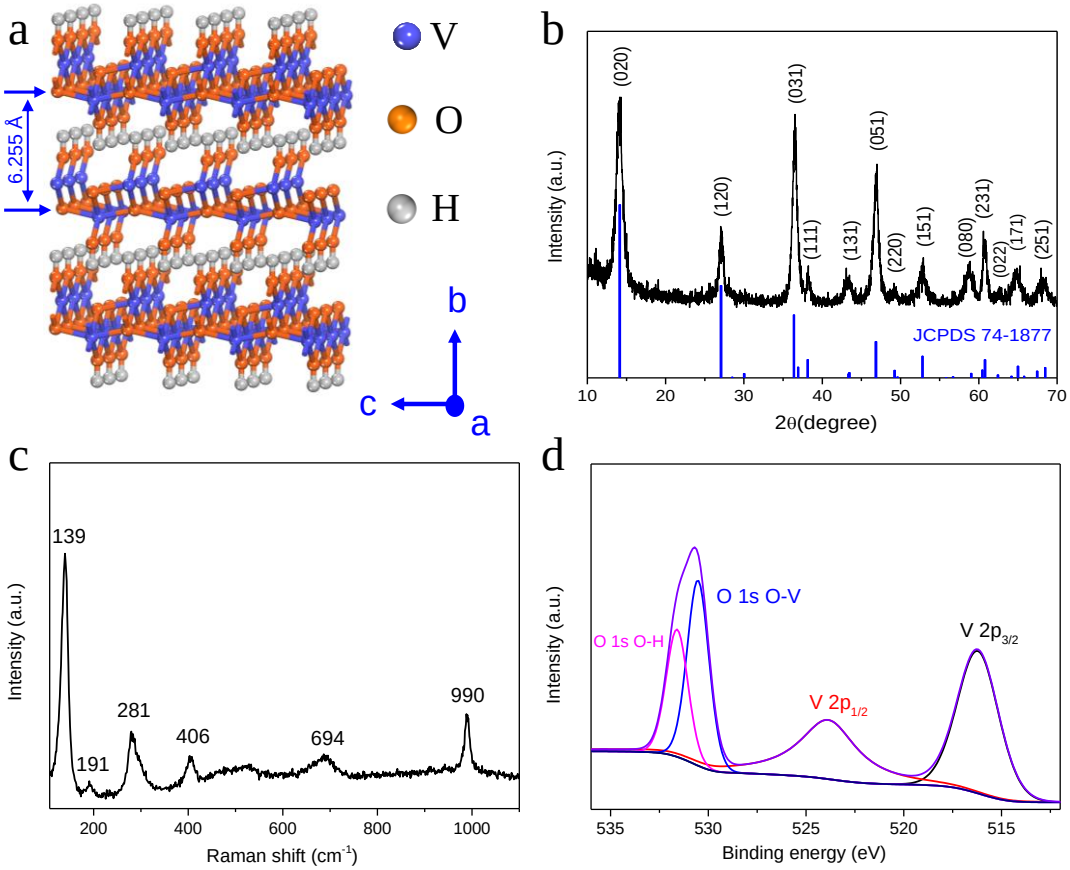

Fig. 5.4 (a) Schematic crystal structure, (b) XRD pattern, (c) Raman spectrum and (d) XPS spectra of the synthesized lepidocrocite-VOOH nanobelts.

The morphology of VOOH is also investigated by FESEM and HRTEM in Figure 5.5. VOOH nanobelt possesses a size of 3-5 μm in length and ~100 nm in width (Figure 5.5a-c). And the short length and rough surface of VOOH nanobelt could be speculated from the synthesis method of self-sacrificial template based on $H_2V_3O_8$ nanowires. The fine-lattice structure of VOOH is presented in Figure 5.5d. Two representative lattice spacings of 0.656 and 0.349 nm with an angle of 64.2° can be identified to the crystal planes of (020) and (120), respectively.[174-175, 179] And SEAD pattern (inset in Figure 5.5d) also demonstrates the high crystallinity of lepidocrocite-phase VOOH.

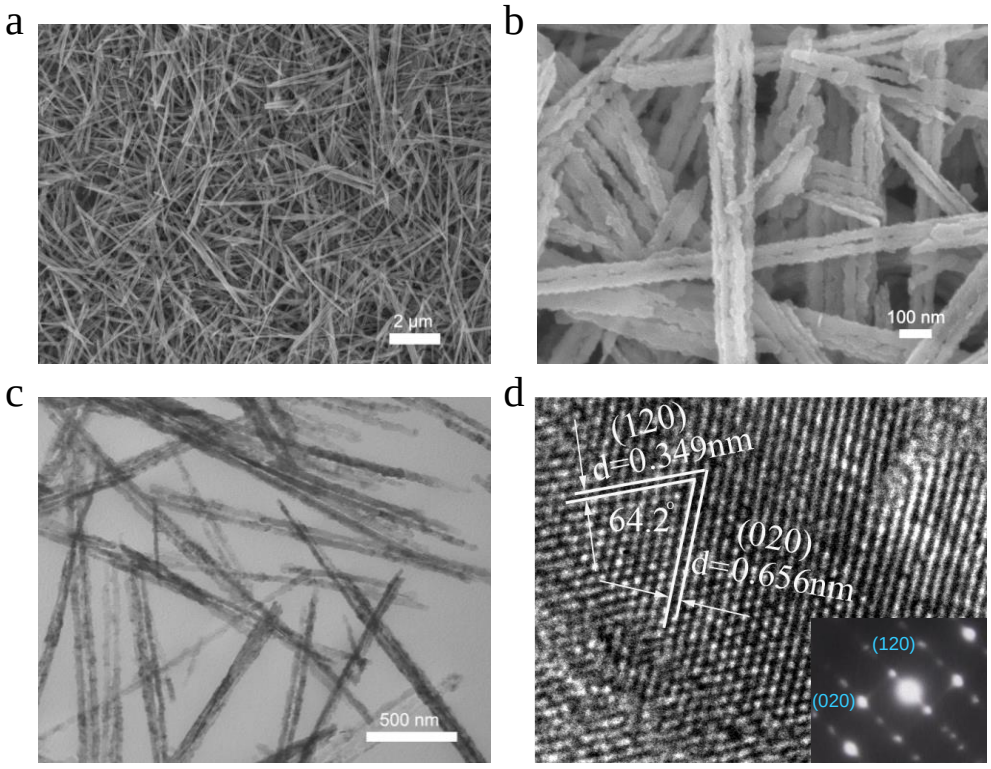

Fig. 5.5 (a and b) SEM and (c and d) HRTEM images with the SEAD pattern (inset in d) of lepidocrocite-VOOH nanobelts.

5.3.2 Electrochemical analysis

Electrochemical properties

The $H_2V_3O_8$ and VOOH were used as working electrode materials to investigate their electrochemical properties in AZIB. As for VOOH, its typical cyclic voltammetry (CV) curves for initial three cycles within the potential range from 0.2 to 1.6 V vs. Zn^{2+}/Zn under a scan rate of 0.2 mV s^{-1} are presented in Figure 5.6a. Two pairs of redox peaks with good reversibility are illustrated in further two cycles. The pristine three CV curves of $H_2V_3O_8$ at a scan rate of 0.2 mV s^{-1} are shown in Figure 5.7a, which have good reversibility and several pairs of redox peaks. The galvanostatic charge and discharge (GCD) profiles of VOOH (Figure 5.6b) with a current density of 0.5 A g^{-1} reveal a low Coulombic efficiency in the first cycle. The next two GCD profiles exhibit good reversibility. And the GCD curves of $H_2V_3O_8$ with a current density of 0.5 A g^{-1} are presented in Figure 5.7b, which exhibit similar curves in the first three cycles. This demonstrates the good reversibility of $H_2V_3O_8$ in AZIB.

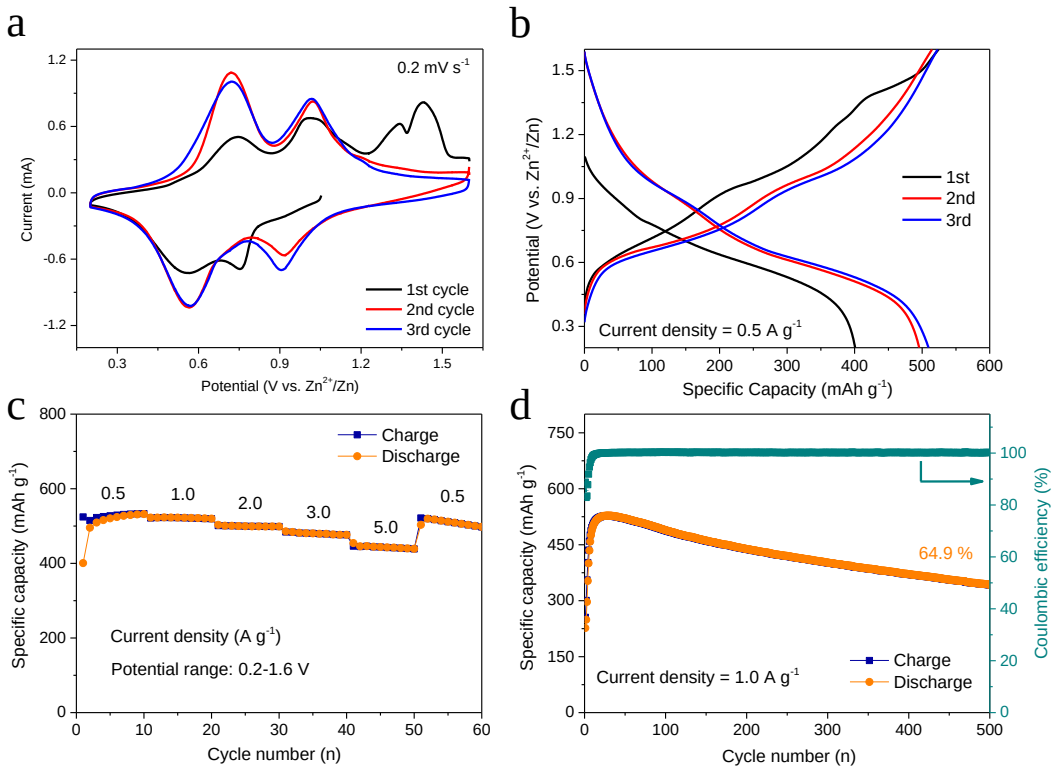

Fig. 5.6 Electrochemical properties of lepidocrocite-VOOH within the potential range from 0.2 to 1.6 V vs. Zn^{2+}/Zn. (a) The initial three CV curves with a scan rate of 0.2 mV s^{-1}; (b) galvanostatic charge-discharge profiles at a current density of 0.5 A g^{-1}; (c) rate capability with different current densities and (d) cyclic stability and Coulombic efficiency at a current density of 1.0 A g^{-1}.

The energy storage properties of $H_2V_3O_8$ and VOOH were studied with rate and cycle measurements at different current densities within the potential range of 0.2-1.6 V vs. Zn^{2+}/Zn. In terms of the rate performance of $H_2V_3O_8$, it exhibits the discharge specific capacities of ~280 and 195 mAh g^{-1} at the current densities of 0.5 and 5.0 A g^{-1} (Figure 5.7c), respectively. The specific capacity recovers to ~290 mAh g^{-1} once the rate returns to 0.5 A g^{-1}. VOOH delivers specific capacities of ~525 and 440 mAh g^{-1} at rates of 0.5 and 5.0 A g^{-1} in Figure 5.6c, respectively. The capacitance recovers to ~510 mAh g^{-1} when the current density returns to 0.5 A g^{-1}. VOOH displays relatively higher specific capacity than most of vanadium-based cathode materials in Table 5.1.

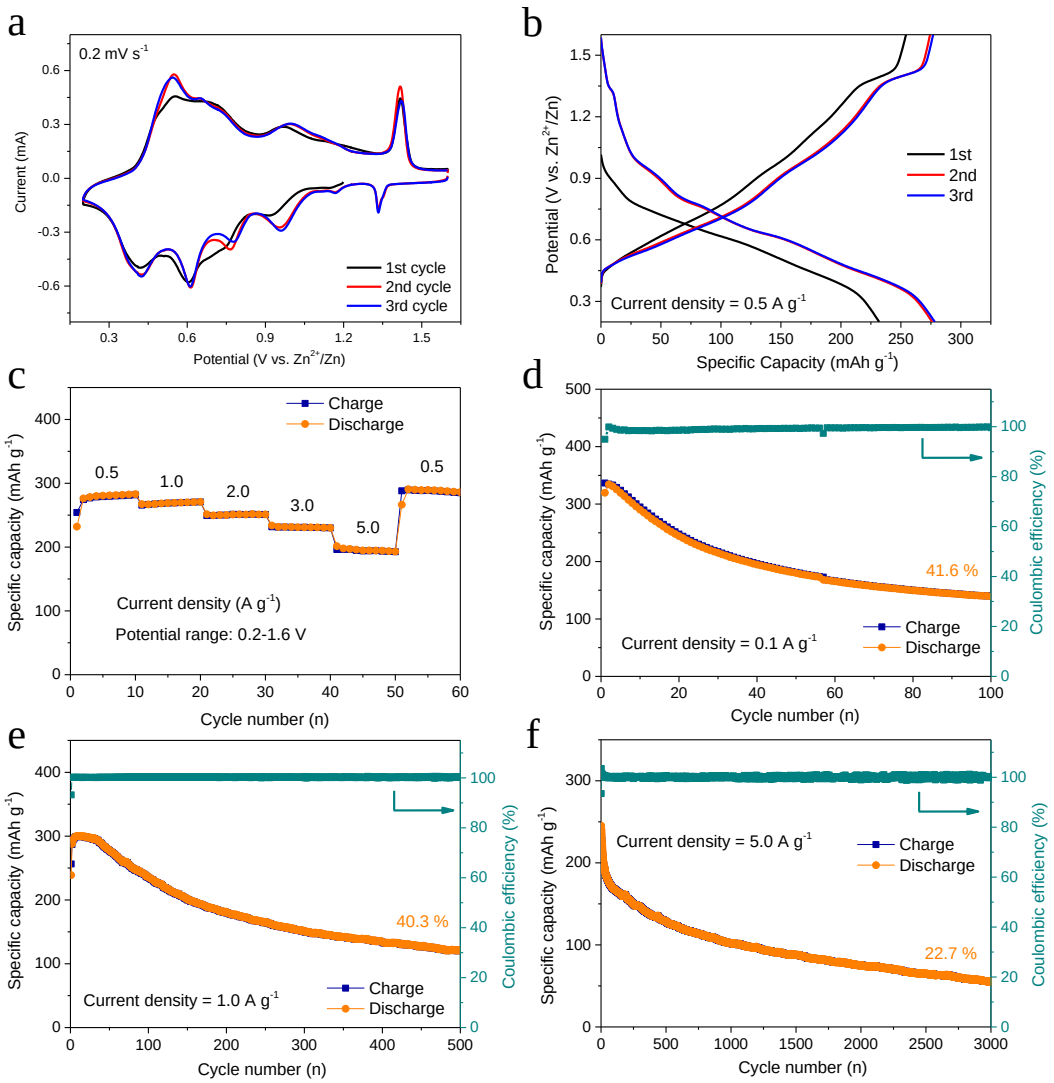

Fig. 5.7 Electrochemical properties of $H_2V_3O_8$ within the potential range from 0.2 to 1.6 V vs. Zn^{2+}/Zn: (a) The initial three CV curves with a scan rate of 0.2 mV s^{-1}; (b) galvanostatic charge-discharge profiles at a current density of 0.5 A g^{-1}; (c) rate capability with different current densities, and (e-f) cyclic stability and Coulombic efficiency at three different current densities.

As for the cyclic properties of VOOH at different current densities, they exhibit an activation process in the first several cycles, and their capacities step up first and then go down. The capacity retention of VOOH at 1.0 A g^{-1} is about 64.9 % after 500 cycles in Figure 5.6d. The Coulombic efficiency is low at first several cycles and then step up to about 100 % in the end. The capacity retentions at 0.1 and 5.0 A g^{-1} with 100 and 5,000 cycles are about 53.8 % and 51.3 % in Figure 5.8a and b, respectively. The higher current density shows better capacity retention. However, the cycle performance of VOOH is relatively poorer than some of vanadium-based cathode materials in Table 5.1. The impedance changes of VOOH electrode after different cycles are investigated by electrochemical impedance spectroscopy (EIS) in Figure 5.9. The electrochemical

reaction impedance in electrode and ion diffusion impedance in electrolyte can be determined by the semicircle in high frequency region and the straight line in low frequency region, respectively, which can be identified by the simulation equivalent circuit inserted in the figure. The simulated value of charge-transfer resistance (Rp) is 60 Ω at original state, becomes small after 10 cycle (7 Ω) and then changes to large after 50 (28 Ω) and 100 (35 Ω) cycles, which indicate the changes of interfacial charge-transfer resistances. The intercalation of Zn ions can reduce the resistance first, and then the change of electrode structure after many cycles can result in large resistance later. As for the cycle performance of $H_2V_3O_8$, they also are tested with current densities of 0.1, 1.0 and 5.0 A g^{-1} in Figure 5.7d-f. Their capacity retentions are worse than those of VOOH. The surface morphologies of VOOH electrode and zinc foil after 500 cycles at 1.0 A g^{-1} are also measured in Figure 5.10. Figure 5.10a and b show the large nanosheet on the surface of VOOH electrode, and Figure 5.10c and d exhibit the small nanoflake on the surface of zinc foil, but there is no zinc dendrite on zinc foil observed from cross-section images in Figure 5.10e-f. The XRD pattern of zinc foil after 500 cycles at 1.0 A g^{-1} is measured in Figure 5.11, which only shows the XRD peaks of Zn (JCPDS: 87-0713), indicating the small nanoflake is only zinc on the surface of zinc foil.

Table 5.1 Summary comparison on electrochemical performance of vanadium-based cathode materials in aqueous ZIBs.

Cathode materials	**Electrolytes**	**Specific capacity (mAh g^{-1} @A g^{-1})**	**Rate performance (mAh g^{-1} @A g^{-1})**	**Cycle performance (% / cycle @A g^{-1})**
lepidocrocite-VOOH (this work)	2M $Zn(CF_3SO_3)_2$	525.0 @0.5	440.0 @5.0	51.3 / 5,000 @5.0
VO_2[180]	3 M $Zn(CF_3SO_3)_2$	265.0 @0.1	133.0 @10	79.0 / 10,000 @10.0
VO_2 (B)[181]	3M Zn $(CF_3SO_3)_2$	357.0 @0.1	171.0 @51.2	91.2 / 300 @2.0
VO_2/RGO[182]	3M Zn $(CF_3SO_3)_2$	276.0 @0.1	120.0 @35.0	99.0 / 1,000 @4.0
V_2O_5[183]	21 M LiTFSI + 1 M $Zn(CF_3SO_3)_2$	242.0 @0.05	156.0 @1.0	80.0 / 2,000 @2.0
V_2O_5[184]	3 M $Zn(CF_3SO_3)_2$	465.0 @0.5	396 @10.0	91.1/ 4,000 @5.0
V_2O_5[185]	3 M $ZnSO_4$	224.0 @0.1	NA	75.0 / 400 @2.0
V_2O_5•nH_2O[186]	0.5 M $Zn(TFSI)_2$ in AN	196.0 @0.0144	130.0 @2.88	87.0 / 120 @0.0144

$V_2O_5 \cdot nH_2O$[187]	3 M $Zn(CF_3SO_3)_2$	381.0 @0.06	248 @30.0	71.0 / 900 @6.0
V_2O_5@PEDOT[188]	2.5 M $Zn(CH_3SO_3F)_2$	356.2 @0.1	232.2 @20	86.1 / 100 @0.2
$V_3O_7 \cdot H_2O$[173]	1 M $ZnSO_4$	375.0 @0.375	275.0 @3.0	80.0 / 200 @3.0
$H_2V_3O_8$[169]	3 M $Zn(CF_3SO_3)_2$	410.3 @0.1	113.9 @5.0	94.3 / 1,000 @5.0
$H_2V_3O_8$/graphene[168]	3 M $Zn(CF_3SO_3)_2$	394.0 @0.1	215.0 @3.0	87.0 / 2,000 @2.0
$V_{10}O_{24} \cdot 12H_2O$[189]	3 M $Zn(CF_3SO_3)_2$	164.5 @0.2	80.0 @10.0	80.1 / 3,000 @10.0
LiV_3O_8[190]	1 M $ZnSO_4$	256.0 @ 0.016	29 @1.666	75.0 / 65 @0.133
$Na_{0.33}V_2O_5$[191]	3 M $Zn(CF_3SO_3)_2$	367.1 @0.1	96.4 @2.0	93.0 / 1,000 @1.0
$Na_2V_6O_{16} \cdot 1.63H_2O$[40]	3 M $Zn(CF_3SO_3)_2$	352.0 @0.05	162.0 @2.0	90.0 / 6,000 @5.0
$Na_2V_6O_{16} \cdot 3H_2O$[41]	1 M $ZnSO_4$	361.0 @0.1	113.95 @20.0	80.0 / 1,000 @14.44
$Na_{1.1}V_3O_{7.9}$@rGO[192]	1 M $Zn(CF_3SO_3)_2$	220.0 @0.3	NA	77.0 / 100 @0.3
$Zn_2V_2O_7$[193]	1 M $ZnSO_4$	248.0 @0.05	54.0 @3.0	85.0 / 1,000 @4.0
$Zn_2(OH)VO_4$[36]	4% fumed silica into 2M $ZnSO_4$	204.0 @0.1	101.0 @10.0	89.0 / 2,000 @4.0
$Zn_{0.25}V_2O_5 \cdot nH_2O$[163]	1 M $ZnSO_4$	282.0 @0.3	183.0 @2.4	80.0 / 1,000 @2.4
$Zn_3V_2O_7(OH)_2 \cdot 2H_2O$[194]	1 M $ZnSO_4$	213.0 @0.05	76.0 @3.0	68.0 / 300 @0.2
$Mg_{0.34}V_2O_5 \cdot 0.84H_2O$[195]	3 M $Zn(CF_3SO_3)_2$	353.0 @0.05	81.0 @5.0	97.0 / 2,000 @5.0
$Ca_{0.25}V_2O_5$[196]	1 M $ZnSO_4$	340.0 @0.2C	72.0 @80C	64.0 / 5,000 @80C

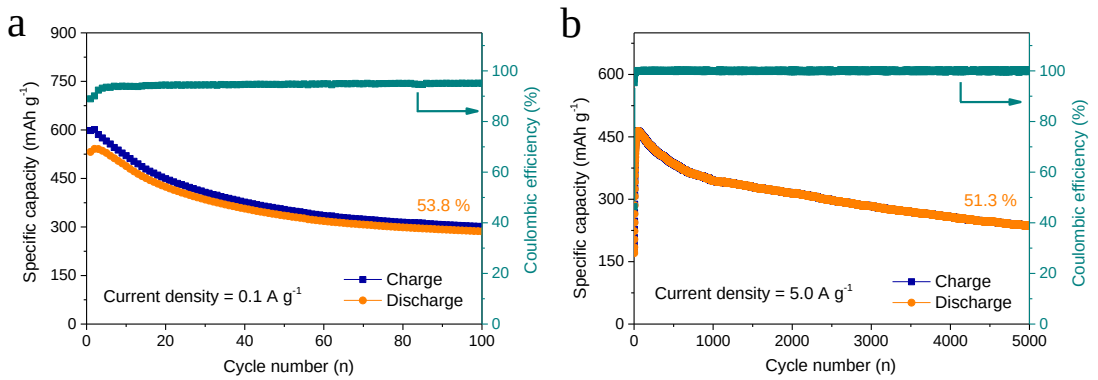

Fig. 5.8 Cyclic stability and Coulombic efficiency of lepidocrocite-VOOH at current densities of 0.1 (a) and 5.0 (b) A g^{-1}.

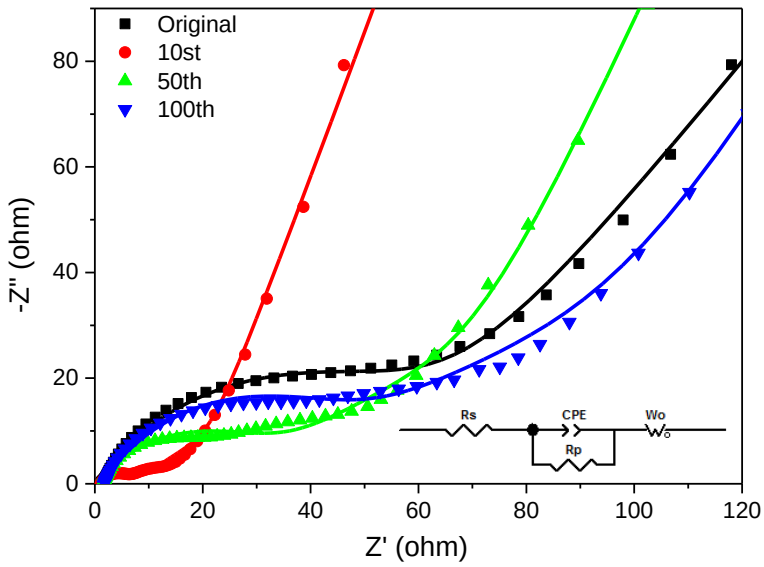

Fig. 5.9 Nyquist plots of lepidocrocite-VOOH electrode at 1.6 V vs. Zn^{2+}/Zn in original state and after 10, 50 and 100 cycles in 2 M $Zn(CF_3SO_3)_2$ aqueous electrolyte at 1.0 A g^{-1}. The solid lines are fittings using the same equivalent circuit model.

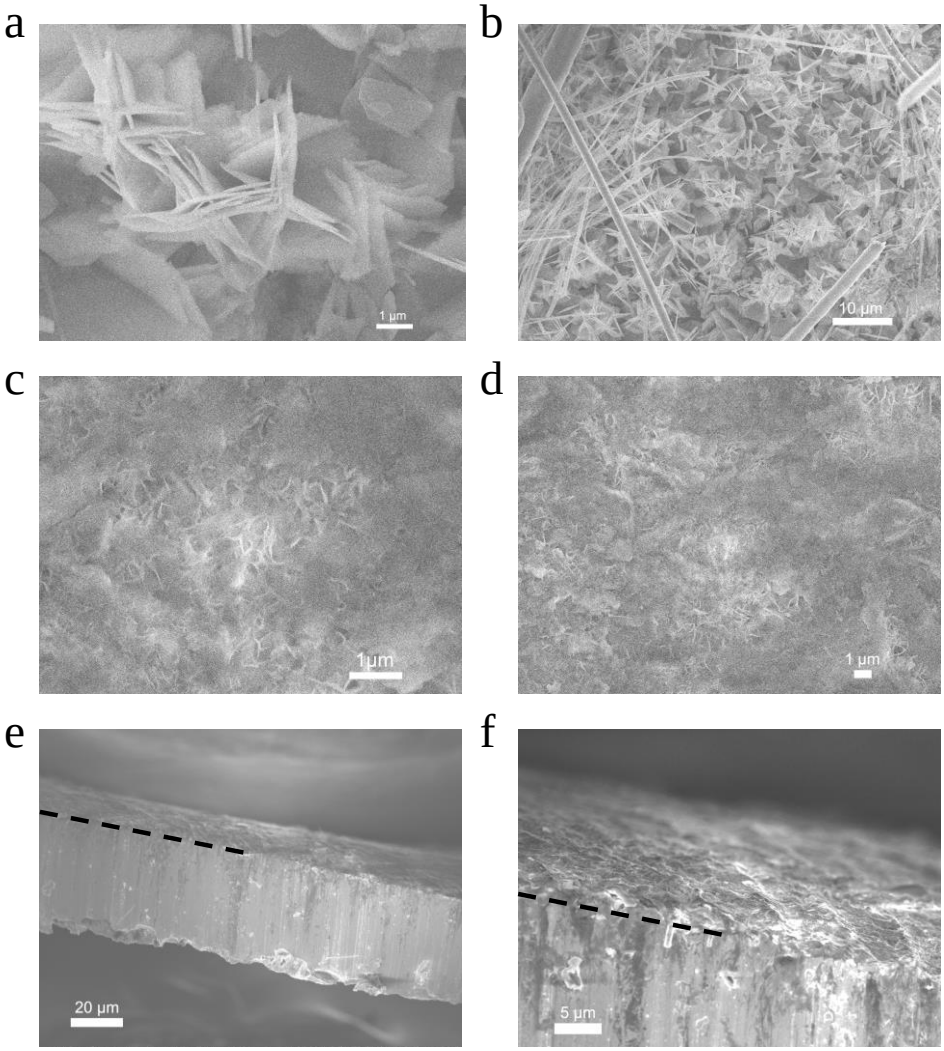

Fig. 5.10 Morphologies of electrodes after 500 cycles of charging/discharging at 1.0 A g^{-1} in the electrolyte of 2M $Zn(CF_3SO_3)_2$: (a-b) SEM images of the lepidocrocite-VOOH electrode (c-f) zinc foil. a-d correspond to the top views, e and f are cross-section images.

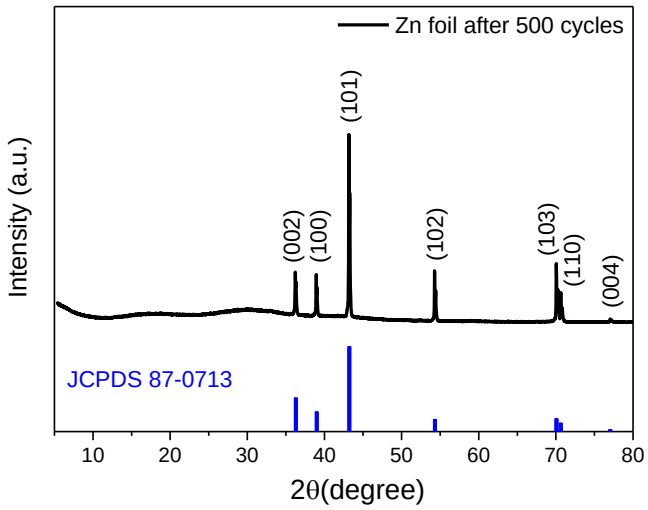

Fig. 5.11 The XRD pattern of zinc foil after 500 cycles at 1.0 A g^{-1}. All the peaks can be indexed to pure Zn (JCPDS 87-0713).

Electrochemical reaction kinetics

The electrochemical reaction kinetics of VOOH were investigated by galvanostatic intermittent titration technique (GITT) and redox capacity contribution analysis. The GITT measurement is applied to calculate the Zn^{2+} diffusion coefficients of $H_2V_3O_8$ and VOOH within the potential range from 0.2 to 1.6 V vs Zn^{2+}/Zn. Their discharge and charge profiles are presented in Figure 5.12a and c with an intermittent current density of 10 mA g^{-1}. Their coefficients in discharge and charge processes are within the range of 10^{-13} ~ 10^{-11} cm^2 s^{-1} (in Figure 5.12b and d), which are still higher than those of some electrode materials, such as the Li^+ ions in $LiFePO_4$ and TiO_2.[197-198]

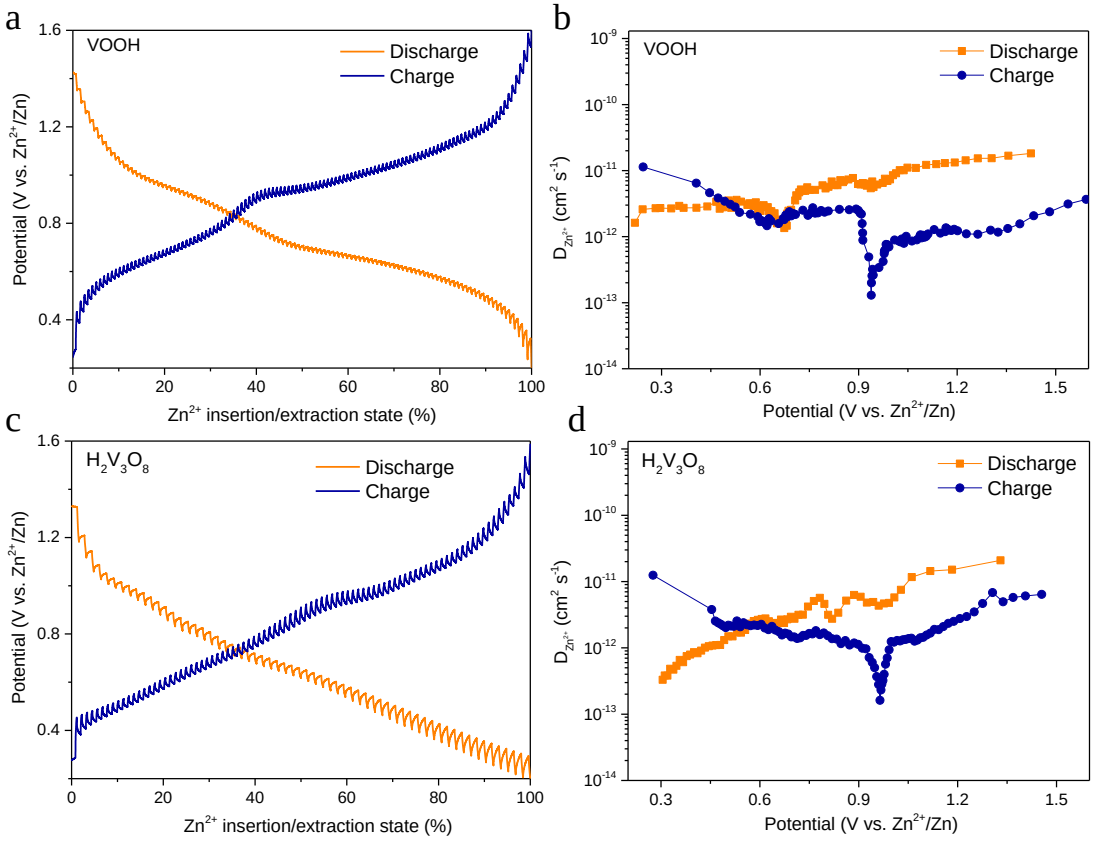

Fig. 5.12 Discharge and charge GITT curves and their corresponding Zn^{2+} diffusion coefficients of lepidocrocite-VOOH (a and b) and $H_2V_3O_8$ (c and d).

The good rate performance of VOOH has drawn our attention to understand its kinetics by performing the redox capacity contribution analysis. Its capacitance contribution, including capacitive-derived and diffusion-controlled capacitance contribution, can be distinguished quantitatively by conducting the standard CV fitting from the redox current contribution, which contains the capacitive-derived and diffusion-controlled current contribution.[199-200] The CV curves at different scan rates are presented in Figure 5.13a, which can be divided into two parts quantitatively. The capacitive-

derived and diffusion-controlled capacitance contribution can be separated at a fixed potential (V) from the current response (i). The capacitive-derived and diffusion-controlled parts are named as k_1v and $k_2v^{1/2}$, respectively, according to the relationship of $i(V) = k_1v + k_2v^{1/2}$. v is the scan rate, and k_1 and k_2 are constants. For instance, the capacitive-derived part (orange region with 66.7 %) and diffusion-controlled part (white region in royal blue curve with 33.3 %) of the VOOH electrode at a scan rate of 0.8 mV s^{-1} (in Figure 5.13b) are divided from the fitting analysis. With this approach, the capacitive-derived parts at different scan rates are distinguished and illustrated in Figure 5.13c. The ratio of capacitive-derived contribution increases as the increase of scan rate, which is reasonable due to the capacitive-derived process is faster than bulk diffusion.

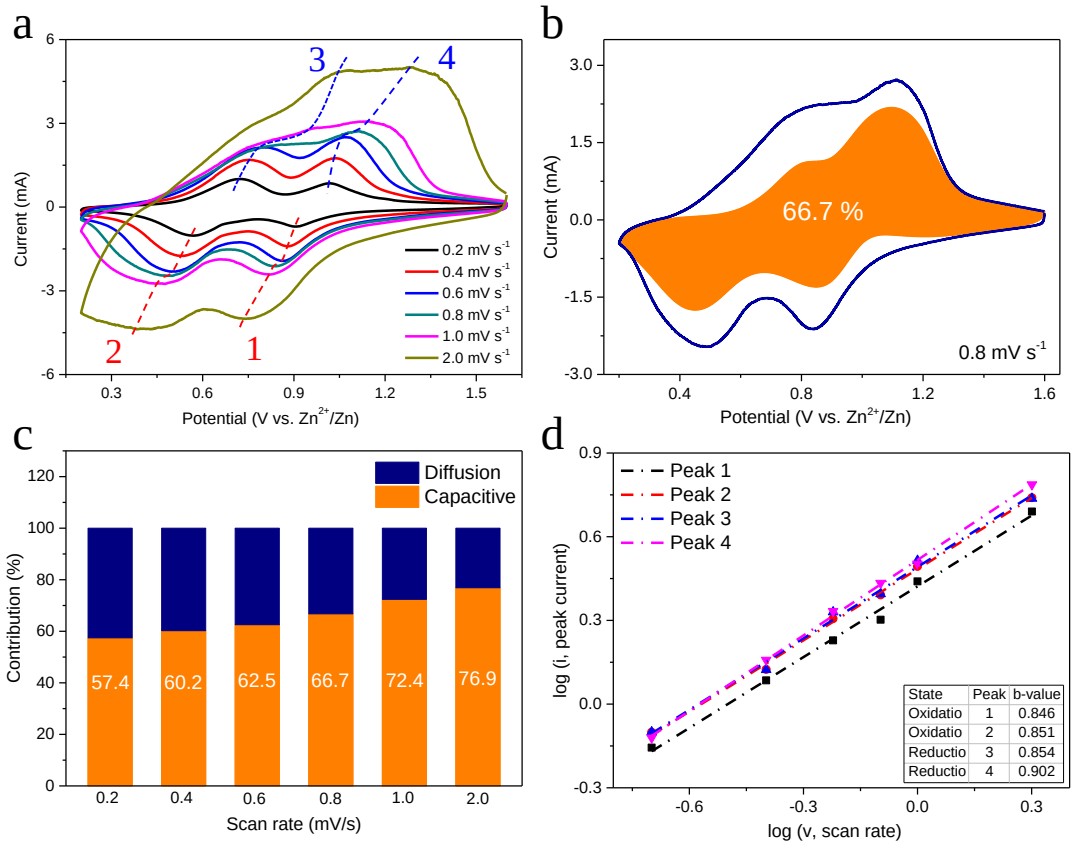

Fig. 5.13 Quantitative analysis of capacity contribution in lepidocrocite-VOOH working electrode: (a) CV curves at different scan rates; (b) diffusive-controlled current contribution (white region inside the CV curve) and capacitive-derived current contribution (shaded area) at the scan rate of 0.8 mV s^{-1}; (c) normalized current contribution ratios of diffusive-controlled and capacitive-derived parts at different scan rates; (d) relationship between the redox peak current and the voltage scan rate in a logarithm scale.

Moreover, the capacitive effect of the electrode at different redox peaks could be determined from CV profiles according to the equation between measured current (i) and scan rate (v): $i = av^b$, where a and b are parameters. When the b value approaches to 1, the electrode kinetics is mainly controlled by capacitive processes; while the b is close to

0.5, the electrode kinetics is mainly diffusion limited.[84-85] The detailed *b* values of the two pairs of redox peaks are fitted from CV profiles, as exhibited in Figure 5.13d, which imply the electrochemical reactions are mainly controlled by capacitive process.

5.3.3 Investigation of the storage mechanism

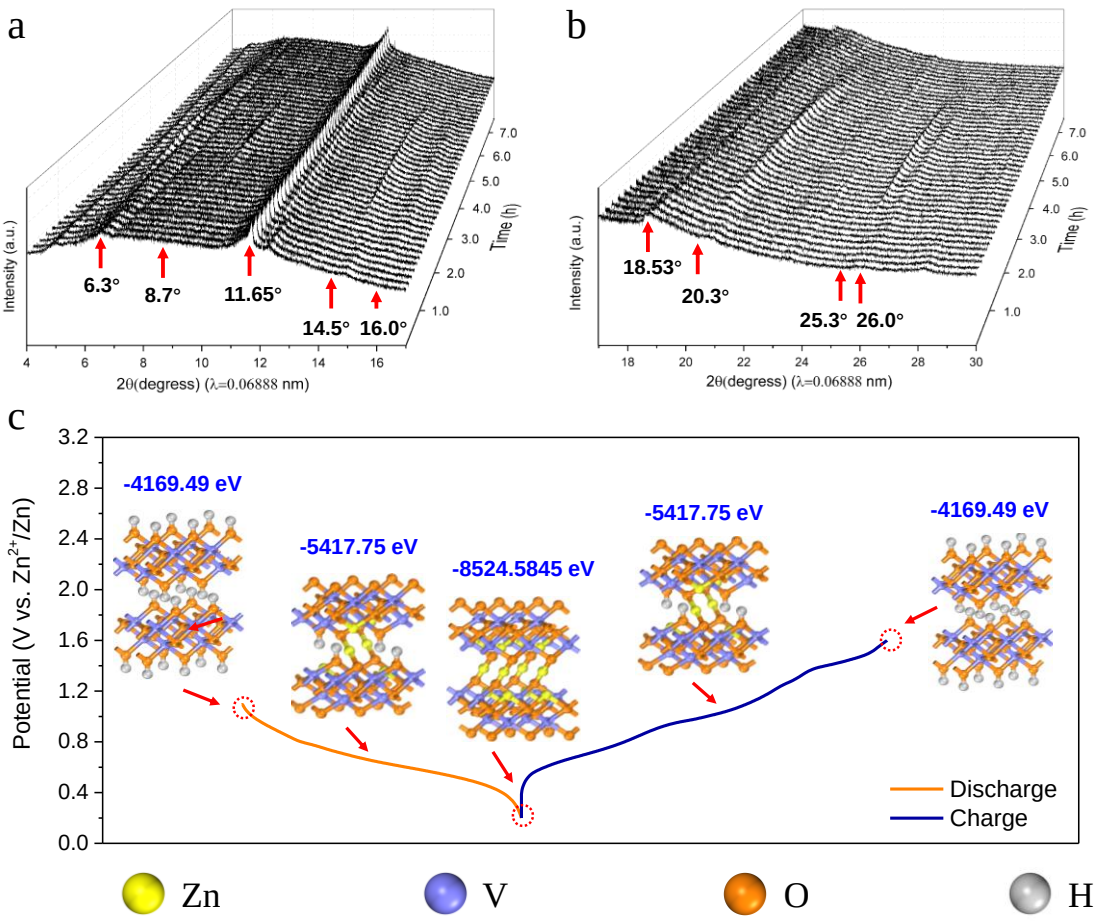

Fig. 5.14 The composition change and crystal structure evolution of lepidocrocite-VOOH in AZIB: the synchrotron-based in-situ XRD patterns within (a) 4 to 17° and (b) 17 to 30° during first discharge and charge processes, and (c) the schematics of inner structure changes and final energy values via density functional theory (DFT) calculation for the insertion and extraction of Zn ions.

The composition change and crystal structure evolution were investigated by synchrotron-based in-situ XRD, which has the advantages of high brilliance and stable radiation, which is better than general XRD instrument. Because the VOOH is powder sample, the fabrication of working electrode needs some additives and current collectors, the synchrotron-based in-situ XRD with high brilliance can transmit the current collector to detect the active material. The VOOH working electrode was assembled in a modified coin-cell, which was applied with a current density of 50 mA g^{-1} within the potential range from 0.2 to 1.6 V vs. Zn^{2+}/Zn. The XRD curves were collected with an interval of

about 10 minutes, which can provide the continuous and direct observation of composition change and crystal structure evolution. The in-situ XRD curves during discharge and charge processes are illustrated in Figure 5.14a and b within the ranges of 4 to 17° and 17 to 30°, respectively. The diffraction peaks located at 11.65 and 18.53° come from the (002) and (100) crystal planes of carbon, because the carbon paper is served as the substrate of working electrode to support the VOOH sample. In Figure 5.14a, a part of diffraction peak of 6.3°, resulting from the (020) crystal plane of VOOH, shift gradually to a lower degree (5.7°) during the discharge process, and then shift gradually back to 6.3° when the potential returns to 1.6 V in the end. The former and latter shifts indicate the expansion and recovery of interlayer spacing, which should be attributed to the insertion and extraction of zinc ions in the layered crystal structure of VOOH. A peak at around 20.3° in Figure 5.15b can be identified to the (051) crystal plane of VOOH. The peak becomes more and more obvious with a left shift to a low degree during the discharge process and then becomes weaker and weaker gradually with a right shift to initial degree during charge process. This phenomenon has also been found in other electrode materials, which should also be ascribed to the intercalation and deintercalation of zinc ions in the VOOH.[201]

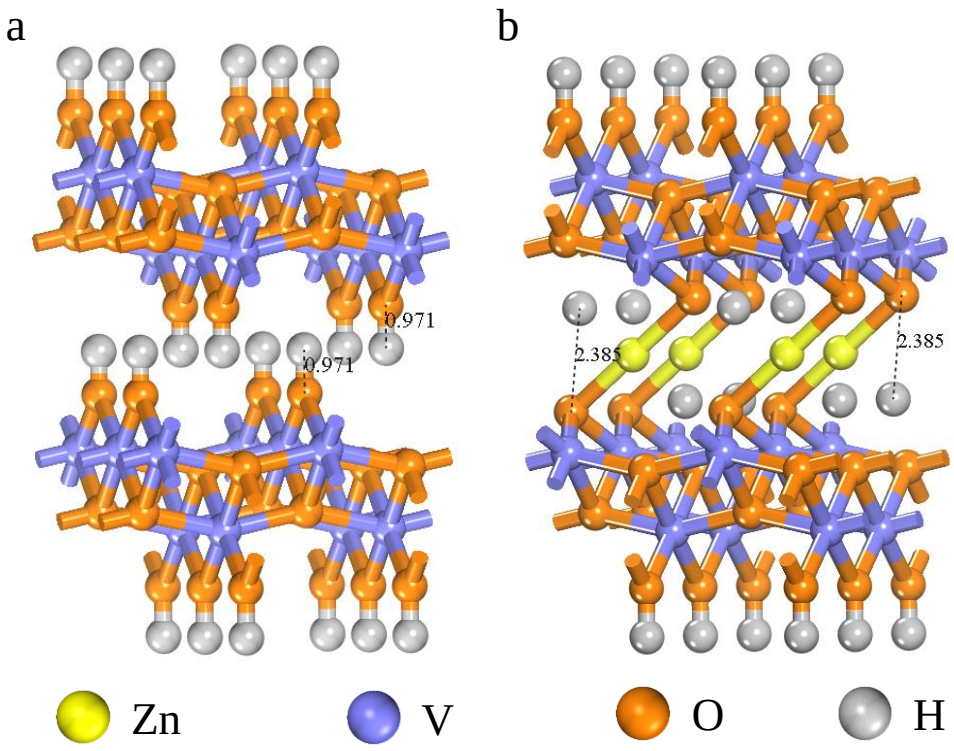

Fig. 5.15 The density functional theory (DFT) calculation of H-O bond change in lepidocrocite-VOOH (a) before and (b) after Zn^{2+} intercalation.

The new peak at 8.7° matches well with the (111) crystal plane of ZnV_2O_4 (JCPDS: 89-7413).[202-203] The peak becomes more distinct with more intercalation of zinc ions in the VOOH crystal structure, and then become weak due to the deintercalation of zinc ions. However, the valence state of vanadium has not been changed, it is still V^{3+} inside ZnV_2O_4. To explain the constant valence state, the crystal structure change in lepidocrocite-VOOH before and after Zn ions intercalation is simulated by DFT calculation in Figure 5.15. The results show that eight zinc ions can link to the oxygen atoms within a cell of $V_8O_{16}H_8$. The intercalation of zinc ions in VOOH will result in the rupture of hydrogen bonds that link to the oxygen atoms. And then zinc ion will replace the hydrogen atom and link two oxygen atoms that comes from two adjacent layers respectively, which can maintain the valence state of V^{3+} in four out of eight vanadium atoms. The formation of ZnV_2O_4 is also identified from in-situ XRD curves. Simultaneously, the other four zinc ions can directly link to oxygen atoms that do not link with hydrogen atoms in the crystal structure of VOOH. The insertion and extraction processes of Zn ions in VOOH is simulated by DFT calculation and presented in Figure 5.14c. And there are several new XRD peaks (at 14.5, 16.0, 25.3 and 26.0°) appear and disappear during the in-situ measurements. The peak of 16.0° matches well with the (101) crystal plane of ZnO (JCPDS: 89-7102). The other three peaks can be attributed to the crystal planes of V_2O_3.[204] These peaks validate the decomposition of a part of ZnV_2O_4 into V_2O_3 and ZnO, accompanying with the formation of ZnV_2O_4 during the discharge process. This similar phenomenon is also found in the aqueous Zn-MnO_2 battery. The generated MnOOH can be decomposed into Mn_2O_3 and H_2O via a conversion reaction during the discharge process and changed back to MnOOH reversibly during the charge process.[205]

The calculation also provides an interpretation about the high specific capacity of VOOH in AZIB, which shows that the eight zinc ions can be stored in a cell of $V_8O_{16}H_8$ during discharge process. Based on the simulation, the theoretical specific capacity of can be speculated as follow:

$$1\ \text{mol} * 2 * (6.02 * 10^{23})\ \text{mol}^{-1} * 1.602 * 10^{-19}\ \text{C} = 1.928808 * 10^5\ \text{C}\ (\text{A} * \text{s}) \quad (5.1)$$

$$1.928808 * 10^5\ \text{C}\ (\text{A} * \text{s}) * 1000/3600\ s = 53578\ \text{mAh} \quad (5.2)$$

$$53578\ \text{mAh}/(1\ \text{mol} * 83.948\ \text{g} * \text{mol}^{-1}) = 638.23\ \text{mAh}\ \text{g}^{-1} \quad (5.3)$$

Therefore, the theoretical specific capacity of VOOH in ZIB is about 638.23 mAh g^{-1}. Although the measured specific capacity in this work is higher than those of most

vanadium-based cathode materials in Table 5.1, the tremendous effort should be devoted to approaching the theoretical capacity and enhance the cycle performance.

5.4 Conclusion

The lepidocrocite-VOOH with a low valence state of V^{3+} has been introduced in AZIBs, which is demonstrated to be a promising cathode material. It exhibits high specific capacities of about 525 and 440 mAh g^{-1} at the rates of 0.5 and 5.0 A g^{-1} and good rate performance within the potential range from 0.2 to 1.6 V vs Zn^{2+}/Zn. The GITT measurement reveals the Zn^{2+} diffusion coefficients are in the range of 10^{-13} ~ 10^{-11} cm^2 s^{-1} during cycles. The redox capacity contribution analysis uncovers the main pseudocapacitive contribution during Zn^{2+} insertion and extraction processes. The combined in-situ XRD characterization and DFT calculation provide a new storage mechanism of zinc ions in vanadium-based materials. Zn ions are reversibly stored in the layers and interlayers by replacing the H atoms and bonding two adjacent layers within the lepidocrocite-VOOH.

Chapter 6 Summary and Outlook

6.1 Summary

This thesis study deals with the design of layered electrode materials and their metal ion storage mechanisms in sodium ion battery and aqueous zinc ion battery. The electrochemical properties and electrochemical reaction processes of a few types of layered materials were investigated systematically with the help of ex-situ and in-situ characterization techniques, and DFT calculations.

Layered transition metal dichalcogenides (TMDs) as anode materials are studied in SIBs. Their electrochemical properties and related storage mechanisms of sodium ions were investigated in detail. First, $MoSe_2$ nanosheet uniformly distributed in N-doped carbon matrix with an urchin-like morphology was synthesized in Chapter 3. The purpose is to increase the electrical conductivity and realize long cycle stability for sodium ion storage. And the crystal structure changes of $MoSe_2$ associated with electrochemical reactions in SIB were also investigated using ex-situ XRD technique, which implied an irreversible conversion reaction during the first discharge process within the potential range from 0.01 to 3.0 V vs. Na^+/Na. However, sometimes the ex-situ characterization can be influenced by the unwanted ambient environment, such as the natural oxidation of non-oxide metal compounds when the samples are unavoidably exposed to air ambient. Hence, a direct observation of the composition and crystal structure evolution will be more favorable in order to disclose the storage mechanism. That is the reason why currently in-situ characterizations are becoming popular in battery research. In Chapter 4 of this thesis, the electrochemical reaction processes of layered TMD materials are studied systematically using both ex-situ and in-situ characterization techniques. MoS_2 nanoflakes were first hydrothermal grown on graphene-like carbon foam (MoS_2/graphene foam), and then were underwent selenization treatment in order to substitute sulfur partly to form $MoS_{2-x}Se_x$/graphene foam. The in-situ Raman spectroscopy combined with ex-situ XRD measurement recorded within different potential ranges further revealed that the 2D layered structure in $MoS_{2-x}Se_x$/graphene foam could be preserved with the Na-ion intercalation process under the potential range above 0.5 V vs Na^+/Na. In contrast, deep discharge to 0.01 V would lead to damage of the layered structure and aggregation. And electrochemical measurements also revealed the capacitance retention could be improved by choosing an appropriate potential range

to utilize the intercalation and deintercalation processes and avoid the irreversible decomposition. Moreover, the selenium substitution in $MoS_{2-x}Se_x$/graphene foam has improved the rate performance due to higher pseudocapacitive contribution than the MoS_2, which results from the expanded interlayer spacing of $MoS_{2-x}Se_x$ by selenium substitution. Therefore, the combination of in-situ observation and delicate control of electrochemical measurements is effective in understanding the electrochemical reaction processes and associated storage mechanism. This result may provide insight for better design of electrode materials.

Because aqueous ZIB has the advantages of low cost and high safety, it has been considered as the promising alternative to alkaline metal ion batteries with organic electrolyte. Currently, extensive efforts are being devoted to exploring new electrode materials and investigation of the storage mechanisms. Many kinds of vanadium-based cathode materials have been reported, but most of them possess high valence states of vanadium, such as V^{4+} and V^{5+}. In this thesis (Chapter 5), the low valance (V^{3+}) state vanadium material (lepidocrocite-VOOH) has been introduced for aqueous ZIB. The VOOH nanobelt electrode exhibits high specific capacities of about 525 and 400 mAh g^{-1} at the current densities of 0.5 and 5.0 A g^{-1} within the potential range from 0.2 to 1.6 V vs Zn^{2+}/Zn. GITT measurements reveal the relatively good electrochemical reaction kinetics of VOOH in aqueous ZIB during cycles. The standard cyclic voltammetry fitting implies dominating pseudocapacitive contribution to the capacity during Zn^{2+} ion insertion and extraction processes in the nanobelts. The in-situ XRD characterization combined with DFT calculation reveal a different storage mechanism of zinc ions different from other vanadium-based materials. It is found herein that Zn^{2+} ions are reversibly stored in the layers and interlayers by replacing the H atoms and bonding two adjacent layers within the lepidocrocite-VOOH. This work provides an insight into the exploration of new cathode materials in aqueous ZIBs.

6.2 Outlook

For the development of electrochemical metal-ion batteries, particularly the SIBs and AZIBs discussed in this thesis, much efforts should be devoted to optimizing their electrochemical performance. Here, I will introduce the electrolyte modification for SIB and interface engineering for AZIB.

(1) Electrolyte modification for sodium-ion battery: Severe safety concerns are impeding the large-scale commercialization of SIB. The severe danger arises from the subsequent fire ignition and explosion of the organic electrolyte supported by the oxygen evolved from the cathode materials or surrounding air because the combustion energy is several times higher than the electrical energy stored in a battery. The conventional electrolytes used in SIBs are highly flammable and volatile organics, for example, the 1.0 M $NaPF_6$ in ethylene carbonate (EC) and dimethyl carbonate (DEC), which may cause catastrophic fires or explosions. Thus, we need to do some electrolyte modifications to improve the safety issues. As for electrolyte, we can study the additive types, concentration, component ratios and so on. Moreover, we can adopt some characterization methods, such as the Raman spectroscopy and FTIR, to study their physical and chemical properties. Theory calculation of molecular dynamics simulation is also an important tool to predict their molecular structures and chemical energies, which is highly efficient to choose suitable electrolytes in different working situations. For example, as for the severe safety issue in conventional organic electrolyte, researchers can adopt flame-retardant solvents or additives into the electrolytes, such as those containing phosphorus or fluorine, which can increase the flash point and improve the safety concerns remarkably. Meanwhile, the high-concentration electrolyte is also an effective methodology to improve its flash point and provide a robust and stable solid-state electrolyte interface (SEI), which can improve the safety issue and long-term capacity retention. For example, Yamada's group introduced a 3.3 M NaFSA/TMP electrolyte for SIB, which has higher flash point and Columbic efficiency than those of 1.0 M NaFSA/TMP electrolyte.[206] The higher concentration of electrolyte can also provide a more robust SEI layer than that with low-concentration electrolyte, which can suppress parasitic reactions. They also used the molecular dynamics simulation to calculate the coordination structures of electrolytes with different concentrations. They found the 1.0 M electrolyte has many free TMP molecules and FSA^- anions, because the solvent-to-salt ratio (7.6) is larger than the typical coordination number (5) of Na^+. In contrast, in the 3.3 M electrolyte, ~95% of the TMP molecules are coordinated with Na^+ cations, and over 80% of the FSA^- anions are in an aggregate state with each FSA^- coordinating to two or more Na^+, forming a peculiar three-dimensional network structure. These structure features contribute to improved battery safety. Thus, electrolyte modification is an effective and promising method to improve the safety issues and electrochemical performance.

(2) Interface engineering for aqueous zinc-ion battery: There are two electrolyte-electrode interfaces in battery, between anode and electrolyte and between cathode and electrolyte. Metal ions should transmit the interfaces to other side and some parasitic reactions happen at the interfaces, so the investigation of interface is very significant and meaningful to optimize the electrochemical performance. In aqueous zinc-ion battery, there is a potential danger of zinc dendrite growth for large-scale energy storage devices, which need stable thousands of charging/discharging cycles. As for the study of interface, we can study the chemical composition by some characterization methods, such as XRD, XPS and Raman spectroscopy, and investigate its formation and evolution by some in-situ characterization tools. A stable and robust interface can have a thin layer, which can avoid the pulverization of electrode and suppress the parasitic reactions. Thus, the studies of stable interface and zinc dendrite suppression are promising direction to optimize AZIBs. For example, the chemical composition of interface has much influence on the electrochemical performance. Cui's group found the F-rich interface can suppress the zinc-dendrite growth and improve the long-term cycle performance.[207] They pretreated the zinc metal with $Zn(TFSI)_2$-acetamide (Ace) electrolyte, which result in the in-situ formation of a F-rich SEI layer. The F-rich interface was demonstrated by XPS characterization. They tested the zinc plating and found the zinc foil with the F-rich layer does not have zinc dendrites, but the zinc foil without the interface has severe and obvious dendrites. They also found the battery with the F-rich SEI-coated zinc foil can provide longer stable capacity than that without the interface. As for the battery without the F-rich SEI-coated zinc foil, it has a short circuit during cycles, which results from the zinc dendrite. Meanwhile, the special cell design is also important to study the interface, researchers can learn a lot from in-situ working cells.

Publication List

(1) **Guichong Jia,** Dongliang Chao, Bo Ouyang, Kun Xu, Zheng Zhang, Hong Jin Fan*, Self-sacrificial Template Induced Synthesis of Lepidocrocite-VOOH Nanobelts for Aqueous Zinc-ion Battery; **(To be submitted)**

(2) **Guichong Jia,** Dongliang Chao*, Nguyen Huy Tiep, Zheng Zhang, and Hong Jin Fan*, Intercalation Na-Ion Storage in Two-Dimensional $MoS_{2-x}Se_x$ and Capacity Enhancement by Selenium Substitution, Energy Storage Mater. 14,136-142 (2018); **(Front Cover)**

(3) **Guichong Jia,** Huanwen Wang, Dongliang Chao, Haiyong He, Nguyen Huy Tiep, Yongqi Zhang, Zheng Zhang, Hong Jin Fan*, Ultrathin $MoSe_2$ @N-doped Carbon Composite Nanospheres for Stable Na-Ion Storage, Nanotechnology 28, 42LT01 (2017); **(Front Cover)**

(4) Yongqi Zhang[#], **Guichong Jia[#],** Huanwen Wang, Bo Ouyang, Rajdeep Singh Rawat, and Hong Jin Fan*, Ultrathin CNTs@FeOOH Nanoflakes Core/Shell Networks as Efficient Electrocatalysts for Oxygen Evolution Reaction, Mater. Chem. Front., 2017,1,709-715; **(Co-first Author)**

(5) Bo Ouyang, Dongliang Chao, **Guichong Jia,** Zheng Zhang, Hong Jin Fan*, Rajdeep Singh Rawat*, Hierarchical vertical graphene nanotube arrays via universal carbon plasma processing strategy: A platform for high-rate performance battery electrodes, Energy Storage Mater. 18, 462-469 (2019);

(6) Kun Xu, Yiqiang Sun, Yuanmiao Sun, Yongqi Zhang, **Guichong Jia,** Qinghua Zhang, Lin Gu, Shuzhou Li, Yue Li*, and Hong Jin Fan*, Yin-Yang Harmony: Metal and Non-metal Dual-Doping Boosts Electrocatalytic Activity for Alkaline Hydrogen Evolution, ACS Energy Lett., 3, 2750–2756 (2018);

(7) Dongliang Chao, Bo Ouyang, Pei Liang, Tran Thi Thu Huong, **Guichong Jia,** Hui Huang, Xinhui Xia, Rajdeep Singh Rawat*, and Hong Jin Fan*, C-Plasma of Hierarchical Graphene Survives SnS Bundles for Ultra-Stable and High Volumetric Na-Ion Storage, Adv. Mater. 6, 1804833 (2018);

(8) Jing Xu, **Guichong Jia,** Wenjie Mai and Hong Jin Fan*, Energy Storage Performance Enhancement by Surface Engineering of Electrode Materials, Adv. Mater. Interface, 1600430 (2016);

(9) Huanwen Wang, **Guichong Jia,** Yuanyuan Guo, Yongqi Zhang, Hongbo Geng, Jing Xu, Wenjie Mai, Qingyu Yan, and Hong Jin Fan*, Atomic Layer Deposition of Amorphous TiO_2 on Carbon Nanotube Networks and Their Superior Li and Na Ion Storage Properties, Adv. Mater. Interface, 3, 1600375 (2016);

(10) Yongqi Zhang, Bo Ouyang, Jing Xu, **Guichong Jia,** Shi Chen, Rajdeep Singh Rawat, and Hong Jin Fan*, Rapid synthesis of CoN nanowires: highly efficient and low-cost catalyst for oxygen evolution, Angew. Chem. Int. Ed. 55(30), 8670-8674 (2016).

References

1. Li, M.; Lu, J.; Chen, Z.; Amine, K., *Adv Mater* 2018, e1800561.
2. Dunn, B.; Kamath, H.; Tarascon, J.-M., *Science* 2011, *334* (6058), 928-935.
3. Winter, M.; Barnett, B.; Xu, K., *Chem Rev* 2018.
4. Liu, C.; Li, F.; Ma, L. P.; Cheng, H. M., *Adv Mater* 2010, *22* (8), E28-62.
5. Yabuuchi, N.; Kubota, K.; Dahbi, M.; Komaba, S., *Chemical reviews* 2014, *114* (23), 11636-11682.
6. Kim, H.; Kim, H.; Ding, Z.; Lee, M. H.; Lim, K.; Yoon, G.; Kang, K., *Adv. Energy Mater.* 2016, *6* (19), 1600943.
7. Dai, Z.; Mani, U.; Tan, H. T.; Yan, Q., *Small Methods* 2017, *1* (5).
8. Chayambuka, K.; Mulder, G.; Danilov, D. L.; Notten, P. H. L., *Adv. Energy Mater.* 2018.
9. Xiang, X.; Zhang, K.; Chen, J., *Adv Mater* 2015, *27* (36), 5343-64.
10. Pu, X.; Wang, H.; Zhao, D.; Yang, H.; Ai, X.; Cao, S.; Chen, Z.; Cao, Y., *Small* 2019, e1805427.
11. Wang, Y.; Yu, X.; Xu, S.; Bai, J.; Xiao, R.; Hu, Y. S.; Li, H.; Yang, X. Q.; Chen, L.; Huang, X., *Nat Commun* 2013, *4*, 2365.
12. Lee, H. W.; Wang, R. Y.; Pasta, M.; Woo Lee, S.; Liu, N.; Cui, Y., *Nat Commun* 2014, *5*, 5280.
13. Lu, Y.; Wang, L.; Cheng, J.; Goodenough, J. B., *Chem Commun (Camb)* 2012, *48* (52), 6544-6.
14. Slater, M. D.; Kim, D.; Lee, E.; Johnson, C. S., *Advanced Functional Materials* 2013, *23* (8), 947-958.
15. Liu, T.; Zhang, Y.; Jiang, Z.; Zeng, X.; Ji, J.; Li, Z.; Gao, X.; Sun, M.; Lin, Z.; Ling, M.; Zheng, J.; Liang, C., *Energy & Environmental Science* 2019.
16. Komaba, S.; Mikumo, T.; Ogata, A., *Electrochem. Commun.* 2008, *10* (9), 1276-1279.
17. Koo, B.; Chattopadhyay, S.; Shibata, T.; Prakapenka, V. B.; Johnson, C. S.; Rajh, T.; Shevchenko, E. V., *Chemistry of Materials* 2013, *25* (2), 245-252.
18. Rudola, A.; Saravanan, K.; Mason, C. W.; Balaya, P., *Journal of Materials Chemistry A* 2013, *1* (7), 2653.
19. Senguttuvan, P.; Rousse, G.; Seznec, V.; Tarascon, J.-M.; Palacín, M. R., *Chemistry of Materials* 2011, *23* (18), 4109-4111.
20. Tan, H.; Chen, D.; Rui, X.; Yu, Y., *Advanced Functional Materials* 2019.
21. Liu, Y.; Yang, C.; Zhang, Q.; Liu, M., *Energy Storage Materials* 2019.
22. Hu, X.; Zhang, W.; Liu, X.; Mei, Y.; Huang, Y., *Chem Soc Rev* 2015, *44* (8), 2376-404.
23. Chen, X.; Shen, X.; Li, B.; Peng, H. J.; Cheng, X. B.; Li, B. Q.; Zhang, X. Q.; Huang, J. Q.; Zhang, Q., *Angew Chem Int Ed Engl* 2017.
24. Jin, T.; Han, Q.; Jiao, L., *Adv Mater* 2019, e1806304.
25. Fang, G.; Zhou, J.; Pan, A.; Liang, S., *ACS Energy Letters* 2018, 2480-2501.
26. Yu, P.; Zeng, Y.; Zhang, H.; Yu, M.; Tong, Y.; Lu, X., *Small* 2019, e1804760.
27. Zeng, X.; Hao, J.; Wang, Z.; Mao, J.; Guo, Z., *Energy Storage Materials* 2019.
28. Song, M.; Tan, H.; Chao, D.; Fan, H. J., *Advanced Functional Materials* 2018.
29. Xu, C.; Li, B.; Du, H.; Kang, F., *Angew Chem Int Ed Engl* 2012, *51* (4), 933-5.
30. Sun, W.; Wang, F.; Hou, S.; Yang, C.; Fan, X.; Ma, Z.; Gao, T.; Han, F.; Hu, R.; Zhu, M.; Wang, C., *J Am Chem Soc* 2017, *139* (29), 9775-9778.
31. Wan, F.; Zhang, L.; Dai, X.; Wang, X.; Niu, Z.; Chen, J., *Nat Commun* 2018, *9* (1), 1656.
32. Pan, H.; Shao, Y.; Yan, P.; Cheng, Y.; Han, K. S.; Nie, Z.; Wang, C.; Yang, J.; Li, X.; Bhattacharya, P.; Mueller, K. T.; Liu, J., *Nature Energy* 2016, *1* (5), 16039.
33. Li, H.; Xu, C.; Han, C.; Chen, Y.; Wei, C.; Li, B.; Kang, F., *Journal of The Electrochemical Society* 2015, *162* (8), A1439-A1444.

34. Qiu, W.; Li, Y.; You, A.; Zhang, Z.; Li, G.; Lu, X.; Tong, Y., *Journal of Materials Chemistry A* 2017, *5* (28), 14838-14846.
35. Wang, L.-P.; Li, N.-W.; Wang, T.-S.; Yin, Y.-X.; Guo, Y.-G.; Wang, C.-R., *Electrochim. Acta* 2017, *244*, 172-177.
36. Chao, D.; Zhu, C. R.; Song, M.; Liang, P.; Zhang, X.; Tiep, N. H.; Zhao, H.; Wang, J.; Wang, R.; Zhang, H.; Fan, H. J., *Adv Mater* 2018, e1803181.
37. Sun, K. E.; Hoang, T. K.; Doan, T. N.; Yu, Y.; Zhu, X.; Tian, Y.; Chen, P., *ACS Appl Mater Interfaces* 2017, *9* (11), 9681-9687.
38. Parker, J. F.; Chervin, C. N.; Pala, I. R.; Machler, M.; Burz, M. F.; Long, J. W.; Rolison, D. R., *Science* 2017, *356* (6336), 415-418.
39. Zhao, K.; Wang, C.; Yu, Y.; Yan, M.; Wei, Q.; He, P.; Dong, Y.; Zhang, Z.; Wang, X.; Mai, L., *Advanced Materials Interfaces* 2018, *5* (16).
40. Hu, P.; Zhu, T.; Wang, X.; Wei, X.; Yan, M.; Li, J.; Luo, W.; Yang, W.; Zhang, W.; Zhou, L.; Zhou, Z.; Mai, L., *Nano Lett* 2018, *18* (3), 1758-1763.
41. Soundharrajan, V.; Sambandam, B.; Kim, S.; Alfaruqi, M. H.; Putro, D. Y.; Jo, J.; Kim, S.; Mathew, V.; Sun, Y. K.; Kim, J., *Nano Lett* 2018, *18* (4), 2402-2410.
42. Wang, F.; Borodin, O.; Gao, T.; Fan, X.; Sun, W.; Han, F.; Faraone, A.; Dura, J. A.; Xu, K.; Wang, C., *Nat Mater* 2018, *17* (6), 543-549.
43. Chao, D.; Zhou, W.; Ye, C.; Zhang, Q.; Chen, Y.; Gu, L.; Davey, K.; Qiao, S. Z., *Angew Chem Int Ed Engl* 2019.
44. Xu, W.; Zhao, K.; Huo, W.; Wang, Y.; Yao, G.; Gu, X.; Cheng, H.; Mai, L.; Hu, C.; Wang, X., *Nano Energy* 2019, *62*, 275-281.
45. Ding, Y.; Cano, Z. P.; Yu, A.; Lu, J.; Chen, Z., *Electrochemical Energy Reviews* 2019, *2* (1), 1-28.
46. Li, L.; Zheng, Y.; zhang, s.; Yang, J.; Shao, Z.; Guo, Z., *Energy & Environmental Science* 2018.
47. Larcher, D.; Tarascon, J. M., *Nat Chem* 2015, *7* (1), 19-29.
48. Hong, Y.-S.; Li, N.; Chen, H.; Wang, P.; Song, W.-L.; Fang, D., *Energy Storage Materials* 2018, *11*, 118-126.
49. Lu, J., *Small Methods* 2018, *2* (8).
50. Sun, J.; Lee, H. W.; Pasta, M.; Yuan, H.; Zheng, G.; Sun, Y.; Li, Y.; Cui, Y., *Nat Nanotechnol* 2015, *10* (11), 980-5.
51. Wen, Y.; He, K.; Zhu, Y.; Han, F.; Xu, Y.; Matsuda, I.; Ishii, Y.; Cumings, J.; Wang, C., *Nat Commun* 2014, *5*, 4033.
52. Wang, J. W.; Liu, X. H.; Mao, S. X.; Huang, J. Y., *Nano Lett* 2012, *12* (11), 5897-902.
53. Wu, D.; Li, X.; Xu, B.; Twu, N.; Liu, L.; Ceder, G., *Energy Environ. Sci.* 2015, *8* (1), 195-202.
54. Ren, Y.; Zuo, X., *Small Methods* 2018, *2* (8).
55. Li, W.; Li, M.; Hu, Y.; Lu, J.; Lushington, A.; Li, R.; Wu, T.; Sham, T.-K.; Sun, X., *Small Methods* 2018, *2* (8).
56. Shadike, Z.; Zhou, Y. N.; Chen, L. L.; Wu, Q.; Yue, J. L.; Zhang, N.; Yang, X. Q.; Gu, L.; Liu, X. S.; Shi, S. Q.; Fu, Z. W., *Nat Commun* 2017, *8* (1), 566.
57. Alemu, T.; Wang, F. M., *J Synchrotron Radiat* 2018, *25* (Pt 1), 151-165.
58. Liu, X. H.; Huang, J. Y., *Energy & Environmental Science* 2011, *4* (10).
59. Lu, X.; Adkins, E. R.; He, Y.; Zhong, L.; Luo, L.; Mao, S. X.; Wang, C.-M.; Korgel, B. A., *Chemistry of Materials* 2016, *28* (4), 1236-1242.
60. Zhu, C.; Xu, F.; Min, H.; Huang, Y.; Xia, W.; Wang, Y.; Xu, Q.; Gao, P.; Sun, L., *Advanced Functional Materials* 2017, *27* (17).
61. Boebinger, M. G.; Xu, M.; Ma, X.; Chen, H.; Unocic, R. R.; McDowell, M. T., *Journal of Materials Chemistry A* 2017, *5* (23), 11701-11709.
62. Lacey, S. D.; Wan, J.; von Wald Cresce, A.; Russell, S. M.; Dai, J.; Bao, W.; Xu, K.; Hu, L., *Nano Lett* 2015, *15* (2), 1018-24.

63. Schröder, D.; Bender, C. L.; Arlt, T.; Osenberg, M.; Hilger, A.; Risse, S.; Ballauff, M.; Manke, I.; Janek, J., *Journal of Physics D: Applied Physics* 2016, *49* (40).
64. Shen, Y.; Pedersen, E. E.; Christensen, M.; Iversen, B. B., *Rev Sci Instrum* 2014, *85* (10), 104103.
65. Zhang, L.; Guo, X.; Huang, J.; Qu, Y.; Niu, C.; Du, Z.; Li, D.; Chen, Y., *Frontiers in Energy Research* 2018, *6*.
66. Aquilanti, G.; Giorgetti, M.; Dominko, R.; Stievano, L.; Arčon, I.; Novello, N.; Olivi, L., *Journal of Physics D: Applied Physics* 2017, *50* (7).
67. Yu, X.; Pan, H.; Zhou, Y.; Northrup, P.; Xiao, J.; Bak, S.; Liu, M.; Nam, K. W.; Qu, D.; Liu, J., *Adv. Energy Mater.* 2015, *5* (16), 1500072.
68. Wang, Q. C.; Hu, E.; Pan, Y.; Xiao, N.; Hong, F.; Fu, Z. W.; Wu, X. J.; Bak, S. M.; Yang, X. Q.; Zhou, Y. N., *Advanced Science* 2017, *4* (11), 1700219.
69. Zhang, X.; Verhallen, T. W.; Labohm, F.; Wagemaker, M., *Adv. Energy Mater.* 2015, *5* (15), 1500498.
70. Nazer, N. S.; Yartys, V. A.; Azib, T.; Latroche, M.; Cuevas, F.; Forseth, S.; Vie, P. J. S.; Denys, R. V.; Sørby, M. H.; Hauback, B. C.; Arnberg, L.; Henry, P. F., *Journal of Power Sources* 2016, *326*, 93-103.
71. Bhattacharyya, R.; Key, B.; Chen, H.; Best, A. S.; Hollenkamp, A. F.; Grey, C. P., *Nat Mater* 2010, *9* (6), 504-10.
72. Griffin, J. M.; Forse, A. C.; Tsai, W. Y.; Taberna, P. L.; Simon, P.; Grey, C. P., *Nat Mater* 2015, *14* (8), 812-9.
73. Kitada, K.; Pecher, O.; Magusin, P.; Groh, M. F.; Weatherup, R. S.; Grey, C. P., *J Am Chem Soc* 2019, *141* (17), 7014-7027.
74. Pecher, O.; Bayley, P. M.; Liu, H.; Liu, Z.; Trease, N. M.; Grey, C. P., *J Magn Reson* 2016, *265*, 200-9.
75. Liu, Z.; Hu, Y.-Y.; Dunstan, M. T.; Huo, H.; Hao, X.; Zou, H.; Zhong, G.; Yang, Y.; Grey, C. P., *Chemistry of Materials* 2014, *26* (8), 2513-2521.
76. Xie, X.; Makaryan, T.; Zhao, M.; Van Aken, K. L.; Gogotsi, Y.; Wang, G., *Adv. Energy Mater.* 2016, *6* (5), 1502161.
77. Aurbach, D.; Turgeman, R.; Chusid, O.; Gofer, Y., *Electrochem. Commun.* 2001, *3* (5), 252-261.
78. Wei, Q.; Liu, J.; Feng, W.; Sheng, J.; Tian, X.; He, L.; An, Q.; Mai, L., *J. Mater. Chem. A* 2015, *3* (15), 8070-8075.
79. Lu, J.; Wu, T.; Amine, K., *Nature Energy* 2017, *2* (3).
80. Soto, F. A.; Yan, P.; Engelhard, M. H.; Marzouk, A.; Wang, C.; Xu, G.; Chen, Z.; Amine, K.; Liu, J.; Sprenkle, V. L.; El-Mellouhi, F.; Balbuena, P. B.; Li, X., *Adv Mater* 2017, *29* (18).
81. Brant, W. R.; Li, D.; Gu, Q.; Schmid, S., *Journal of Power Sources* 2016, *302*, 126-134.
82. Bard, A. J.; Faulkner, L. R.; Leddy, J.; Zoski, C. G., *Electrochemical methods: fundamentals and applications*. wiley New York: 1980; Vol. 2.
83. Shen, Z.; Cao, L.; Rahn, C. D.; Wang, C.-Y., *Journal of The Electrochemical Society* 2013, *160* (10), A1842-A1846.
84. Chao, D.; Zhu, C.; Yang, P.; Xia, X.; Liu, J.; Wang, J.; Fan, X.; Savilov, S. V.; Lin, J.; Fan, H. J.; Shen, Z. X., *Nat Commun* 2016, *7*, 12122.
85. Chao, D.; Liang, P.; Chen, Z.; Bai, L.; Shen, H.; Liu, X.; Xia, X.; Zhao, Y.; Savilov, S. V.; Lin, J.; Shen, Z. X., *ACS Nano* 2016, *10* (11), 10211-10219.
86. Bonaccorso, F.; Colombo, L.; Yu, G.; Stoller, M.; Tozzini, V.; Ferrari, A. C.; Ruoff, R. S.; Pellegrini, V., *Science* 2015, *347* (6217), 1246501.
87. Xie, L. M., *Nanoscale* 2015, *7* (44), 18392-401.
88. Chen, Y. M.; Yu, X. Y.; Li, Z.; Paik, U.; Lou, X. W. D., *Science Advances* 2016, *2*, e1600021.
89. Balendhran, S.; Walia, S.; Nili, H.; Ou, J. Z.; Zhuiykov, S.; Kaner, R. B.; Sriram, S.; Bhaskaran, M.; Kalantar-zadeh, K., *Advanced Functional Materials* 2013, *23* (32), 3952-3970.

90. Wang, H.; Feng, H.; Li, J., *Small* 2014, *10* (11), 2165-81.
91. Huang, X.; Zeng, Z.; Zhang, H., *Chem Soc Rev* 2013, *42* (5), 1934-46.
92. Cook, J. B.; Kim, H.-S.; Yan, Y.; Ko, J. S.; Robbennolt, S.; Dunn, B.; Tolbert, S. H., *Adv. Energy Mater.* 2016, *6* (9), 1501937.
93. Hu, Z.; Wang, L.; Zhang, K.; Wang, J.; Cheng, F.; Tao, Z.; Chen, J., *Angewandte Chemie* 2014, *126* (47), 13008-13012.
94. Wang, H.; Kong, D.; Johanes, P.; Cha, J. J.; Zheng, G.; Yan, K.; Liu, N.; Cui, Y., *Nano Lett* 2013, *13* (7), 3426-33.
95. Li, H.; Duan, X.; Wu, X.; Zhuang, X.; Zhou, H.; Zhang, Q.; Zhu, X.; Hu, W.; Ren, P.; Guo, P.; Ma, L.; Fan, X.; Wang, X.; Xu, J.; Pan, A.; Duan, X., *J Am Chem Soc* 2014, *136* (10), 3756-9.
96. Feng, Q.; Zhu, Y.; Hong, J.; Zhang, M.; Duan, W.; Mao, N.; Wu, J.; Xu, H.; Dong, F.; Lin, F.; Jin, C.; Wang, C.; Zhang, J.; Xie, L., *Adv Mater* 2014, *26* (17), 2648-2653.
97. Xie, D.; Xia, X.; Zhong, Y.; Wang, Y.; Wang, D.; Wang, X.; Tu, J., *Adv. Energy Mater.* 2016, 1601804.
98. Xie, D.; Tang, W.; Wang, Y.; Xia, X.; Zhong, Y.; Zhou, D.; Wang, D.; Wang, X.; Tu, J., *Nano Research* 2016, *9* (6), 1618-1629.
99. Yang, X.; Zhang, Z.; Fu, Y.; Li, Q., *Nanoscale* 2015, *7* (22), 10198-203.
100. Wang, H.; Lan, X.; Jiang, D.; Zhang, Y.; Zhong, H.; Zhang, Z.; Jiang, Y., *Journal of Power Sources* 2015, *283*, 187-194.
101. Wei Seh, Z.; Li, W.; Cha, J. J.; Zheng, G.; Yang, Y.; McDowell, M. T.; Hsu, P. C.; Cui, Y., *Nat Commun* 2013, *4*, 1331.
102. Yang, Y.; Zheng, G.; Cui, Y., *Chem Soc Rev* 2013, *42* (7), 3018-32.
103. Luo, C.; Xu, Y.; Zhu, Y.; Liu, Y.; Zheng, S.; Liu, Y.; Langrock, A.; Wang, C., *ACS nano* 2013, *7* (9), 8003-8010.
104. Ko, Y. N.; Choi, S. H.; Park, S. B.; Kang, Y. C., *Nanoscale* 2014, *6* (18), 10511-5.
105. Liu, Q.; Hu, Z.; Chen, M.; Zou, C.; Jin, H.; Wang, S.; Chou, S. L.; Dou, S. X., *Small* 2019, e1805381.
106. Li, Y.; Liang, Y.; Robles Hernandez, F. C.; Deog Yoo, H.; An, Q.; Yao, Y., *Nano Energy* 2015, *15*, 453-461.
107. Su, D.; Dou, S.; Wang, G., *Chem Commun (Camb)* 2014, *50* (32), 4192-5.
108. Fu, Y.; Manthiram, A., *RSC Advances* 2012, *2* (14), 5927.
109. Li, X.; Meduri, P.; Chen, X.; Qi, W.; Engelhard, M. H.; Xu, W.; Ding, F.; Xiao, J.; Wang, W.; Wang, C.; Zhang, J.-G.; Liu, J., *J. Mater. Chem.* 2012, *22* (22), 11014.
110. Su, L.; Jing, Y.; Zhou, Z., *Nanoscale* 2011, *3* (10), 3967-83.
111. Wu, F.; Chen, J.; Chen, R.; Wu, S.; Li, L.; Chen, S.; Zhao, T., *The Journal of Physical Chemistry C* 2011, *115* (13), 6057-6063.
112. Zhu, C.; Song, K.; van Aken, P. A.; Maier, J.; Yu, Y., *Nano Lett* 2014, *14* (4), 2175-80.
113. Zhang, L.; Zhang, G.; Wu, H. B.; Yu, L.; Lou, X. W., *Adv Mater* 2013, *25* (18), 2589-93.
114. Zheng, G.; Lee, S. W.; Liang, Z.; Lee, H. W.; Yan, K.; Yao, H.; Wang, H.; Li, W.; Chu, S.; Cui, Y., *Nat Nanotechnol* 2014, *9* (8), 618-23.
115. Jian, Z.; Han, W.; Lu, X.; Yang, H.; Hu, Y.-S.; Zhou, J.; Zhou, Z.; Li, J.; Chen, W.; Chen, D.; Chen, L., *Adv. Energy Mater.* 2013, *3* (2), 156-160.
116. Xie, K.; Wu, P.; Zhou, Y.; Ye, Y.; Wang, H.; Tang, Y.; Zhou, Y.; Lu, T., *ACS Appl Mater Interfaces* 2014, *6* (13), 10602-7.
117. Jeong, J. M.; Lee, K. G.; Chang, S. J.; Kim, J. W.; Han, Y. K.; Lee, S. J.; Choi, B. G., *Nanoscale* 2015, *7* (1), 324-9.
118. Qiu, Y.; Rong, G.; Yang, J.; Li, G.; Ma, S.; Wang, X.; Pan, Z.; Hou, Y.; Liu, M.; Ye, F.; Li, W.; Seh, Z. W.; Tao, X.; Yao, H.; Liu, N.; Zhang, R.; Zhou, G.; Wang, J.; Fan, S.; Cui, Y.; Zhang, Y., *Adv. Energy Mater.* 2015, *5* (23), 1501369.
119. Zhao, C.; Kong, J.; Yang, L.; Yao, X.; Phua, S. L.; Lu, X., *Chem Commun (Camb)* 2014, *50* (68), 9672-5.

120. Liu, Y.; Ai, K.; Lu, L., *Chem Rev* 2014, *114* (9), 5057-115.
121. Kong, J.; Yee, W. A.; Yang, L.; Wei, Y.; Phua, S. L.; Ong, H. G.; Ang, J. M.; Li, X.; Lu, X., *Chem Commun (Camb)* 2012, *48* (83), 10316-8.
122. Lu, Y.; Ang, H.; Yan, Q.; Fong, E., *Chemistry of Materials* 2016, *28* (16), 5743-5752.
123. Chen, Y. Y.; Zhang, Y.; Jiang, W. J.; Zhang, X.; Dai, Z.; Wan, L. J.; Hu, J. S., *ACS Nano* 2016, *10* (9), 8851-60.
124. Zhang, Z.; Yang, X.; Fu, Y.; Du, K., *Journal of Power Sources* 2015, *296*, 2-9.
125. Zhang, Y.; Ouyang, B.; Xu, J.; Chen, S.; Rawat, R. S.; Fan, H. J., *Adv. Energy Mater.* 2016, *6* (11), 1600221.
126. Zhang, Z.; Fu, Y.; Yang, X.; Qu, Y.; Zhang, Z., *ChemNanoMat* 2015, *1* (6), 409-414.
127. Wang, H.; Wang, L.; Wang, X.; Quan, J.; Mi, L.; Yuan, L.; Li, G.; Zhang, B.; Zhong, H.; Jiang, Y., *Journal of The Electrochemical Society* 2016, *163* (8), A1627-A1632.
128. Zhang, Y.; Liu, Z.; Zhao, H.; Du, Y., *RSC Adv.* 2016, *6* (2), 1440-1444.
129. Yang, X.; Zhang, Z.; Shi, X., *Journal of Alloys and Compounds* 2016, *686*, 413-420.
130. Sen, U. K.; Johari, P.; Basu, S.; Nayak, C.; Mitra, S., *Nanoscale* 2014, *6* (17), 10243-54.
131. Kim, H. S.; Cook, J. B.; Lin, H.; Ko, J. S.; Tolbert, S. H.; Ozolins, V.; Dunn, B., *Nat Mater* 2017, *16*, 454-460.
132. Choi, S. H.; Ko, Y. N.; Lee, J.-K.; Kang, Y. C., *Adv. Funct. Mater* 2015, *25* (12), 1780-1788.
133. Zhang, S.; Yu, X.; Yu, H.; Chen, Y.; Gao, P.; Li, C.; Zhu, C., *ACS Appl Mater Interfaces* 2014, *6* (24), 21880-218805.
134. Shi, Z.-T.; Kang, W.; Xu, J.; Sun, Y.-W.; Jiang, M.; Ng, T.-W.; Xue, H.-T.; Yu, D. Y. W.; Zhang, W.; Lee, C.-S., *Nano Energy* 2016, *22*, 27-37.
135. Wang, Y. X.; Chou, S. L.; Wexler, D.; Liu, H. K.; Dou, S. X., *Chem. Eur. J* 2014, *20* (31), 9607-9612.
136. Zhu, C.; Mu, X.; van Aken, P. A.; Yu, Y.; Maier, J., *Angew Chem Int Ed Engl* 2014, *53* (8), 2152-2156.
137. Bang, G. S.; Nam, K. W.; Kim, J. Y.; Shin, J.; Choi, J. W.; Choi, S. Y., *ACS Appl Mater Interfaces* 2014, *6* (10), 7084-7089.
138. Wang, J.; Luo, C.; Gao, T.; Langrock, A.; Mignerey, A. C.; Wang, C., *Small* 2015, *11* (4), 473-481.
139. Liang, Y.; Yoo, H. D.; Li, Y.; Shuai, J.; Calderon, H. A.; Robles Hernandez, F. C.; Grabow, L. C.; Yao, Y., *Nano Lett* 2015, *15* (3), 2194-2202.
140. Fan, X.; Gaddam, R. R.; Kumar, N. A.; Zhao, X. S., *Adv. Energy Mater* 2017, *17*, 1700317.
141. Zhang, W.; Li, X.; Jiang, T.; Song, J.; Lin, Y.; Zhu, L.; Xu, X., *Nanoscale* 2015, *7* (32), 13554-13560.
142. Yang, L.; Fu, Q.; Wang, W.; Huang, J.; Huang, J.; Zhang, J.; Xiang, B., *Nanoscale* 2015, *7* (23), 10490-10497.
143. Zhu, C.; Yang, P.; Chao, D.; Wang, X.; Zhang, X.; Chen, S.; Tay, B. K.; Huang, H.; Zhang, H.; Mai, W.; Fan, H. J., *Adv Mater* 2015, *27* (31), 4566-71.
144. Jadczak, J.; Dumcenco, D. O.; Huang, Y. S.; Lin, Y. C.; Suenaga, K.; Wu, P. H.; Hsu, H. P.; Tiong, K. K., *J. Appl. Phys* 2014, *116* (19), 193505.
145. Feng, Q.; Mao, N.; Wu, J.; Xu, H.; Wang, C.; Zhang, J.; Xie, L., *ACS nano* 2015, *9* (7), 7450-7455.
146. Alam Khan, M.; Kang, Y.-M., *Journal of Energy Storage* 2016, *7*, 252-257.
147. Liu, Y.; Wang, X.; Song, X.; Dong, Y.; Yang, L.; Wang, L.; Jia, D.; Zhao, Z.; Qiu, J., *Carbon* 2016, *109*, 461-471.
148. Teng, Y.; Zhao, H.; Zhang, Z.; Zhao, L.; Zhang, Y.; Li, Z.; Xia, Q.; Du, Z.; Świerczek, K., *Carbon* 2017, *119*, 91-100.
149. Wang, H.; Jiang, H.; Hu, Y.; Saha, P.; Cheng, Q.; Li, C., *Chem. Eng. Sci.* 2017, *174*, 104-111.
150. Qin, W.; Chen, T.; Pan, L.; Niu, L.; Hu, B.; Li, D.; Li, J.; Sun, Z., *Electrochim. Acta* 2015, *153*, 55-61.

151. Chen, C.; Li, G.; Lu, Y.; Zhu, J.; Jiang, M.; Hu, Y.; Cao, L.; Zhang, X., *Electrochim. Acta* 2016, *222*, 1751-1760.
152. Li, X.; Li, J.; Gao, Q.; Yu, X.; Hu, R.; Liu, J.; Yang, L.; Zhu, M., *Electrochim. Acta* 2017, *254*, 172-180.
153. Liang, J.; Wei, Z.; Wang, C.; Ma, J., *Electrochim. Acta* 2018, *285*, 301-308.
154. Lin, M.; Deng, M.; Zhou, C.; Shu, Y.; Yang, L.; Ouyang, L.; Gao, Q.; Zhu, M., *Electrochim. Acta* 2019, *309*, 25-33.
155. Wang, J.; Han, L.; Li, X.; Zeng, L.; Wei, M., *J. Colloid Interface Sci.* 2019, *548*, 20-24.
156. Chen, W.; Wu, W.; Pan, Z.; Wu, X.; Zhang, H., *Journal of Alloys and Compounds* 2018, *763*, 257-266.
157. Hu, Y.-Y.; Bai, Y.-L.; Wu, X.-Y.; Wei, X.; Wang, K.-X.; Chen, J.-S., *Journal of Alloys and Compounds* 2019, *797*, 1126-1132.
158. Li, X.; Yang, Y.; Liu, J.; Ouyang, L.; Liu, J.; Hu, R.; Yang, L.; Zhu, M., *Applied Surface Science* 2017, *413*, 169-174.
159. Che, Z.; Li, Y.; Chen, K.; Wei, M., *Journal of Power Sources* 2016, *331*, 50-57.
160. Cai, Y.; Yang, H.; Zhou, J.; Luo, Z.; Fang, G.; Liu, S.; Pan, A.; Liang, S., *Chemical Engineering Journal* 2017, *327*, 522-529.
161. Li, J.; Qin, W.; Xie, J.; Lin, R.; Wang, Z.; Pan, L.; Mai, W., *Chemical Engineering Journal* 2018, *332*, 260-266.
162. Xu, J.; Jia, G.; Mai, W.; Fan, H. J., *Advanced Materials Interfaces* 2016, *3* (20).
163. Kundu, D.; Adams, B. D.; Duffort, V.; Vajargah, S. H.; Nazar, L. F., *Nature Energy* 2016, *1* (10), 16119.
164. Li, Y.; Fu, J.; Zhong, C.; Wu, T.; Chen, Z.; Hu, W.; Amine, K.; Lu, J., *Adv. Energy Mater.* 2018.
165. Verma, V.; Kumar, S.; Manalastas, W.; Satish, R.; Srinivasan, M., *Advanced Sustainable Systems* 2018.
166. Wang, D.; Wei, Q.; Sheng, J.; Hu, P.; Yan, M.; Sun, R.; Xu, X.; An, Q.; Mai, L., *Phys Chem Chem Phys* 2016, *18* (17), 12074-9.
167. Tang, H.; Xu, N.; Pei, C.; Xiong, F.; Tan, S.; Luo, W.; An, Q.; Mai, L., *ACS Appl Mater Interfaces* 2017, *9* (34), 28667-28673.
168. Pang, Q.; Sun, C.; Yu, Y.; Zhao, K.; Zhang, Z.; Voyles, P. M.; Chen, G.; Wei, Y.; Wang, X., *Adv. Energy Mater.* 2018, *8* (19).
169. He, P.; Quan, Y.; Xu, X.; Yan, M.; Yang, W.; An, Q.; He, L.; Mai, L., *Small* 2017.
170. Mjejri, I.; Etteyeb, N.; Sediri, F., *Materials Research Bulletin* 2013, *48* (9), 3335-3341.
171. Dai, Y.; Li, Q.; Tan, S.; Wei, Q.; Pan, Y.; Tian, X.; Zhao, K.; Xu, X.; An, Q.; Mai, L.; Zhang, Q., *Nano Energy* 2017, *40*, 73-81.
172. Liu, Z.; Xu, R.; Wei, W.; Jing, P.; Li, X.; Zhu, Q.; Sun, H.; Dong, Y.; Zakharova, G. S., *Solid State Ionics* 2019, *329*, 74-81.
173. Kundu, D.; Hosseini Vajargah, S.; Wan, L.; Adams, B.; Prendergast, D.; Nazar, L. F., *Energy & Environmental Science* 2018, *11* (4), 881-892.
174. Shi, H.; Liang, H.; Ming, F.; Wang, Z., *Angew Chem Int Ed Engl* 2017, *56* (2), 573-577.
175. Wu, C.; Zhang, X.; Ning, B.; Yang, J.; Xie, Y., *Inorg Chem* 2009, *48* (13), 6044-54.
176. Boukhalfa, S.; Evanoff, K.; Yushin, G., *Energy & Environmental Science* 2012, *5* (5).
177. Sawatzky, G. A.; Post, D., *Physical Review B* 1979, *20* (4), 1546-1555.
178. Silversmit, G.; Depla, D.; Poelman, H.; Marin, G. B.; De Gryse, R., *J. Electron. Spectrosc. Relat. Phenom.* 2004, *135* (2-3), 167-175.
179. Zhu, H.; Ruan, S., *Materials Letters* 2016, *184*, 134-138.
180. Wei, T.; Li, Q.; Yang, G.; Wang, C., *Journal of Materials Chemistry A* 2018, *6* (17), 8006-8012.
181. Ding, J.; Du, Z.; Gu, L.; Li, B.; Wang, L.; Wang, S.; Gong, Y.; Yang, S., *Adv Mater* 2018, e1800762.
182. Dai, X.; Wan, F.; Zhang, L.; Cao, H.; Niu, Z., *Energy Storage Materials* 2019, *17*, 143-150.

183. Hu, P.; Yan, M.; Zhu, T.; Wang, X.; Wei, X.; Li, J.; Zhou, L.; Li, Z.; Chen, L.; Mai, L., *ACS Appl Mater Interfaces* 2017.
184. Zhang, N.; Dong, Y.; Jia, M.; Bian, X.; Wang, Y.; Qiu, M.; Xu, J.; Liu, Y.; Jiao, L.; Cheng, F., *ACS Energy Letters* 2018, *3* (6), 1366-1372.
185. Zhou, J.; Shan, L.; Wu, Z.; Guo, X.; Fang, G.; Liang, S., *Chem Commun (Camb)* 2018, *54* (35), 4457-4460.
186. Senguttuvan, P.; Han, S.-D.; Kim, S.; Lipson, A. L.; Tepavcevic, S.; Fister, T. T.; Bloom, I. D.; Burrell, A. K.; Johnson, C. S., *Adv. Energy Mater.* 2016, 1600826.
187. Yan, M.; He, P.; Chen, Y.; Wang, S.; Wei, Q.; Zhao, K.; Xu, X.; An, Q.; Shuang, Y.; Shao, Y.; Mueller, K. T.; Mai, L.; Liu, J.; Yang, J., *Adv Mater* 2018, *30* (1).
188. Xu, D.; Wang, H.; Li, F.; Guan, Z.; Wang, R.; He, B.; Gong, Y.; Hu, X., *Advanced Materials Interfaces* 2019, *6* (2).
189. Wei, T.; Li, Q.; Yang, G.; Wang, C., *Electrochim. Acta* 2018, *287*, 60-67.
190. Alfaruqi, M. H.; Mathew, V.; Song, J.; Kim, S.; Islam, S.; Pham, D. T.; Jo, J.; Kim, S.; Baboo, J. P.; Xiu, Z.; Lee, K.-S.; Sun, Y.-K.; Kim, J., *Chemistry of Materials* 2017, *29* (4), 1684-1694.
191. He, P.; Zhang, G.; Liao, X.; Yan, M.; Xu, X.; An, Q.; Liu, J.; Mai, L., *Adv. Energy Mater.* 2018, *8* (10).
192. Cai, Y.; Liu, F.; Luo, Z.; Fang, G.; Zhou, J.; Pan, A.; Liang, S., *Energy Storage Materials* 2018, *13*, 168-174.
193. Sambandam, B.; Soundharrajan, V.; Kim, S.; Alfaruqi, M. H.; Jo, J.; Kim, S.; Mathew, V.; Sun, Y.-k.; Kim, J., *Journal of Materials Chemistry A* 2018, *6* (9), 3850-3856.
194. Xia, C.; Guo, J.; Lei, Y.; Liang, H.; Zhao, C.; Alshareef, H. N., *Adv Mater* 2018, *30* (5).
195. Ming, F.; Liang, H.; Lei, Y.; Kandambeth, S.; Eddaoudi, M.; Alshareef, H. N., *ACS Energy Letters* 2018, *3* (10), 2602-2609.
196. Xia, C.; Guo, J.; Li, P.; Zhang, X.; Alshareef, H. N., *Angew Chem Int Ed Engl* 2018, *57* (15), 3943-3948.
197. Tang, K.; Yu, X.; Sun, J.; Li, H.; Huang, X., *Electrochim. Acta* 2011, *56* (13), 4869-4875.
198. Wu, M.-S.; Wang, M.-J.; Jow, J.-J.; Yang, W.-D.; Hsieh, C.-Y.; Tsai, H.-M., *Journal of Power Sources* 2008, *185* (2), 1420-1424.
199. Ouyang, B.; Chao, D.; Jia, G.; Zhang, Z.; Fan, H. J.; Rawat, R. S., *Energy Storage Materials* 2019, *18*, 462-469.
200. Jia, G.; Chao, D.; Tiep, N. H.; Zhang, Z.; Fan, H. J., *Energy Storage Materials* 2018, *14*, 136-142.
201. Fang, X.; Hua, C.; Guo, X.; Hu, Y.; Wang, Z.; Gao, X.; Wu, F.; Wang, J.; Chen, L., *Electrochim. Acta* 2012, *81*, 155-160.
202. Ebbinghaus, S. G.; Hanss, J.; Klemm, M.; Horn, S., *Journal of Alloys and Compounds* 2004, *370* (1-2), 75-79.
203. Zheng, C.; Zeng, L.; Wang, M.; Zheng, H.; Wei, M., *CrystEngComm* 2014, *16* (44), 10309-10313.
204. Sun, Y.; Jiang, S.; Bi, W.; Wu, C.; Xie, Y., *Journal of Power Sources* 2011, *196* (20), 8644-8650.
205. Huang, Y.; Mou, J.; Liu, W.; Wang, X.; Dong, L.; Kang, F.; Xu, C., *Nano-Micro Letters* 2019, *11* (1).
206. Wang, J.; Yamada, Y.; Sodeyama, K.; Watanabe, E.; Takada, K.; Tateyama, Y.; Yamada, A., *Nature Energy* 2017, *3* (1), 22-29.
207. Qiu, H.; Du, X.; Zhao, J.; Wang, Y.; Ju, J.; Chen, Z.; Hu, Z.; Yan, D.; Zhou, X.; Cui, G., *Nat Commun* 2019, *10* (1), 5374.